Novel Light and Strong Aluminum-Boron Nitride Nanotube Composites

Maho Yamaguchi
Doctoral Program in Materials Science and Engineering

Submitted to the Graduate School of
Pure and Applied Sciences
in Partial Fulfillment of the Requirements

for the Degree of Doctor of Philosophy in

Engineering

at the
University of Tsukuba

Abstract

Nowadays, it is becoming more and more important to provide "superlight" and "superstrong" materials for vehicles to make them lighter and reduce the amount of carbon dioxide or fuel cost. Metal matrix composites (MMC) made of aluminum and carbon nanotubes (CNTs) have become of great interest with respect to utilization in automotive, aircraft and aerospace industries [1]. However, CNTs have drawbacks for those applications such as absorption of light, and thus heating, and ease in bundling and buckling. Boron nitride nanotubes (BNNTs), while having quite similar structures to CNTs, are particularly known for their remarkable mechanical properties, no absorption of visible light, high thermal, chemical and oxidation stabilities, and straight needle-like morphologies. They have low density (1.4 g/cm^3), high ultimate tensile strength (~35 GPa) and high Young's modulus (~ 1 TPa), thus the figures which are much more impressive than those typical for standard reinforcing materials, such as aluminum nitride or silicon carbide. To make decently strong composites, it is important to have intimate and robust interfaces between metals and nano-reinforcing fibers. BNNTs may be able to create such interfacial structures and maintain them up to high temperatures due to their superb thermal and oxidation stabilities (up to ~ 1000 °C) in air. In order to create this new generation of "nanotube-metal composites", herein BNNTs were utilized as novel nanofillers for the reinforcement of light metals, such as aluminum (Al). In this Thesis, the regarded composites were fabricated at nano-, micro- and macro-scales through various processing methods and their structures and mechanical properties were then reported in detail.

First, Al-BNNT composite nanohybrids with a varying Al coating thickness were fabricated by magnetron sputtering. Al uniformly coated each BNNT. Using imaging techniques and electron diffraction analysis in a transmission electron microscope, the Al phase was found to create nanocrystalline shields around individual BNNTs. The chemical states of the hybrid nanomaterials during the initial stages of sputtering were analyzed by X-ray photoelectron spectroscopy. Direct in situ bending and tensile tests on individual BNNT–Al nanocomposites were carried out by using a dedicated transmission electron microscope-atomic force microscope holder. In parallel, high-resolution TEM images and video recordings were taken for the analysis of deformation kinetics and fracture mechanisms. The nanohybrids with a suitably thick Al coating (~ 40 nm) withstood at least nine times higher stresses compared to a pure non-armed Al metal. This pioneering work opens up a prospective pathway for making ultralight and superstrong "dream" structural materials for future automotive and aerospace applications [2].

Next, a meter long and several dozen micrometers thick Al-BNNTs composite ribbons with various fractions of multiwalled BNNTs (0.5 to 3.0 wt%) were fabricated by melt spinning using an Al-BNNTs powder mixture. BNNTs were randomly dispersed within a microcrystalline Al matrix under ribbon casting and led to more than doubling of room-temperature ultimate tensile strength of the composites compared to pure Al ribbons produced at the similar conditions. The comparative structural characteristics were analyzed using X-ray diffraction, scanning and transmission electron microscopy, and internal friction measurements

Abstract

as a function of temperature within a 80–800 K range. Room temperature tensile tests were carried out on ribbons. These revealed reinforcing effects on pure Al-matrices after nano/micro-BN embedment for both added phases with the notably higher numbers peculiar to the BNNT-containing samples. The intra-structural interactions between BN additions and Al-matrices are discussed based on the structural analysis and the internal friction data [3, 4].

Powder metallurgy is one of the most popular methods for Al-based MMC processing. Thus finally, for making Al-BNNTs composites with up to 5 wt% (i.e. 9.7 vol%) nanotube fractions Spark Plasma Sintering (SPS) and High Pressure Torsion (HPT) methods were utilized. Various microscopy techniques, X-ray diffraction, and energy dispersive X-ray analysis confirmed the integration of the two phases into decently dense and compact composites. No other phases, like Al borides or nitrides, form in the Al-BNNTs macrocomposites of the two series. The BNNTs were found to be preferentially located along Al grain boundaries in SPS samples (grain size was 10-20 micrometers) creating micro-discontinuities and pores which were found to be detrimental for the sample hardness, whereas in HPT samples, the tubes were rather evenly distributed within a fine-grained Al matrix (grain size of several hundred nm). Therefore the hardness of HPT samples was drastically increased with increasing BNNTs content in Al pellets. The value for Al-BNNT 3.0 wt% sample was more than doubled (190 MPa) compared to a pure Al HPT compact (90 MPa). And the room temperature ultimate tensile strength of Al-BNNTs HPT samples containing 3.0 wt% BNNT (~300 MPa) became ~1.5 times larger than that of a BNNT-free HPT Al compact (~200 MPa) [5].

Over all, I have studied Al-BNNTs composites by using various fabrication processes and at the different length scales – from nano- *via* micro-, and to macro-dimensions. The strength of Al-BNNTs composites was always higher than that of pure Al samples prepared using analogous procedures. These results demonstrate that BNNTs can be a promising candidate for the reinforcement of light metal matrices which may be used in harsh environments and conditions, and for the growing demands of aerospace, aircraft and automotive industries.

References

[1] S.R. Bakshi, D. Lahiri, A. Agarwal, *Inter. Mater. Rev.*, **2010**, 55, 41.

[2] M. Yamaguchi, D.M. Tang, C.Y. Zhi, Y. Bando, D. Shtansky, D. Golberg, *Acta Mater.*, **2012**, 60, 6213.

[3] M. Yamaguchi, A. Pakdel, C.Y. Zhi, Y. Bando, D.M. Tang, K. Faerstein, D. Shtansky, D. Golberg, *Nanoscale Res. Lett.*, **2012**,8, 3.

[4] M. Yamaguchi, J. Bernhardt, K. Faerstein, D. Shtansky, Y. Bando, I.S. Golovin, H.R. Sinning, D. Golberg, *Acta Mater.*, **2013**, 61, 7604.

[5] M.Yamaguchi, F. Meng, K. Faerstein, K. Tsuchiya, D. Golberg. *Mater. Sci. Eng. A.*, **2014**, Under submission.

Acknowledgements

It was such a great experience being a Ph.D. student at NIMS. While working there, I could work with and meet top researchers from all over the world. It would have not been possible to complete this doctoral thesis without the help and support of the kind people around me, to only some of whom it is possible to give particular mention here.

First of all, this Thesis would not have been possible to complete without the support and patience of my principal supervisor, Prof. Dmitri Golberg, not to mention his advice and unsurpassed knowledge of Materials Science. The great advice and support from another supervisor, Prof. Yoshio Bando, has been invaluable on both an academic and a personal level, for which I am extremely grateful. I also would like to acknowledge the financial, academic and technical support of the University of Tsukuba and National Institute for Materials Science (NIMS), particularly in the fellowship of a NIMS Junior researcher that provided the necessary financial support for this research. All the facilities (notably at International Center for Materials Nanoarchitectonics (MANA), NIMS)) and NIMS Sengen site have been indispensable.

I would like to thank Dr. Chunyi Zhi. I could not finish this Thesis work without his help such as in regards of synthesizing experiments and all the discussions with his profound knowledge of composite studies.

Also I am grateful to my group members, especially Drs. Akihiko Nukui, Masanori Mitome and Naoyuki Kawamoto for all the support in this lab, Dr. Daiming Tang for in-situ TEM analysis work support, Dr. Kotone Hasegawa for tutoring TEM sample making by FIB and Mr. Shigenobu Okamiya for BNNT synthesis support, I would like to thank them all deeply. I appreciate that all other members and friends also made my Ph.D. student life better.

I also would like to express my great gratitude to Prof. Koichi Tsuchiya, Prof. Tomonobu Nakayama, Prof. Hee Young Kim and Prof. Takao Mori to be my thesis committee members to discuss and give me such invaluable advices.

Second of all, my work could not be completed without collaborators from all over the world. First, I would like to thank all NIMS Sengen site collaborators - Prof. Kazuhiro Hono and his group members, especially Drs. Tadakatsu Ohkubo, Prahubu Delhibabu,Sepehri Amin Hossein and Uma Maheswara Rao Seelam for their support and deep understanding of melt-spinning, Prof. Yoshio Sakka and his group members, especially Dr. Mehdi Estili for their useful discussions with respect to SPS samples, and Prof. Tsuchiya and his group members, especially Dr. Fanqiang Meng and Mr. Baozhen Jiang, for their technical scientific support and advices.

I also have wonderful collaborators all over the world. I thank Prof. Jun Lou and his student Mr. Phillip Loya for their in-situ SEM mechanical tests on melt-spun ribbons. I also would give deep complement to Prof. Arkady Krasheninnikov, Aalto University and University of Helsinki, Finland and Drs. Dr. Dmitry Kvashnin and Dr. Pavel Sorokin, National Univeristy of Science and Technology, "MISIS", Moscow, Russia

Table of Contents

Chapter 1

Introduction

1. Introduction

Chapter 1 Introduction

1.1 Importance of light metals in aircraft, aerospace and automotive industries

Lightweight materials and their design have always been an important topic across several industries. Global trends toward CO_2 reduction and resource efficiency have significantly increased the importance of this topic over the last decade. Since Wright brothers created an airplane, people have long been looking for light and strong materials for its body. Among such materials, low density, lightweight aluminum and its alloys are one of the most important constituents of functional components used in aircrafts, aerospace and automotive applications [1]. Recent prominent examples lend evidence to the newest composite trend gaining momentum: the Boeing 787 Dreamliner is constructed largely of carbon fiber reinforced plastics instead of the traditional aluminum structure as shown in Figure 1.1 [2]. Yet most of the structural materials used in today's world are metals because the cost of new lightweight composite materials is still extremely high. Among them aluminum and its alloys are one of the most important constituents for structural components for the industries. Their light weight is the key, however, such metals are relatively soft. For example, a pure Al has a very modest Young's modulus and ultimate tensile strength values, ~70 GPa and ~40 MPa [3], respectively, these further decrease several times under heating to moderate temperatures of only 200 ~ 300 $^{\circ}$C. To make aluminum stronger without making them heavier, one of the most popular ideas is making an alloy. Ultimate tensile strength of typical aluminum alloys are 300 MPa (6061-T6) and 483 MPa (2014-T6) [4]. Making Al and its alloys much tougher and stiffer would lead to significantly minimized demands for structural component sizes and their thicknesses, and, in turn further decreases the overall construction weights. While such enhanced components would be fully capable of carrying high stresses present in harsh conditions which would be used for automotive airplanes and spacecrafts. According to the several reports related to lightweight materials trend, 2030 is the key target as (1) the number of aircraft and travelers will be increased to more than twice in the next two decades [5], (2) production of lightweight materials will increase significantly within the next two decades [1].

1.2 Metal matrix composite (MMC)

Metal matrix composites (MMC) are made of a metallic matrix that is reinforced with another material, usually in the form of fibers, particles, whiskers etc. According to Pai et al., [6] the reinforcing material usually carries most of the load, while the matrix material, by holding them together, enables a load transfer. The advantages of using such materials (with metals as matrices) include high tensile and shear moduli, good fatigue and fracture properties, small thermal expansion coefficient, high melting point, high toughness, high ductility, high thermal and electrical conductivities, good erosion (and/or corrosion) resistance, dimensional stability and good moisture resistance [7,8]. In addition, MMCs with aluminum as the matrix benefit from good wear resistance, high specific modulus and specific strength [9]. These days, metal matrix composites

1. Introduction

(MMCs) based on lightweight metals are extensively used in aerospace and automotive industries. Ceramics including Al_2O_3, TiC, B_4C or SiC were the first targets for reinforcement Al-MMC composites. One such example of MMC is an aluminum matrix composite reinforced by a silicon carbide. The most important property of aluminum-silicon carbide material with reference to the aerospace industry is its strength to weight ratio, which is three times more than that of a mild steel [10]. In addition composites containing SiC (reinforcing material) and Al (matrix) have higher modulus strength values, wear resistance, higher thermal stability, lower weight and a more effective load carrying capacity compared to many other materials [11,12]. It is also expected that this composite will exhibit good corrosion/oxidation properties since silicon carbide forms a protective coating of silicon oxide at 1200 ^{o}C [13] and, aluminum also displays a similar reaction. Therefore, this material offers considerable advantages to the aerospace industry especially in applications that require good thermal and tensile properties [14]

MMC-nanotube composite field is also a quickly emerging topic in Materials Science during the last couple of decades [15] especially after the identification of superstrong carbon nanotubes in 1991 [16]. The particular attention has been drawn to metallic matrices made of lightweight metals, among those aluminum is still the most popular [15, 17]. In fact, merging light masses and attractive visual appearances of Al with strong and elastic tubular fibers embedded in it, at least intuitively, should lead to the creation of breathtaking material – an ultralight and superstrong Al-nanotube composite. There is a variety of fabrication methods such as powder metallurgy, melting and solidification, thermal spraying, electrochemical deposition and so on. Not only those, it is getting more and more popular to develop and test new methods.
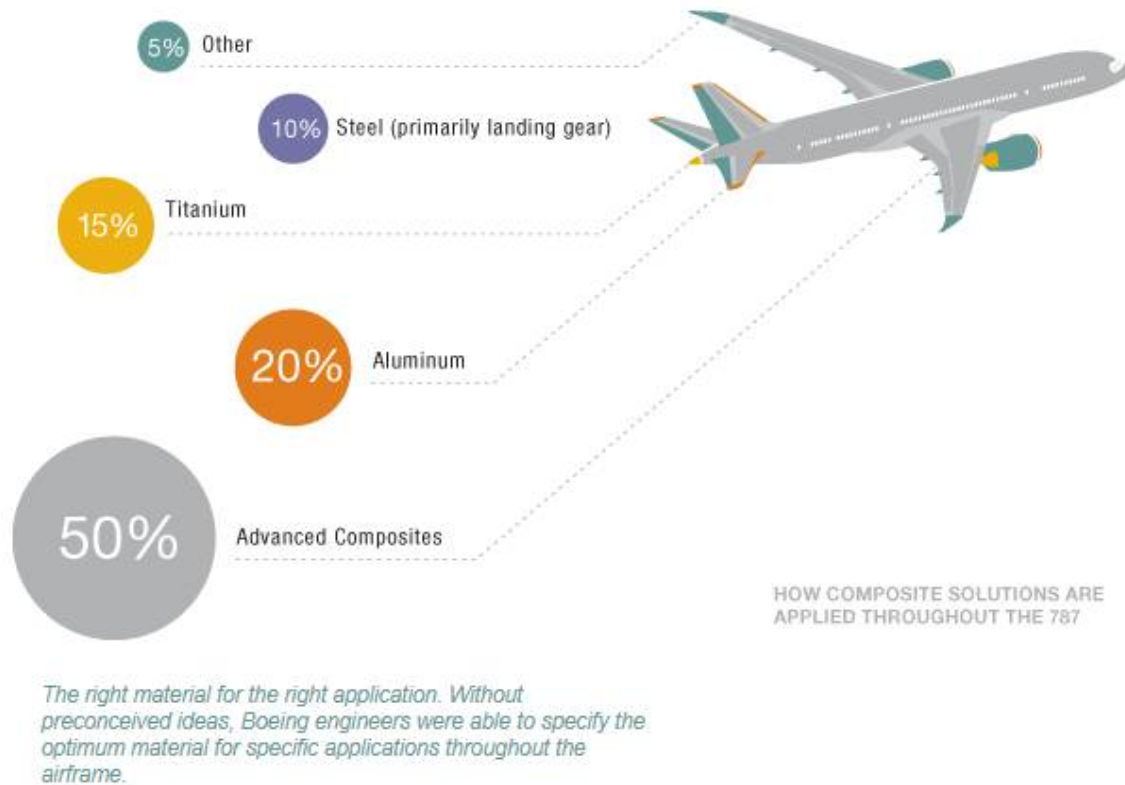
Figure 1.1 Materials usage for Boeing 787. They reduced much weight by using advanced composites.

1.3 Al-CNT composites

Over the last decade much research has been carried out in the field of standard carbon nanotube (CNT)-Al MMCs [15]. There has been a variety of methods such as powder metallurgy or melting and solidification processes which have been tried to fabricate CNT-MMCs. According to a review by Bakshi *et al.* [15] most of Al-CNT composites were prepared by a powder metallurgy route; however, these revealed several and rather severe technological drawbacks. For example, formation of aluminum carbide (Al_4C_3) in an Al-CNT matrix took place and, according to some reports, this effect reduced the composite mechanical strength [18], the others, by contrast, mentioned that some amount of Al_4C_3 had helped in the effective load transfer and pinning of CNTs to the matrix [19]. The formation of Al carbide (Al_4C_3) at the interfacial regions was in fact experimentally documented [23-26]. The thick layers of such carbide further deteriorated the composite mechanical performance, while the thin layers (below 20 nm thick) were found to be advantageous to enhance interfacial bonding [27]. However, the formation of rather thick carbide interfaces was found to occur rather quickly, even during flash thermal processes and treatments, like plasma spraying and plasma spark sintering. This feature was detrimental for the mechanical performance. Another problem is the large surface area of CNTs which led to the formation of nanotube clusters due to van der Waals forces,
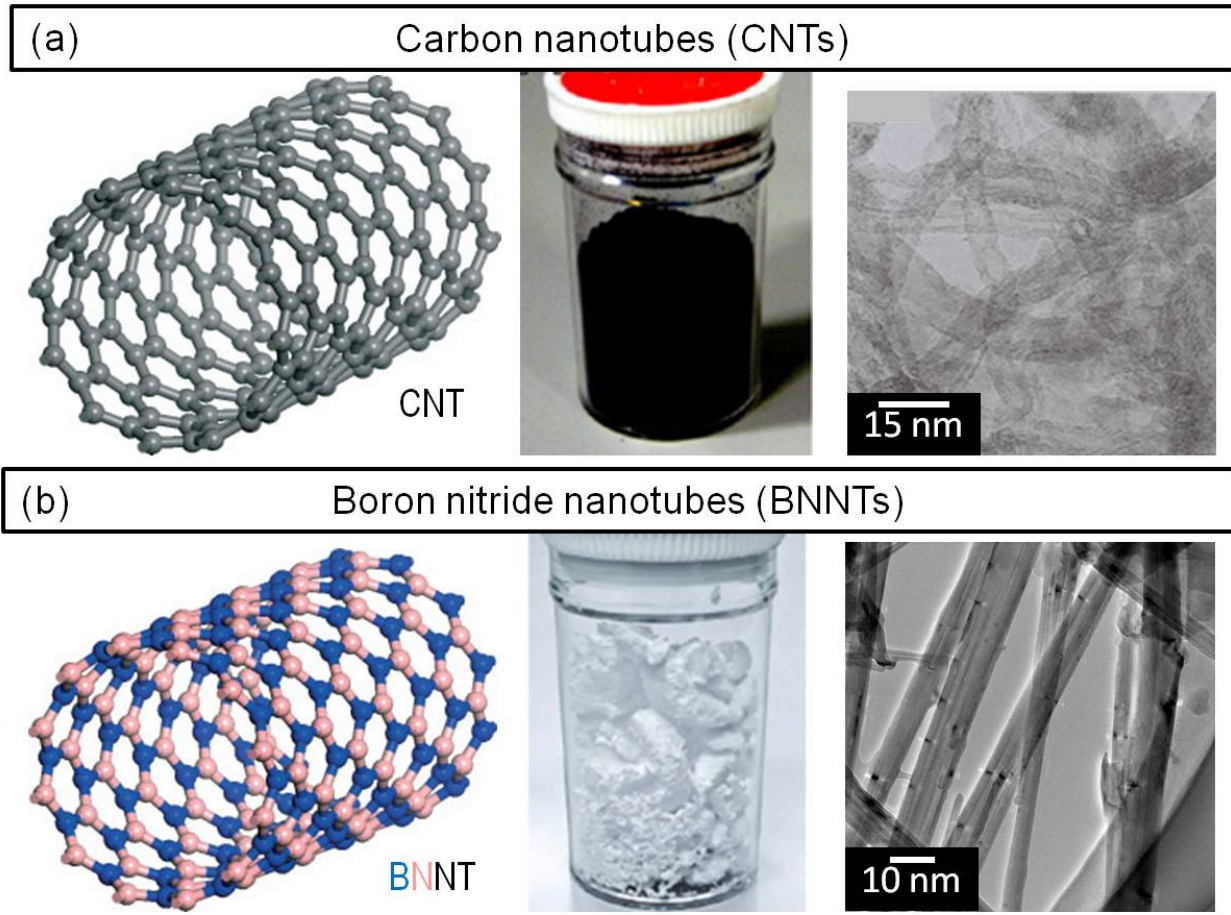
Figure 1.2 Comparison of (a) CNTs and (b) BNNTs. (Left) structural models of single-layered carbon and boron nitride nanotubes (CNTs and BNNTs, respectively). The alternating B and N atoms are shown in blue and pink, respectively, on the BNNT model, (middle) photo images of 1g appearance and (right) transparent electron microscopy images.

CNT bundling and entanglement within the matrix, and related difficulties in their uniform dispersion in Al. This, in turn, created internal stresses and/or microvoids and resulted in an insurmountable cracking at composite loading [20-22]. Also, in air, the CNTs typically start to burn at around 500-600 ^{o}C thus restricting medium and high temperature CNT-MMC applications.

Therefore, Al-CNT fabrication has not yet resulted in the drastic improvement of Al mechanical properties. This fact is likely due to many technological difficulties in CNT dispersion and weak nanotube/Al interfaces. The quality and strength of these interfaces are crucial issues for a load transfer from a soft Al matrix to the hard, tough and elastic nanotube fibers. In addition, CNTs always have buckled and curled appearances normal for the tubes produced through a standard Chemical Vapor Deposition (CVD). This technique is still the only one capable of producing large quantities of CNTs needed for the macroscale and nanotube-consuming composite research. Such waived and curled fiber morphologies insurmountably create microvoids within a metal matrix. These would serve as stress concentrators and crack inhibitors, and spoil the overall mechanical performance.

1.4 Boron Nitride Nanotube (BNNT) and its properties

Boron nitride nanotubes (BNNTs) are another type of nanotubes with a very similar crystal structure to that of CNTs in which alternating B and N atoms substitute for C atoms in a honeycomb lattice. They were theoretically predicted in 1994 [28, 29] and experimentally realized in 1995 by Zettl group [30]. Figure 1.2 shows (left) schematic images of CNT and BNNT atomic structures, (middle) 1g appearance and (right) transmission electron microscopy images of (a) CNTs and (b) BNNTs. Their atomic structure is similar, however, the appearance is quite different. BNNT exhibit many exciting properties, mechanical, thermal, electrical, and optical, particularly valuable for structural and composite applications. Also due to the specific ionic contribution into the B-N chemical bonding, a charge transfer between B and N atoms and preferential B-N-B-N stacking across the tubular multilayers, a BNNT has a characteristically straight, *i.e.* needle-like shape (opposed to CNTs, which are usually waved, entangled and curled).This makes it easy to achieve effective BNNT dispersion and/or texturing in any given matrix. B atoms prefer to have N atoms in the neighboring shells strictly above and beneath them for each local place on the tube. Therefore, there is no trend for bundling / curling / waving. A typical liquid solution of BN tubes consists of individual well separated straight-shape needles [31].

1.4.1   Mechanical properties

Theoretical studies by Hernandez *et al.* [32] revealed the elastic modulus for BNNTs with diameters ranging from 0.81 to 2.08 nm to vary between ~0.84 and ~ 0.91 TPa Chopra and Zettl [33] estimated the elastic modulus of a cantilevered individual double-walled BNNT by measuring the amplitude of the thermal-induced vibrations in a TEM at room temperature. They found a value of 1.22 ± 0.24 TPa, which is similar to the elastic modulus of CNTs. Subsequently, an electric-field-induced resonance method in TEM was utilized to calculate elastic modulus values between 0.51 and 1.03 TPa [34]. More recently, Golberg's group has performed extensive *in situ* TEM bending and tensile experiments on individual multi-walled tubes with diameters of 40 ~ 100 nm and estimated their elastic modulus as 0.5 ~ 0.6 TPa [35] or up to 1.3 TPa [36], and their tensile strength as ~33 GPa. However, in the case of bamboo-like BNNTs, the elastic modulus and tensile strength were estimated as 225 GPa and 8 GPa, respectively [37]. Superior mechanical properties and thermal conductivity of BN nanostructures make them attractive as nanofillers in composite materials. For instance, BNNTs can reinforce polymer matrices and improve their thermal conductivity, while transparency of the polymers is preserved. Zhi *et al.* [38] initiated research on polymer matrix composites reinforced by BNNTs and showed an effective improvement in elastic modulus of polystyrene and polymethyl methacrylate (PMMA) by ~ 20 % with addition of only 1 wt% of nanotubes. A very recent work on nanomechanical characterization of single-walled BNNTs revealed that they axially strong, but radically supple. Overall, BNNT characteristics might be superior to single-walled CNTs for the usage as reinforcing additives for nanocomposite applications [39].

1.4.2   Thermal properties

BNNTs have attractive thermal properties compared to those of CNTs. Theoretical calculations by Xiao *et al*. [40] demonstrated high specific heat of BNNTs and predicted that their thermal conductivity is higher than that of CNTs. They also showed that thermal conductance of single-walled BNNTs at low temperatures is independent of the tube diameter and chirality [41]. The high thermal conductivity (k) on the order of 350 WmK^{-1} was experimentally confirmed at room temperature for BNNTs having an outer diameter of 30 ~ 40 nm [42]. Thermal stability experiments on multi-walled BNNTs were performed by Golberg *et al*. [43] and indicated excellent oxidation resistance up to ~1000 °C in air. Moreover, thermogravimetric analysis showed that the onset temperature for the oxidation of BNNTs (> 800 °C) was much higher than that of CNTs (~ 400 °C) under the same conditions (shown in Figure 1.3).
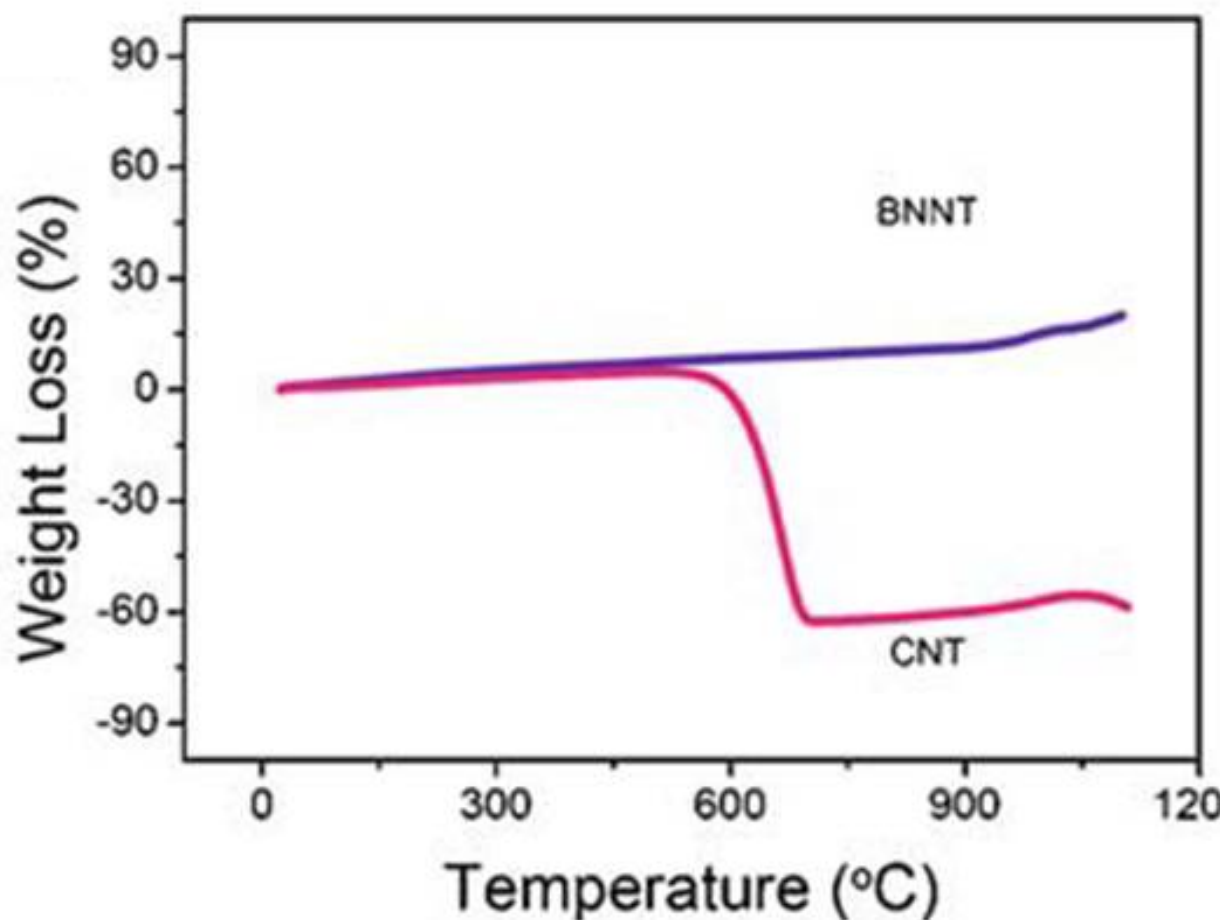

Figure 1.3 Comparative thermogravimetric analysis curves of BNNTs and CNTs (reprinted from [26]).

1.4.3 Electronic properties

BNNTs are theoretically predicted to have merely uniform electronic properties that are hardly modified by changing their chiralities or diameters [28, 29]. Moreover, zigzag BNNTs with chirality (n , 0) are expected to have a direct band gap. On the other hand, armchair BNNTs with chiral vectors (n , n) would have an indirect band gap [44] . Thanks to their large bandgap of ~ 5 eV, experiments using single-walled BNNTs as the conduction channel for field-effect transistors (FETs) showed that BNNTs allowed transport through only the valence band [45]. Another important feature about the band gaps of BNNTs is that they are tunable by doping with carbon [46], radial deformation [47], or by applying a transverse electric field across the BNNTs – the so-called giant Stark effect [48-50]. Experimentally, such effect has been observed when applying a scanning tunneling microscopy (STM) tip to impose a local transverse electric field onto BNNTs and simultaneously probing the electronic properties [50].

Theoretical band structure calculations suggested that BNNTs can either be *p-* type or *n-* type semiconductors by controlling the composition of carbon in BNNTs. Carbon impurities on the boron sites result in electron carriers while on the nitrogen sites result in hole carriers [46]. On the other hand, the band-gap modification by radial deformation in BNNTs was predicted through first-principles pseudopotential density-functional calculations. In zigzag BN nanotubes, radial deformations due to transverse pressures of about 10 GPa decrease the direct bandgap of BNNTs from 5 to 2 eV, allowing for optical applications in the visible range. However, the bandgaps of armchair BNNTs are found to be insensitive to radial deformations.

1.4.4 Optical properties

A local-density approximation (LDA) calculation has pointed out that optical bandgap of BNNTs is independent of the chirality [51]. Another interesting point related to their optical properties is the photoelectric effect. According to Kral *et al.*, unpolarized light can induce a shift current in BNNTs, with a direction along the tube axis [52]. These photoelectric effects can lead to new optoelectronic, optomechanical, and magnetic applications. To understand polarizabilities of BNNTs, Kongsted *et al.* investigated the polarizability tensors for several types of single-wall BNNTs and compared with corresponding CNTs [53]. Their computations showed that BNNTs had smaller magnitudes of the polarizability tensor components than those of CNTs with the same geometry and number of atoms. Polarizability tensor of BNNTs is shown to depend on the tubule length, chiralities, light frequency, etc..

1.4.5 Other properties

Furthermore, as for CNTs, the asymmetric axial thermal conductance properties of BNNTs were also found to be remarkable. In addition, BNNTs are predicted to have piezoelectricity [54, 55] and applicable for room-temperature hydrogen storage [56].

1.5 BNNTs synthesis

It has been challenging to grow BNNTs in a high yield. Following the theoretical prediction in 1994, some researches had started to synthesize BNNTs experimentally. Most reliable and well-established techniques for CNT growth such as arc-discharge, laser ablation and chemical vapor deposition (CVD) were modified for the BNNTs synthesis. In the last decade, BNNTs were grown by arc discharge, laser ablation, substitution reactions from CNT, ball-milling, CVD and so on. These BNNTs contain impurities including amorphous boron nitride (*a*-BN) powders and other solid-state by-product [57].

1.5.1 Arc discharge

The arc discharge method that first successfully grew BNNTs was similar to that for growing CNTs [30]. In the case of BNNTs, the anode was built by inserting a h-BN rod into a hollow tungsten electrode and the cathode was a rapidly cooled pure copper electrode. Arc discharge occurred between the tungsten and copper electrodes. The inserted h-BN rod was evaporated indirectly. After the arc discharge, the gray product was deposited on the copper cathode, which contented some scattered single-wall BNNTs. Other successful attempts to grow BNNTs by arc discharge method were using hafnium diboride (HfB_2) electrodes [48] and arcing hexagonal boron nitride (h-BN) and tantalum in a nitrogen atmosphere [59].

1.5.2 Laser-Based Methods

Laser heating is one of the possible methods to synthesize BNNTs as demonstrated by Golberg *et al.* [60]. Single crystal c-BN specimens were laser heated in a diamond anvil cell under high nitrogen pressures. TEM and other characterization techniques confirmed the product to be BNNTs. Another laser-based technique was oven-laser ablation method [61]. The target material was prepared by mixing high-purity h-BN and nanosized Ni and Co powders. The target was then placed inside a long quartz tube heated by a tube furnace. An excimer laser with a wavelength of 248 nm was focused on the target to initiate ablation. At optimum laser pulsed energy and oven temperature (1200 °C), the ablated laser plumes were carried by the flowing gas and collected on the water-cooled copper collector. BNNTs with diameters ranging from 1.5 to 8 nm were obtained together with other amorphous by-products. Comparison of the structure of the BNNTs synthesized with different carrier gases revealed an interesting phenomenon. BNNTs obtained in inert argon and helium gases were dominated with single-wall BNNTs. When nitrogen was used as the carrier gas, the BNNTs were dominated with double-wall structures. No BNNTs with more than four walls were observed.

1.5.3 Substitution Reaction

Because of the nearly identical lattice structure between CNTs and BNNTs, the former were used as the templates to prepare BNNTs. This technique is called CNT-substituted reaction, where carbon atoms of CNTs are substituted by boron and nitrogen atoms [62] according to the reaction formula as follows:

$$B_2O_3 + 3C \text{ (CNTs)} + N_2 \rightarrow 2BN \text{ (BNNTs)} + 3CO \qquad (1)$$

The reaction was performed in an induction-heating furnace. In brief, B_2O_3 powder was placed in an open sintered graphite crucible and then covered with CNTs. The crucible was kept in a flowing nitrogen atmosphere at 1500 °C for half an hour. Followed by cooling, the starting black CNTs were found to turn into gray color. Different characterization techniques confirmed that BNNTs were grown but were mixed with carbon and other BN phases. To purify the product, oxidation treatment could start to oxidize carbon layers around 550 °C and transform these mixed-phase nanotubes into pure BNNTs.

1.5.4 Ball-Milling technique

Ball-milling is a technique that can produce BNNTs at high yield, but it has a disadvantage of low purity [63, 64]. As reported by Chen *et al.*, the ball-milling system has four stainless steel milling vessels with each small vessel loaded with several grams of boron powder and four hardened steel balls. Then, they were filled with ammonia gas at a pressure of 300 kPa prior to milling. With this method, four large vessels could mill powder up to 1 kg. The mechanism behind was the transfer of large amount of mechanical energy into boron powder particles, leading to morphological, structural, and chemical changes. Followed by milling, an isothermal annealing was executed in a tube furnace at 1200 °C for 16 h under nitrogen gas flow. Finally, BNNTs were obtained by converting powder to tubules with the formation yield of 65 ~ 85% [64]. It is noted that most of these BNNTs appeared in bamboo-like structures.

1.5.5 Catalytic CVD

Catalytic CVD (CCVD) is one of the most popular and successful techniques for the synthesis of CNTs and various nanowires. Lourie *et al.* described the growth of BNNTs by using borazine ($B_3N_3H_6$) as the precursor according to the chemical reaction as follows [65]:

$$3(NH_4)2SO_4 + 6NaBH_4 \rightarrow 2B_3N_3H_6 + 3Na_2SO_4 + 18H_2 \quad (2)$$
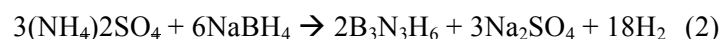
The growth was successful in trials applying different catalysts such as Co, Ni, NiB, or Ni$_2$B. The NiB catalysts were found to be the most effective.. The substrate coated with NiB or Ni$_2$B catalysts was placed in the center of the tube-furnace reactor that was heated to 1000 ~ 1100 °C. These were then exposed to the B$_3$N$_3$H$_6$-containing carrier gas for half an hour. The deposits were observed on the substrate and were identified as MW-BNNTs. Recently, borazine has also been used in conjunction with a floating nickelocene catalyst, resulting in the predominant formation of double-walled BNNTs [66].

1.5.6 BOCVD

Only during the last few years, our group at NIMS has achieved technologically meaningful amounts of multi-walled BNNTs through a method called Boron oxide assisted CVD (BOCVD) [67, 68]. Figure 1.4 shows an illustration of the furnace used for BOCVD. The furnace has two inlets on its top and bottom, and one outlet on its side. This technique uses B and MgO powders as precursors to activate the B source and NH$_3$ as the N source. The product possesses high purity because no carbon is involved in the process. In addition, the precursors and the product are well-separated during the growth. This method was further improved to achieve larger BNNT quantities when SnO was added into the precursor mixture [66]. SnO works as a solvent at high temperature during the reaction between B and MgO. The chemical reactions are given by Eqns. (3) and (4):

$$2B \text{ (s)} + 2MgO \text{ (s)} \rightarrow B_2O_2 \text{ (g)} + 2Mg \text{ (g)} \qquad (3)$$
$$B_2O_2 \text{ (g)} + 2NH_3 \text{ (g)} \rightarrow 2BN \text{ (s)} + 2H_2O \text{ (g)} + H_2 \text{ (g)} \qquad (4)$$
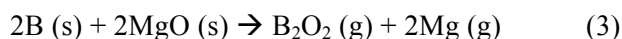
Now it is possible to run a gram order outcome highly-pure BNNT synthesis. For ~ 10 hours synthesis, ~ 1g of BNNTs may be synthesized. Figure 1.5 shows a scanning electron microscopy image of BNNTs synthesized by BOCVD. The phase purity can be up to 90 vol% and there are no carbon impurities as this method is carbon-free synthesis. This method was further improved to achieve larger yields to make it possible a full-scale composite research.

1.5.7 Other methods

Besides, a number of alternative techniques such as liquid flow of FeB nanoparticle [69], electron beam in-situ deposition on a clean tungsten surface in an ultra high vacuum [70], Plasma jet method [71] have also been developed.

Figure 1.4 Illustration of the apparatus to synthesizing BNNTs by the BOCVD method.

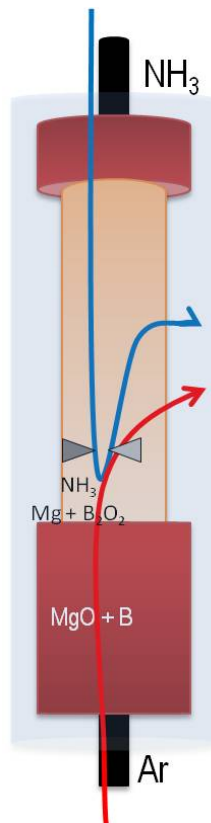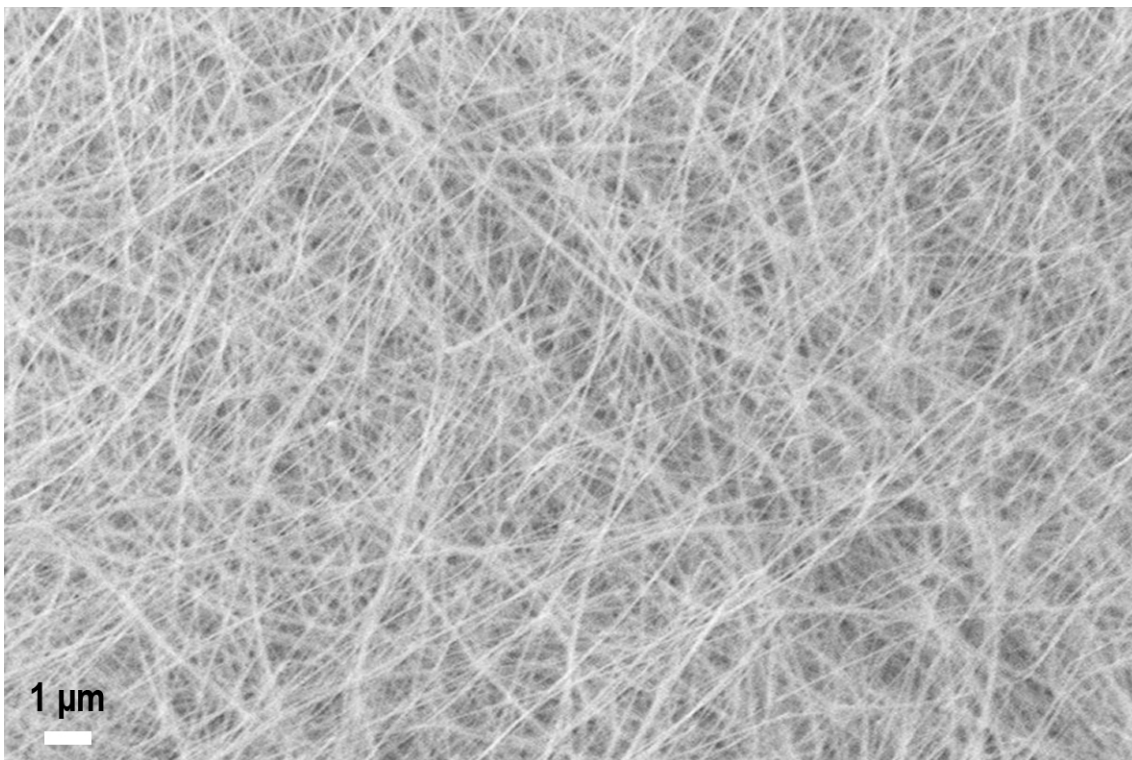**Figure 1.5** A scanning electron microscopy image of purified BNNTs

1.6 BNNTs composite features

Intuitively, needle-like shapes of BNNTs look remarkably preferable for their perfect distribution and even texturing / networking in any given matrix. This feature is due to specific BN structure – (1) having two elements with different electronegativities, B and N, these tubes exhibit a partial ionic contribution to chemical bonding, and there is a charge transfer process. Such tubes are electrical insulators, opposed to metallic or semiconducting CNTs, (2) this type of bonding leads to preferential stacking of tubular multilayers across the tube in such a way that the B atoms like to locate themselves above the N atoms and *vice versa*. This results in perfectly straight appearances of BN nanotubes and makes their texturing in a given matrix possible.

Decent successes have been achieved by us using BNNTs for reinforcing and / or toughening conventional polymers and widespread ceramics [63, 68, 72-74]. The strength, toughness, elasticity and thermal conductivity of polymers and engineering ceramics have dramatically been enhanced, up to 200-300 % by adding marginal amounts of multi-walled BN tubes (only few wt.%).

Golberg's group also measured the true density of BN nanotubes as only ~1.4 g/cm^3 [75]. Therefore, a possible increase of strength and elasticity of a metal matrix by such low density, ultralight, but superstrong reinforcing fibers would allow one to dramatically reduce the carrying-load component dimensions and further dramatically reduce the overall structure weight, decrease fuel consumption, save energy, and reduce pollution effects. Therefore, the ultimate target of the present work is a design, development and fabrication of a new prototype "dream" structural material which would be ultralight, (density of only 2.5 g/cm^3 or less), superelastic (Young's modulus of ~ hundreds of GPa) and superstrong (tensile strength in hundreds of MPa range). We are predicting that such material should be based on a composite hybrid between an Al-based matrix and reinforcing superstrong, ultralight fibers made of straight needle-like multi-walled BN nanotubes.

It is important to mention that BNNT-MMC is still rather rare topic due to the BNNT synthesis difficulties. Only a few reports globally, including ours, have been published with respect to Al-BNNTs composites [76-78]. Singhal *et al.* [79] while using a powder metallurgy route observed an increase of compressive strength and microhardness of Al-BNNT composites compared to non-doped Al powders. Agarwal's group has studied the Al-BNNT chemical interfacial chemical reactions of Al-BNNT and has prepared Al-BNNT composites using SPS method [80]. However, the BNNTs that the both groups utilized were not of preferred morphologies, they possessed so-called bamboo-like structures produced by a ball milling procedure. Such tubes are rather weak (having strength below 8 GPa [81]) compared to well-crystallized nested and long (up to 20 μm) BN tubular cylinders or polygons [36].

1.7 Purpose of this study

Although BNNT is an attractive nanomaterial as shown earlier, yet it has a lot of problems for technological use, especially for composite materials. One of the biggest problems has been the synthesis of pure BNNTs in a high yield. After the discovery of BOCVD method by Bando-Golberg's group, using which BNNT can be produced at ~1 g per day yield, the regarded problem was solved.

Last decade, CNT-MMC composite studies have received an increased attention, especially for Al. MMC-nanotube hybrids allow one to merge a rich variety of functionalities peculiar to nanotubes, e.g. thermal conductivity, electrical conductance, and a huge strength and an excellent elasticity of reinforcing nanotubes. However, with CNTs, there have been some structural issues such as buckling CNTs within a metal matrix or forming carbides with the metals. So it would be a great challenge to try making such composites with BNNTs which are chemically stable and have needle-like shapes. In order to draw a whole and conclusive picture, the BNNTs-reinforced ultralight-weight hybrids were prepared in three different dimension ranges, called nano- (Chapter 2), micro- (Chapter 3) and macrocomposites (Chapter 4), for each scale the specific fabrication and testing methods were designed. And the investigations of Al and BN interaction status, individual mechanical behavior, and structural and mechanical properties were performed toward future applications. Additionally, theoretical characterizations, internal friction measurements and thermal diffusivity measurements on composites were carried out to understand the mechanisms involved.

Al-BNNTs composites would be a promising candidate for future "superlight" and "superstrong" materials for aerospace, aircraft and automotive industries. Based on the Bando-Golberg group's pre-existing successes with BN-reinforced polymeric and ceramic matrices I do believe that this challenge is highly feasible. We expect that it would be possible to employ the huge strength and superb elasticity of BNNTs for ultimate, several fold-time increase of the tensile strength and Young's modulus of ultralight Al. That will allow us to dramatically reduce the demands for sizes (thicknesses) of structural parts of automobiles, aircrafts and spacecrafts. The materials should withstand a given stress under harsh conditions, such as elevated working temperatures of 300 ~ 400 °C, that are typical numbers for the areas of usage of the regarded structural components.

The utilization of such novel superstrong BNNTs-light metals hybrid materials would in-turn decrease the demands for fuel consumption, save energy and, in the long run, reduce the environment pollution.

1.8   References

[1] R. Heuss, N. Müller, A. Starke, A. Tschiesner. Advanced Industries. *McKinsey & Company*. **2012**.

[2] Aero magazine. *Boeing.* **2012**, pp.18-19.

[3] Polmear I. Light alloys: metallurgy of the light metals. 3rd ed. Oxford: Butterworth-Heinemann; 1995.

[4] Ultimate tensile strentgth. (n.d) In *Wikipedia*. Retrieved from
http://en.wikipedia.org/wiki/Ultimate_tensile_strength.

[5] Global Market Forecast: Future Journeys 2013-2032. *Airbus*. **2013**.

[6] B. Pai, T. Rajan, R. Pillai. Indian Foundry. **2004**, 50, 30.

[7] T. Chou, A. Kelly, A. Okura. *Composites*. **1985**, 16, 187.

[8] D. Miracle. *Compos. Sci. Technol.*, **2005**, 65, 2526.

[9] S. Sarkar, A. Singh. *Open J. of Composite Mater.*, **2012**. 2, 22.

[10] C. N. Devi, V. Mahesh, N. Selvaraj. *Int'l J. Appl. Eng. Res.*, **2011**, 1, 793.

[11] R. Arsenault. *Mater. Sci. Eng.*, **1984**. 64, 171.

[12] M. Dave, K. Kothari. *Paripex- Indian J. Res.*, **2013**, 2, 148.

[13] M. MahendraBoopathi, K. Arulshri, N and Iyandurai, *Am. J. Appl. Sci.*, **2013**, 10, 219.

[14] K. Suryanarayanan K, R. Praveen, S. Raghuraman. *Int'l J. Innovative Res. Sci. Eng. Technol.*, **2013**, 2, 6336.

[15] S.R. Bakshi, D. Lahiri, A. Agarwal. *Int. Mater. Rev*. **2010**, 55, 41.

[16] S. Iijima. *Nature.* **1991**, 354, 56.

[17] H.J. Choi, J.H. Shin, D.H. Bae. *Composites: Part A*. **2012**, 43, 1061.

[18] M.H. Vidal-Sétif, M. Lancin, C. Marhic, R. Valle, J.L. Raviart, J.C. Daux, M. Rabinovitch. *Mater. Sci. Eng. A*. **1999**, 272, 321.

[19] H. Kwon, M. Estili, K. Takagi, T. Miyazaki, A. Kawasaki. *Carbon.* **2009**, 47, 570.

[20] A. Esawe, Morsi. *Composites A*. **2007**, 38, 646.

[21] S.R. Bakshi, V. Singh, S. Seal, A. Agarwal. *Surf. Coat. Technol.* **2009**, 203, 1544.

[22] T. Noguchi, A. Magario, S. Fukazawa, S. Shimizu, J. Beppu, M. Seki. *Mater. Trans.* **2004**, 45, 602.

[23] C. Li, Z. Ryu, N.Y. Jin-Philipp, M. Ruhle. *Acta Mater.* **2006**, 54, 5367.

[24] C. Deng, X. Zhang, X. Dezun. *Mater Lett.* **2007**, 61, 904.

[25] D. Poirier, R. Gauvin, R.A.L. Drew. *Composites A*. **2009**, 40, 1482.

[26] H. Kurita, H. Kwon, M. Estili, A. Kawasaki. *Mater. Trans.* **2011**, 52, 1960.

[27] A. Agarwal, S.R. Bakshi, D. Lahiri. Carbon nanotubes: reinforced metal matrix composites. Boca Raton, FL: CRC Press. 2010.

[28] A. Rubio, J. L. Corkill, M. L. Cohen. *Phys. Rev. B*. **1994**, 49, 5081.

[29] X. Blase, A. Rubio, S. G. Louie, M. L. Cohen. *Europhys. Lett.* **1994**, 28, 335.

[30] N.G. Chopra, R.J. Luyken, K. Cherrey, V.H. Crespi, M.L. Cohen, S.G. Louie, A. Zettl. *Science.* **1995**, 269, 966.

[31] C.Y. Zhi, Y. Bando, C.C. Tang, S. Honda, K. Sato, H. Kuwahara, D. Golberg. *Ang. Chem. Int. Ed.* 2005,

44, 7932.

[32] E. Hernandez, C. Goze, P. Bernier, A. Rubio. *Phys. Rev. Lett.* **1998**, 80, 4502.

[33] Chopra, N. G., and Zettl, A., *Solid State Commun* (1998) **105**, 297.

[34] A. P. Suryavanshi, M.F. Yu, J. Wen, C. Tang, Y. Bando. *Appl. Phys. Lett.* **2004**, 84, 2527.

[35] X.L. Wei, M.S. Wang, Y. Bando, D. Golberg. *Adv. Mater.* **2010**, 22, 4895.

[36] D. Golberg, P.M.F.J. Costa, O. Lourie, M. Mitome, X. Bai, K. Kurashima, C.Y. Zhi, C.C. Tang, Y. Bando. *Nano Lett.* **2007**, 7, 2146.

[37] D. M. Tang, C.L. Ren, X.L. Wei, M.S. Wang, C. Liu, Y. Bando, D. Golberg *ACS Nano.* **2011**, 5, 7362.

[38] C.Y. Zhi, Y. Bando, C.C. Tang, D. Golberg. *Mat Sci Eng R,* **2010**, 70, 92.

[39] M. Zheng, X. Chen, I.T. Bae, C. Ke, Cheol Park, M.W. Smith, K. Jordan. *Small,* **2012**, 8, 116.

[40] Y. Xiao, X.H. Yan, J. Xiang, Y. L. Mao, Y. Zhang, J. X. Cao, J.W. Ding. *Appl Phys Lett,* **2004**, 84, 4626.

[41] Y. Xiao, X.H. Yan, J.X. Cao, J.W. Ding, Y.L. Mao, J. Xiang. *Phys Rev B*. **2004**, 69, 205415.

[42] C.W. Chang, A.M. Fennimore, A. Afanasiev, D. Okawa, T. Ikuno, H. Garcia, Deyu Li, A. Majumdar, A. Zettl. *Phys Rev Lett.* **2006**, 97, 85901.

[43] D. Golberg, Y. Bando, K. Kurashima, T. Sato. *Scripta Mater.* **2001**, 44, 1561.

[44] A. Loiseau, F. Willaime, N. Demoncy, G. Hug, H. Pascard. *Phys. Rev. Lett.* **1996**, 76, 4737.

[45] M. Radosavljevic , J. Appenzeller , V. Derycke , R. Martel , Ph. Avouris , A. Loiseau , J.L. Cochon, D. Pigache. *Appl. Phys. Lett.* **2003**, 82, 4131.

[46] Y. Miyamoto, A. Rubio, M.L. Cohen, S.G. Louie. *Phys. Rev. B.* **1994**, 50, 4976.

[47] Y.H. Kim, K.J. Chang, S.G. Louie. *Phys. Rev. B.* **2001**, 63, 205408.

[48] K.H. Khoo, M.S.C. Mazzoni, S.G. Louie. *Phys. Rev. B.* **2004**, 69, 201401R

[49] C.W. Chen, M.H. Lee, S.J. Clark. *Nanotechnology.* **2004**, 15, 1837.

[50] M. Ishigami , J.D. Sau , S. Aloni , M.L. Cohen, A. Zettl. *Phys. Rev. Lett.* **2005**, 94, 56804.

[51] M.F. Ng, R.Q. Zhang. *Phys. Rev. B.* **2004**, 69, 115417.

[52] P. Kral , E.J. Mele, D. Tomanek. *Phys. Rev. Lett.* **2000**, 85, 1512.

[53] J. Kongsted , A. Osted , L. Jensen , P.O. Astrand, K.V. Mikkelsen. *J. Phys. Chem. B.* **2001**, 105, 10243.

[54] E. J. Mele, P. Kral. *Phys. Rev. Lett.* **2002**, 88, 56803.

[55] S. M. Nakhmanson, A. Calzolari, V. Meunier, J. Bernholc, M. B. Nardelli. *Phys. Rev. B.* **2003**, 67, 235406.

[56] S. H. Jhi, Y. K. Kwon, *Phys. Rev. B.* **2004**, 69, 245407.

[57] J. Wang, H. Lee, Y. Bando, D. Golberg, Y.K. Yap. B-C-N Nanotubes and Related Nanostructures, Springer Science + Business Media, LLC. 2009.

[58] A. Loiseau, F. Willaime, N. Demoncy, G. Hug, H. Pascard. *Phys. Rev. Lett.* **1996**, 76, 4737.

[59] M. Terrones, W. K. Hsu, H. Terrones, J. P. Zhang, S. Ramos, J. P. Hare, R. Castillo, K. Prassides, A. K. Cheetham, H. W. Kroto, D. R. M. Walton. *Chem. Phys. Lett.* **1996**, 259, 568.

[60] D. Golberg, Y. Bando, M. Eremets, K. Takemura, K. Kurashima, T. Tamiya, H. Yusa. *Appl. Phys. Lett.* 1996, 69, 2045.

[61] D. P. Yu, X. S. Sun, C. S. Lee, I. Bello, S. T. Lee, H. D. Gu, K. M. Leung, G. W. Zhu, Z. F. Dong, Z. Zhang. *Appl. Phys. Lett.* **1998**, 72, 1966.

[62] W. Q. Han, Y. Bando, K. Kurashima, T. Sato. *Appl. Phys. Lett.* **1998**, 73, 3085.

[63] C.Y. Zhi, Y. Bando, C.C. Tang, S. Honda, H. Kuwahara, D. Golberg. *J. Mater. Res.* **2006**, 21, 2794.

[64] Y. Chen, M. Conway, J.S. Williams, J. Zou. *J. Mater. Res.* **2002**, 17, 1896.

[65] O.R. Lourie, C.R. Jones, B.M. Bartlett, P.C. Gibbons, R.S. Ruoff, W.E. Buhro. *Chem, Mater.* **2000**, 12, 1808.

[66] M. J. Kim, S. Chatterjee, S.M. Kim, E.A. Stach, M.G. Bradley, M.J. Pender, L.G. Sneddon, B. Maruyama. *Nano Lett.* **2008**, 8, 3298.

[67] C.C. Tang, Y. Bando, T. Sato, K. Kurashima. *Chem. Commun.*, **2002**, 1290.

[68] C. Y. Zhi, Y. Bando, C.C. Tang, D. Golberg. *Solid State Commun.*, **2005**, 135, 67.

[69] K.P. Loh, M. Lin, M. Yeadon, C. Boothroyd, Z. Hu. *Chem. Phys. Lett.* **2004**, 387, 40.

[70] E. Bengu, L.D. Marks. *Phys. Rev. Lett.* **2001**, 86, 2385.

[71] Y. Shimizu, Y. Moriyoshi, H. Tanaka, S. Komatsu. *Appl. Phys. Lett.* **1999**, 75, 929.

[72] D. Golberg, Y. Bando, C.C. Tang, C.Y. Zhi. *Adv. Mater.* **2007**, 19, 2413.

[73] C.Y. Zhi, Y. Bando, T. Terao, C.C. Tang, H. Kuwahara, D. Golberg. *Adv. Funct. Mater.* **2009**, 19, 1857.

[74] Q. Huang, Y. Bando, X. Xu, T. Nishimura, C.Y. Zhi, C.C. Tang, F.F. Xu, L. Gao, D. Golberg. *Nanotechnology.* **2007**, 18, 485706.

[75] C.Y. Zhi, Y. Bando, D. Golberg. *Solid State Commun.***2010**, 151, 183.

[76] J.J. Xu, Y.J. Bai, W.L. Wang, S.R. Wang, F.D. Han, Y.X. Qi, J.Q. Bi. *Mater. Sci. Eng. A.* **2012**, 546, 301.

[77] M. Du, J.Q. Bi, W.L. Wang, X.L. Sun, N.N. Long, Y.J. Bai. *Mater. Sci. Eng.* **2011**, 530, 669.

[78] W.L. Wang, J.Q. Bi, K.N. Sun, M. Du, N.N. Long, Y.J. Bai. *J. Am. Ceram. Soc.* **2011**, 94, 2304.

[79] S.K. Singhal, A.K. Srivastava, R. Pasricha, R.B. Mathur. *J. Nanosci. Nanotechnol.* **2011**, 11, 5179.

[80] D. Lahiri, V. Singh, L.H. Li, T. Xing, S. Seal, Y. Chen, A. Agarwal. *J. Mater. Res.* **2012**, 27, 2760.

[81] D.M. Tang, C.L. Ren , X.L. Wei, M.S. Wang, C. Liu, Y. Bando, D. Golberg. *ACS Nano.* **2011**, 5, 7362.

Chapter 2

Nanocomposites

2. Nanocomposites

Chapter 2 Nanocomposites

2.1   Introduction

Although carbon nanotube (CNT) reinforced light metals composite studies are getting popular, still there is a very few metal matrix composite (MMC) studies using BNNT. Since BNNTs are chemically stable, far more than CNTs, it would be an interesting issue on how BNNTs interact with the metals in MMC composites. For the first step, I studied the Al-BNNTs nanocomposites to understand their morphologies and structures, and mechanical properties. Physical vapor deposition (PVD) methods were chosen for Al-BNNT nanocomposite fabrications.
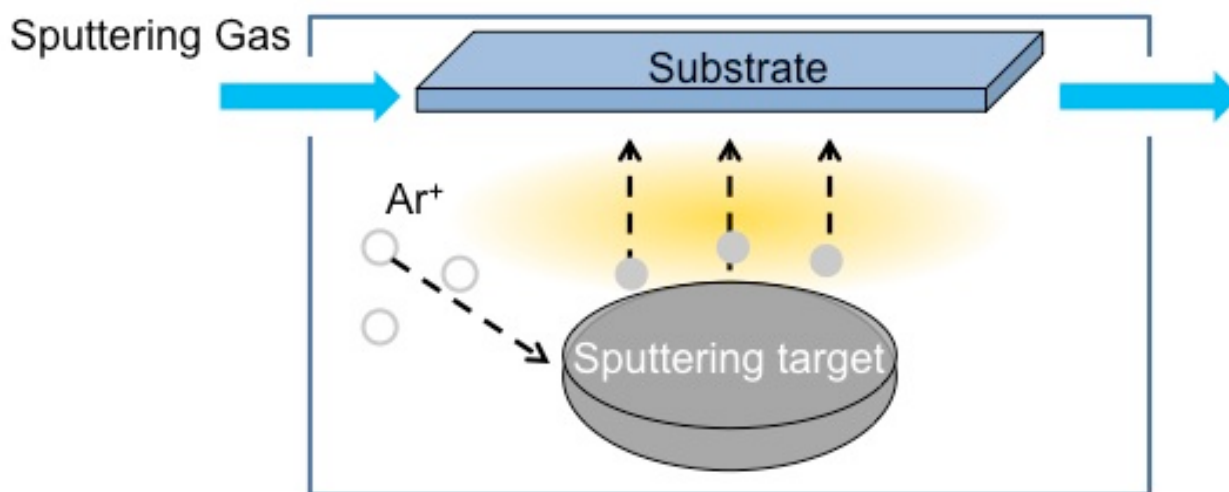
Figure 2.1 Schematic image of sputtering deposition.

PVD represents a variety of vacuum deposition methods used to deposit thin films by the condensation of a vaporized form of the desired film material onto various surfaces. Variants of PVD include cathodic arc deposition, electron beam physical vapor deposition, evaporative deposition, pulsed laser deposition and sputter deposition. Sputter deposition uses a glow plasma discharge (usually localized around the "target" by a magnet) that induces the material sputtering as a vapor for subsequent deposition. Figure 2-1 shows a schematic image of sputtering deposition. It is common coating technique for flat panel display making that requires flat coating at the nanoscale range of dimensions. Although some metal coating CNT studies were performed, sputter deposition is not so popular technique for processing CNT-MMC and only a few reports may be found. For example, Ci et al. fabricated Al-CNT composite films by sputtering pure Al on aligned multi-walled CNT arrays to study interfacial reaction between Al and CNT [1]. It was mentioned that there had been no Al-C compounds or oxide materials formed during the deposition process. Zhang et al. fabricated one-dimensional nanoscale (nanowires) composites based on coatings of CNTs with tungsten by PVD [2]. Apart from PVD methods, having CNTs metal coatings produced by other techniques is a hot topic

for many applications such as making metallic nanowires which have good electrical and magnetic properties [3-7] or tribological applications [8].

It is important to choose processes that can produce uniform coatings and at the same time would not damage the nanotube cores. Since there have been no reports that sputter deposition may cause any damage to the nanotube cores, sputtering may be suggested to a right choice to coat nanotubes with metal. In order to elucidate the regarded working principle of the proposed reinforcement approach, in this section we for the first time fabricated, bent and tensile tested the individual BNNTs- reinforced Al-based nanohybrid using an atomic-force microscopy (AFM) setup compatible with TEM.

2.2   Experimental conditions

BNNTs were dispersed into ethanol and the BNNT/ethanol solution was spread onto substrates. A magnetron sputtering machine (CFS-4EP-LL, Shibaura Mechatronics Corp.) using a pure Al target (99.99 %, 75 mm in diameter) at room temperature was utilized. Argon gas was introduced as a sputtering gas at a flow rate of 20 sccm. The total gas pressure was 0.5 Pa and the base pressure was set to less than 5.0×10^{-4} Pa. DC power supply was used at 200 W. A distance between the target and the substrate with dispersed nanotubes was fixed to 110 mm. Before the Al deposition, the "pre-sputtering" was carried out for 3 minutes to establish the steady state of the target surface. The thickness of the Al coating onto BNNT core was controlled by changing the sputtering time. The range of targeted nominal Al thicknesses varied from 5 nm to 300 nm.

The phase composition and crystal structures of the prepared nanohybrids were analyzed by X-ray diffraction (XRD) (RINT2000 Ultima III, Rigaku) using Cu K_{α} radiation. Also, the morphologies, micro- and atomic structures of the nanocomposites were studied by scanning electron microscopy (SEM) (S4800, Hitachi) and transmission electron microscopy (TEM) (JEM-3000F and JEM-3100FEF (Omega filter) instruments, JEOL). To prepare TEM samples, Al was sputtered directly onto a carbon-coated 3 mm Cu TEM grid with dispersed BNNTs on it. The sputtering direction was adjusted to be perpendicular to the grid plane. Energy dispersive X-ray spectrometry (EDS) (EMAX EX-220, Horiba, and JEM-3100FEF microscopes, respectively) under SEM and TEM at accelerating voltages of 10 kV (SEM) and 300 kV (TEM) was employed to identify the nanocomposite chemistry and to spatially map the constituting species.

Chemical states of the nanohybrids after the initial sputtering stages were analyzed by X-ray photoelectron spectroscopy (XPS) (Theta Probe, Thermo Fisher Scientific). All the spectra data were identified by the NIST X-ray photoelectron spectroscopy database.

Direct *in situ* bending and tensile tests on individual Al-BNNT nanocomposite samples were carried out at room temperature by using an integrated AFM holder (Nanofactory Instruments) inside the TEM (300 kV JEM-3100 FEF, JEOL equipped with a 2K × 2K CCD camera for imaging) [9-13]. Video recording of the deformation cycles was performed using conventional film grabber software. To construct a deformation set-up, firstly, multi-walled BN nanotubes were placed onto the edge of a gold microwire by scratching the wire

over the prepared BNNT powder debris. Then, the tip with physically adhered several BNNTs was coated with Al through magnetron sputtering. It was then inserted into the movable part of the TEM-AFM holder. Calibration of the AFM cantilever and aligning processes of the individual nanocomposites were carried out before all bending and tensile tests. The spring constant of the AFM cantilever was measured to be 6.9 Nm^{-1} by pushing a blank Au tip against the cantilever and recording the force - displacement curve. Then the height of the chosen nanohybrid was adjusted to the AFM cantilever based on the focusing conditions and utilizing a standard wobbler TEM function. The orientation of the nanocomposite sample was set to be nearly perpendicular to the cantilever by three-dimensional piezo-controlled movements of the gold tip with placed Al-BNNT nanohybrids at a precision better than 1 nm. For reliable clamping of the sample to the gold tip and AFM cantilever during the nanomechanical tests, two tiny candle wax droplets were placed ~2 mm away from the tip and cantilever ends, and the electron beam was focused onto the sample/tip and sample/cantilever interfaces for a few minutes to induce electron beam induced (EBID) amorphous carbon deposition. By choosing suitable electron beam conditions, the clamps were highly localized close to the nanocomposite ends, while their surface remained free of carbon contamination. Thus rigid clamping between the densely Al-coated BNNT sample and the Si cantilever, and the gold wire was achieved. The experimental setup for making the amorphous C clamps and performing direct bending and tensile tests is illustrated in Figure 2.2. The insets in Figure 2.2 show the corresponding high-resolution TEM (HRTEM) images of the sample/amorphous C clamp interfaces at the two ends of a nanohybrid. The nanocomposite was bent or stretched under corresponding delicate forward or backward movements of the gold wire placed on the piezo-motor driven unit of the holder. During the sample tension, the tensile forces and real time videos were recorded in parallel, and the tensile stresses and elongations were subsequently calculated. Parallel HRTEM images were also taken for the exact measurements of the nanocomposite cross-sections and analysis of the deformation kinetics and fracture mechanisms. During the tensile tests, the relative Z-position of a composite hybrid inside TEM, relative to the cantilever's height, was maintained by continuous focusing conditions monitoring. However, it was still practically difficult to ensure that the sample was exactly aligned with the cantilever. Therefore, the length, displacement and elongation of the nanocomposites were calculated by considering the angle between the tested nanohybrid and the deflection direction of the cantilever, and the height difference. And the stress was calculated as:

$$\sigma = \frac{k\Delta x/\cos\theta}{S} \quad (1)$$

, where S is the cross-sectional area of the sample, k is the spring constant, Δx is the deflection of the cantilever and θ is the angle between the specimen axis and the direction of the cantilever deflection.
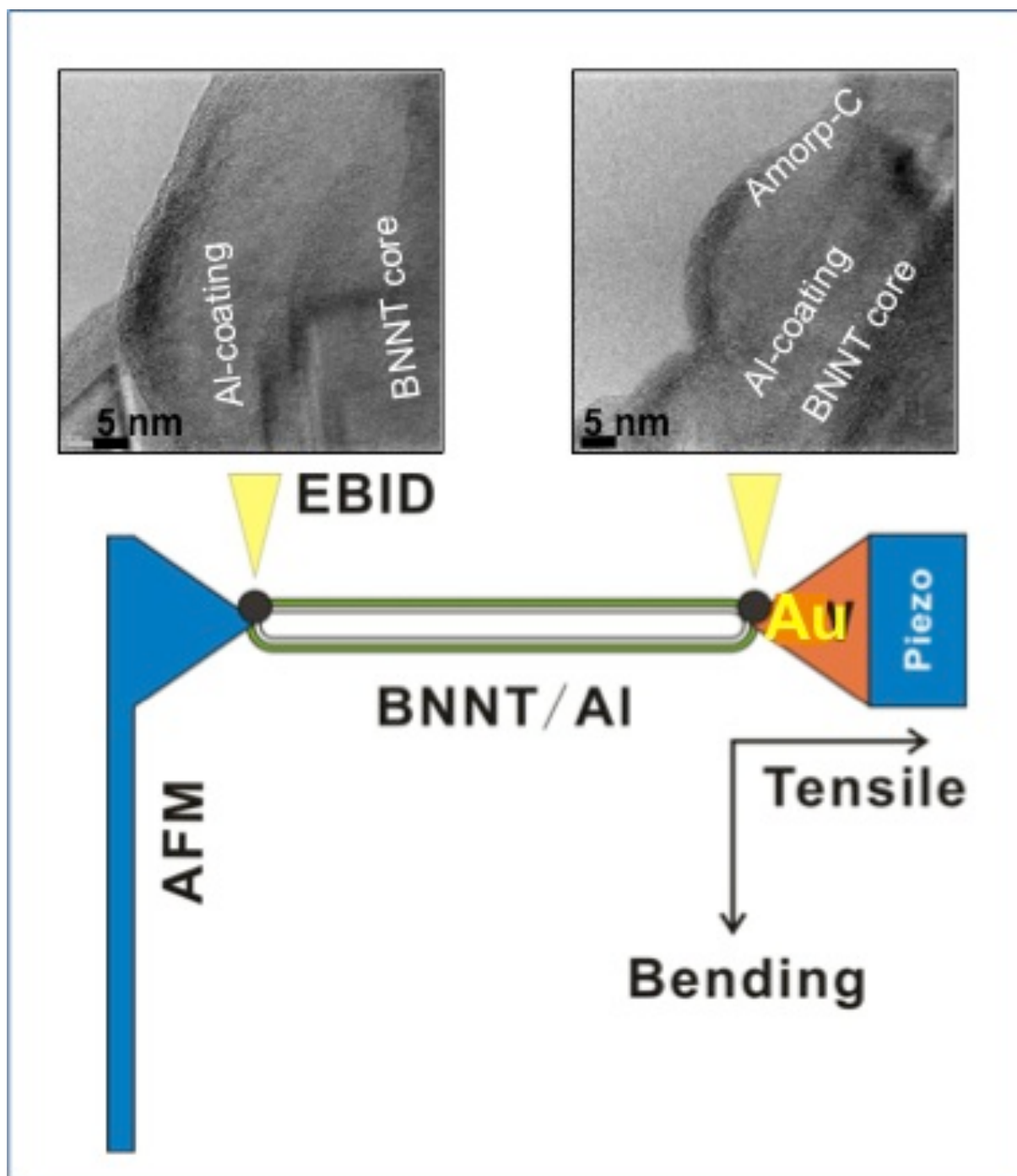
Figure 2.2 Experimental setup for in situ TEM bending and tensile tests on individual Al-BNNT composite nanohybrids; the insets show HRTEM images of a nanocomposite sample in the vicinity of amorphous carbon clamps created by using electron-beam-induced deposition (EBID). The structural details on interest discussed within the text are marked

2.3   Structural and chemical characterizations of Al-BNNTs nanohybrids

The synthesized Al-BNNT nanocomposites entirely preserved a one-dimensional straight morphology peculiar to the starting multi-walled BNNT templates. The thickness of the Al coating became larger in proportion to increased sputtering time. X-ray diffraction patterns of the Al-BNNT nanocomposites with decently thick (~ 200 nm) Al coatings revealed the clear peaks which were identified to a hexagonal BN (0 0 2) plane (ICSD #: 027987), and Al (1 1 1), Al (2 0 0) and Al (2 2 0) reflections (ICSD #: 044321) as shown in Figure 2.3. Other intense visible peaks were from a sample holder or a substrate. This implies that the BN phase remained untainted, and no new B- and/or N- containing Al compounds, such as nitrides (AlN) or borides (AlB_2), formed during sputtering. Some reports have shown similar results [1, 14-16], but in some others new peaks peculiar to boride or nitride compounds were noticed. However, in the latter cases the contents of BN nanotubes were quite low [17], or the samples were bulky [18, 19], or they had undergone prolonged heat treatments.

In order to further confirm the presence of the desired Al coatings on BNNTs, detailed SEM and TEM observations were conducted. SEM images, shown in Figure 2.4, demonstrate that sputtered Al thickness is indeed coincident with the expected sputtering rate. The nominal Al layer thickness (as was set for a magnetron sputtering) varied from 5 nm to 300 nm. Figure 2.5 displays the EDX analysis data obtained from a representative Al-BNNT sample coated with a 200 nm Al layer (Figure 2.5 (a). Although the light elements (B and N) region is not well resolved (inset in Figure 2.5 (a)), a clear and strong Al peak is apparent. Traces of oxygen are also visible. Figure 2.5 (b) shows spatial distribution of Al within the sample. The Al intensity is clearly seen on all one-dimensional morphologies, thus confirming a uniform metal coating on all dispersed BNNTs. Figure 2.6 depicts representative TEM and HRTEM images of individual Al-BNNT nanocomposites of various thicknesses together with selected area electron diffraction (SAED) patterns. It is again obvious that the coating thickness increases with increasing sputtering time. Also it is apparent that the coatings appear to be polycrystalline for all thicknesses studied. As particularly seen in Figure 2.6 (a) and (b), multi-walled BN nanotube cores remain undamaged under the coated Al shield. The DP reflections come from the core BNNT arms and surrounding Al nanocrystals (as marked in the insets to Figure 2.6 (a, c, and e). It is noted that during sample tilting in TEM (up to ±20° in X-Y directions, Figure 2.7 its appearance does not change, implying uniform Al coatings over the entire tube surface Figure 2.7. Thus the sputtered Al phase had uniformly wrapped the BN nanotube cores.

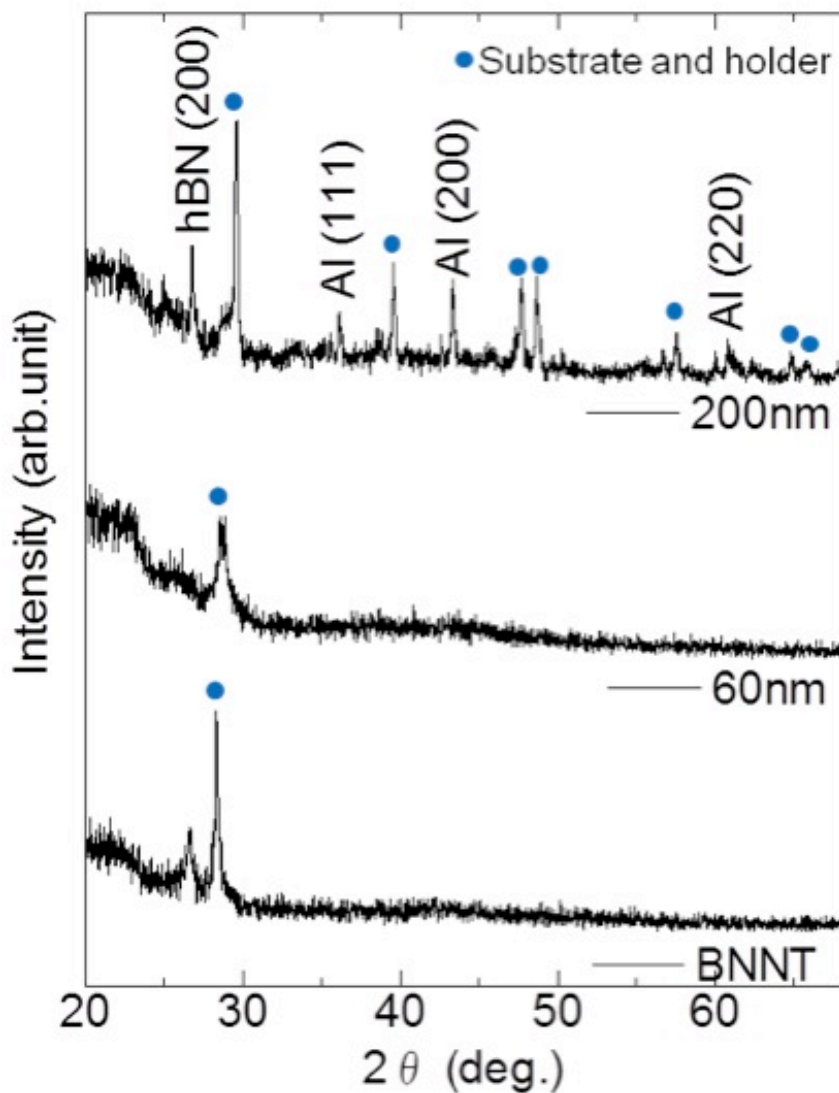**Figure 2.3** XRD spectra of BNNT and Al-BNNT hybrids with 60 nm and 200 nm thickness of Al coatings. BNNT is single-crystalline and Al is polycrystalline within the composite.
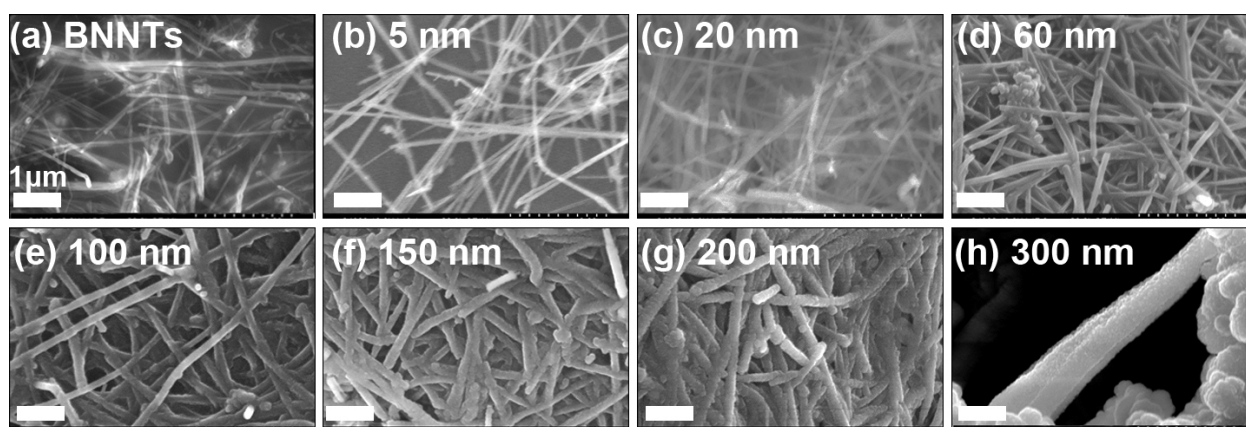

Figure 2.4 Representative SEM images of Al-BNNT nanocomposites with various nominal thicknesses of Al coatings (as set for sputtering condition). The coating thickness proportionally increases with increasing sputtering time.
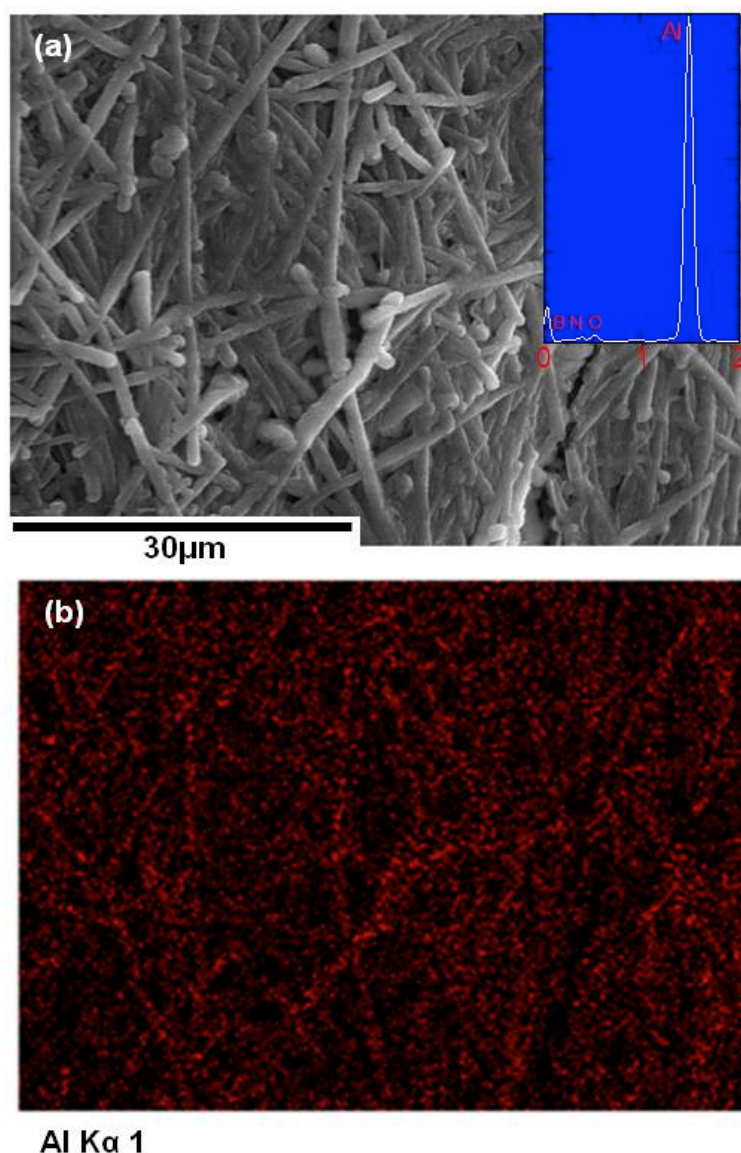
Figure 2.5 (a) SEM image of a representative Al-BNNT nanohybrid with a 200 nm Al layer; and (b) its EDX Al Kα mapping. The inset (a) shows a recorded EDX spectra displaying strong Al and weak O peaks coming from the coating, and weak B, N peaks originating from the core multi-walled BNNTs. (*X* axis: keV; and *Y* axis: counts (arbitrary units))

XPS was used for the elemental analysis of B, N, O and Al states to determine the chemical bonding nature during the initial stages of sputtering. Figure 2.8 displays a survey XPS spectrum of a BNNT with an Al 20 nm coating on a Si wafer. In terms of binding energies, the peaks at ~73 eV, 191 eV, 398 eV and 532 eV correspond to the Al2p, B1s, N1s and O1s, respectively. Figure 2.9 shows enlarged XPS spectra of Al2p, B1s, N1s and O1s on the sample surface. There are two peaks of Al (Figure 2.9 (a)). One weaker peak at 71.9 eV indicates metallic Al and the other main peak at 74.8 eV is peculiar to Al_2O_3.

The described XPS results imply three major conclusions: (i) Al coating may be oxidized during sputtering (e.g. this explains a minor O peak for the EDX spectrum in Figure 2.5); (ii) multi-walled BN

25

nanotube cores entirely withstand the magnetron sputtering without losing integrity of B-N bonds and straight morphology of well-structured shells; (iii) no intermediate and interfacial boride or nitride phases, e.g. AlB_2 or AlN, have been formed between the BN tube cores and Al coats during sputtering in line with the XRD data discussed above. The described facts conclusively show that magnetron sputtering at room temperature, being a relatively simple and straightforward procedure, is fully able to produce desired individual Al-BNNT nanocomposites with various thicknesses of Al phase shields. Compared to other methods of making nanotube-loaded MMC, e.g. powder metallurgy, it does not require a multi-step procedure involving high pressures and/or high temperature treatments [17, 20]. Fabricating metal-BNNT
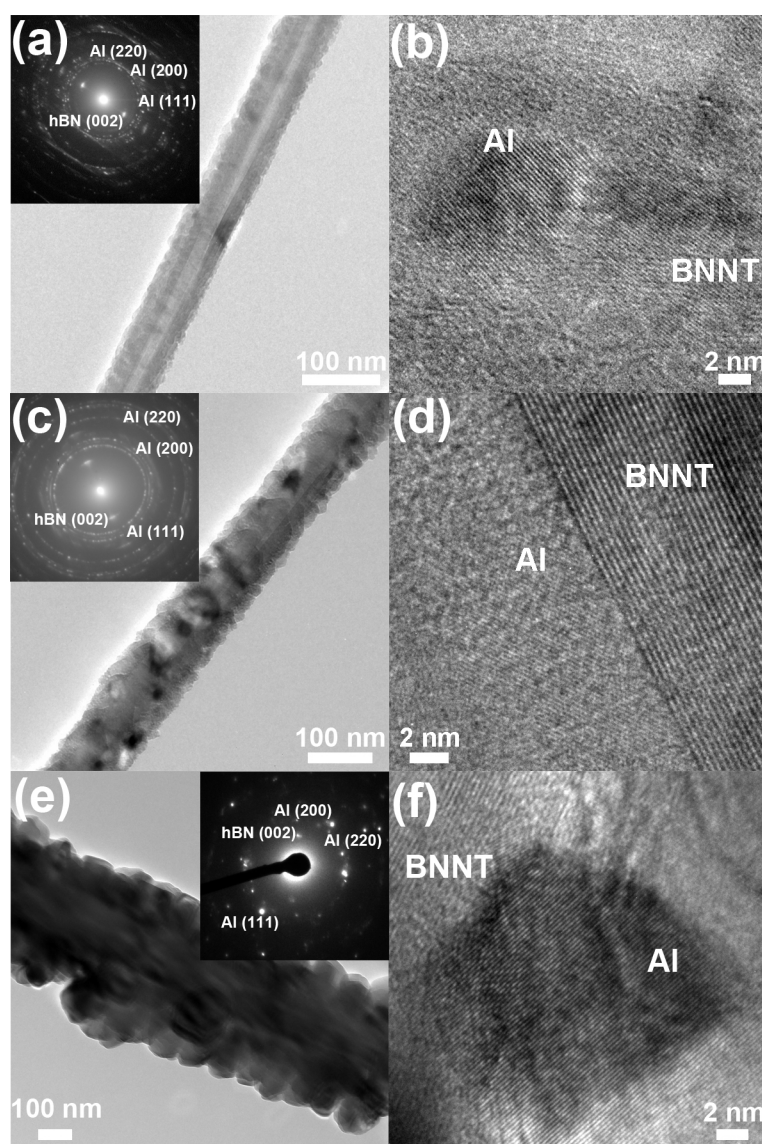
Figure 2.6 (a, c, e) Low-magnification and (b, d, f) high-resolution TEM images showing various nanohybrids and the interfaces between Al phase and the multi-layered BNNT external walls of a Al-BNNT nanocomposite. (a, b) a nanohybrid with a 20 nm Al layer thickness, (c, d) one with a 30 nm Al layer and (e, f) one with a 200 nm Al layer; excellent crystallinity of the BN walls is clearly preserved as seen on all images. The insets show indexed selected area electron diffraction (SAED) patterns, characteristic of polycrystalline Al coatings on well-structured BNNTs.

nanocomposites was also reported during BNNT synthesis by chemical vapor deposition (CVD) using a metal catalyst [21]. However, in the latter case it was impossible to control the desired amount of metal within a composite. It is emphasized that, to date, there have been only a few reports pertaining to metal (i.e. gold [22], nickel, titanium and aluminum [23, 24]) coatings on BNNTs. Chen et al. [22] used sputtering to improve the field emission properties, whereas Obrastsova et al. [23, 24] used a destructive ion-implantation method to coat nanotubes and/or fill them with metals. The data acquired in our present work show that the regarded magnetron sputtering procedure is an effective tool for the realization of multiple merits of BN nanotubes and their metal composites in various branches of technologies such as electronics, mechanics, etc.
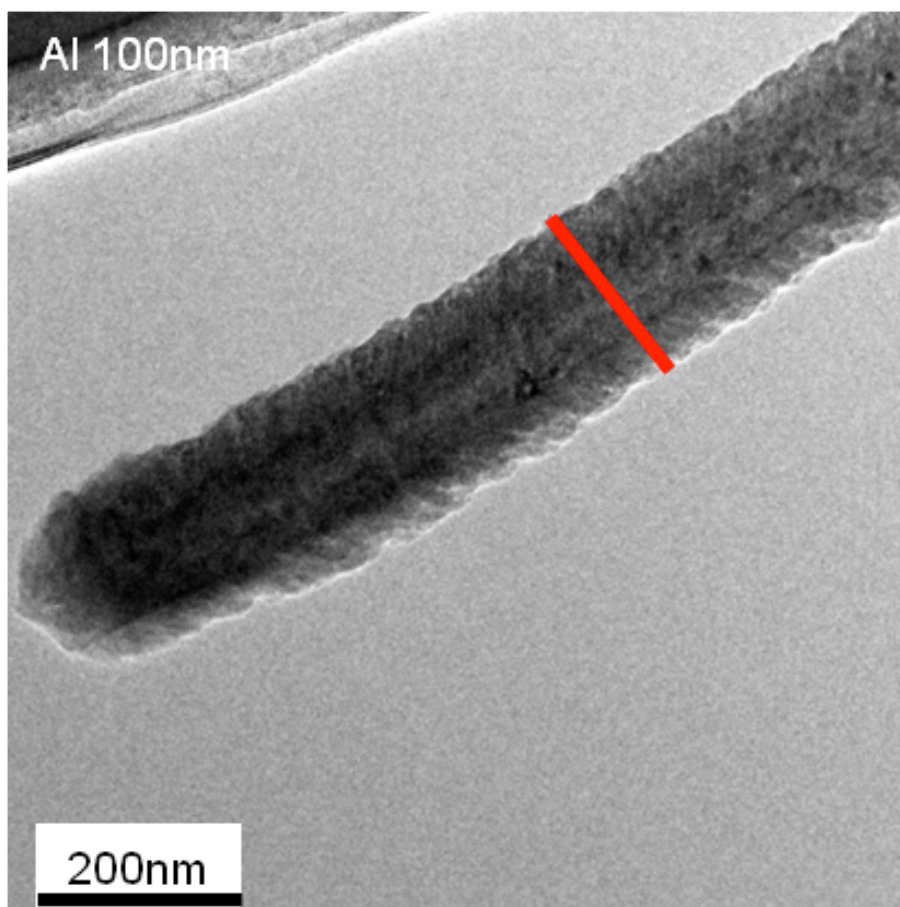
Figure 2.7 TEM image of an Al-BNNT nanocomposite coated with a 40 nm layer of Al and tilted inside TEM, the coating thickness apperance does not notably change (a red bar shows its original thickness
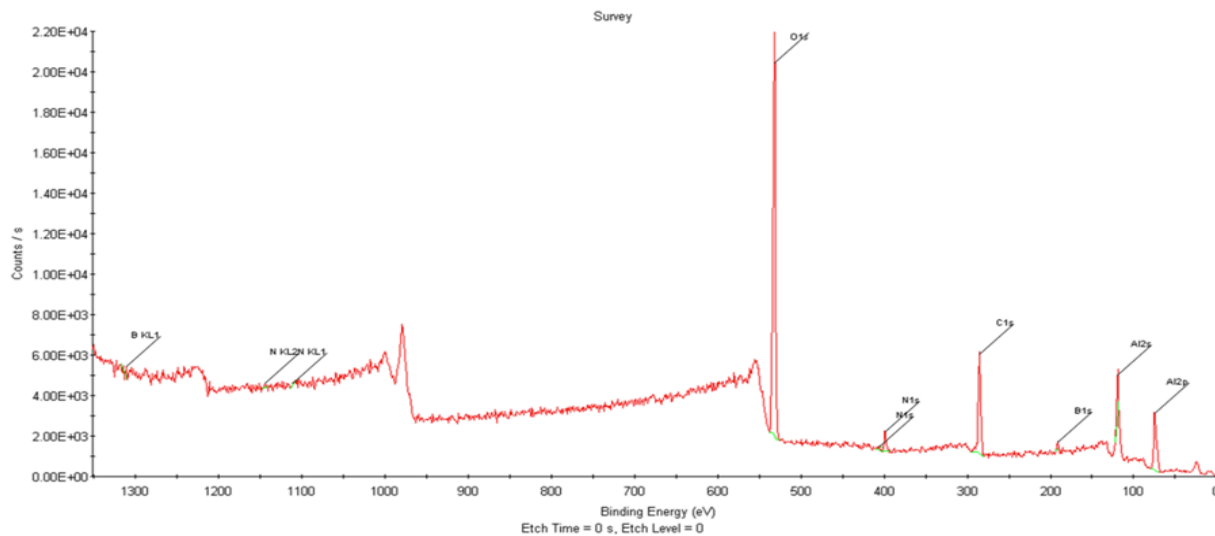
Figure 2.8 XPS survey spectrum of an Al (20 nm nominal thickness)-BNNT nanocomposite. Carbon signal at ~ 284 eV is used as a reference.
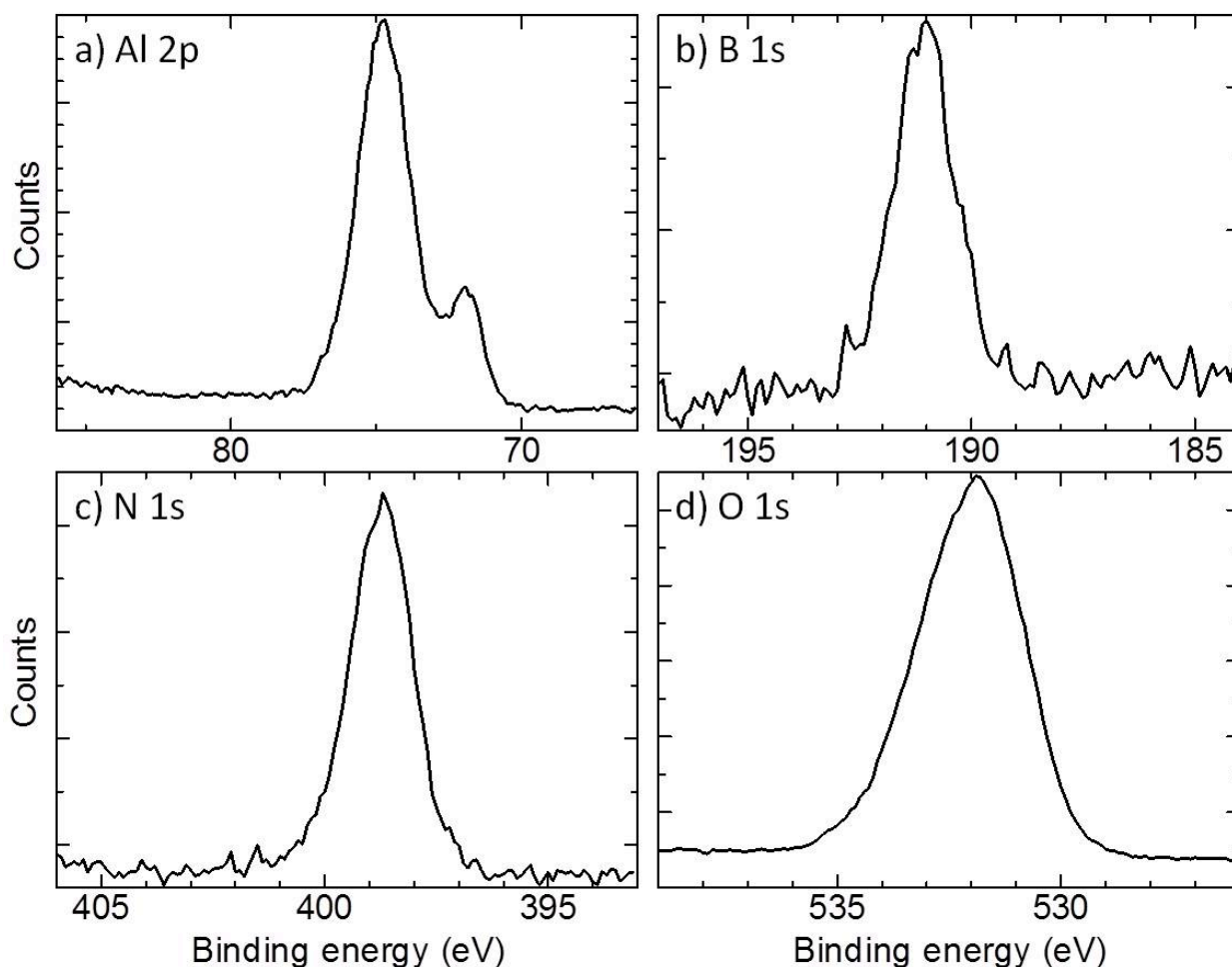
Figure 2.9 XPS spectra (Al 2p, B 1s, N 1s and O 1s) of a Al-BNNT hybrid with a 20 nm Al layer thickness. The Al spectra in (a) indicate metallic Al (73 eV) and Al in Al oxide (74.8 eV); (b, c) B-N bonded phase; and (d) oxygen in Al oxide.

2.4   *In-situ* mechanical tests

At first, bending tests were carried out for an individual Al-BNNT nanocomposite covered with a 40 nm layer of Al. The data are presented in Figure 2.10. Initially, the nanohybrid had a straight morphology inheriting this shape from a starting BNNT template Figure 2.10 (a). Under bending, it turned into an "S" shape with a bending strain concentrated at the middle and close to the clamp portions, respectively Figure 2.10 (b-d). After that, the nanocomposite fractured at a maximum bending angle of 50° (Figure 2.10 (e)). The failure started within the Al shield, whereas the nanotube core initially survived; it broke only at the final stage of bending. In order to get deeper insights into the deformation kinetics, detailed microanalysis of this experimental run using TEM was carried out, as illustrated in Figure 2.11. The starting status of the BNNT with a 100 nm Al coating nanohybrid is depicted in Figure 2.11 (a-c) at different magnifications. An ultimately straight BNNT core is surrounded by a thick Al shield with numerous Al nanoparticles seen Figure 2.11 (b and c). After bending and breakage of the nanocomposite (Figure 2.11 (d)) the broken BN core was partly pulled out of the Al shield (Figure 2.11 (e)). The failure of the core took place in a characteristic "sword-in-sheath" fashion peculiar to inorganic nanotubes [25]. Overall, under bending the Al-BNNT nanocomposite revealed decent toughness. The crack initiated on the tensed side of the sample and did not propagate through the entire nanocomposite directly and immediately. It was likely deflected by
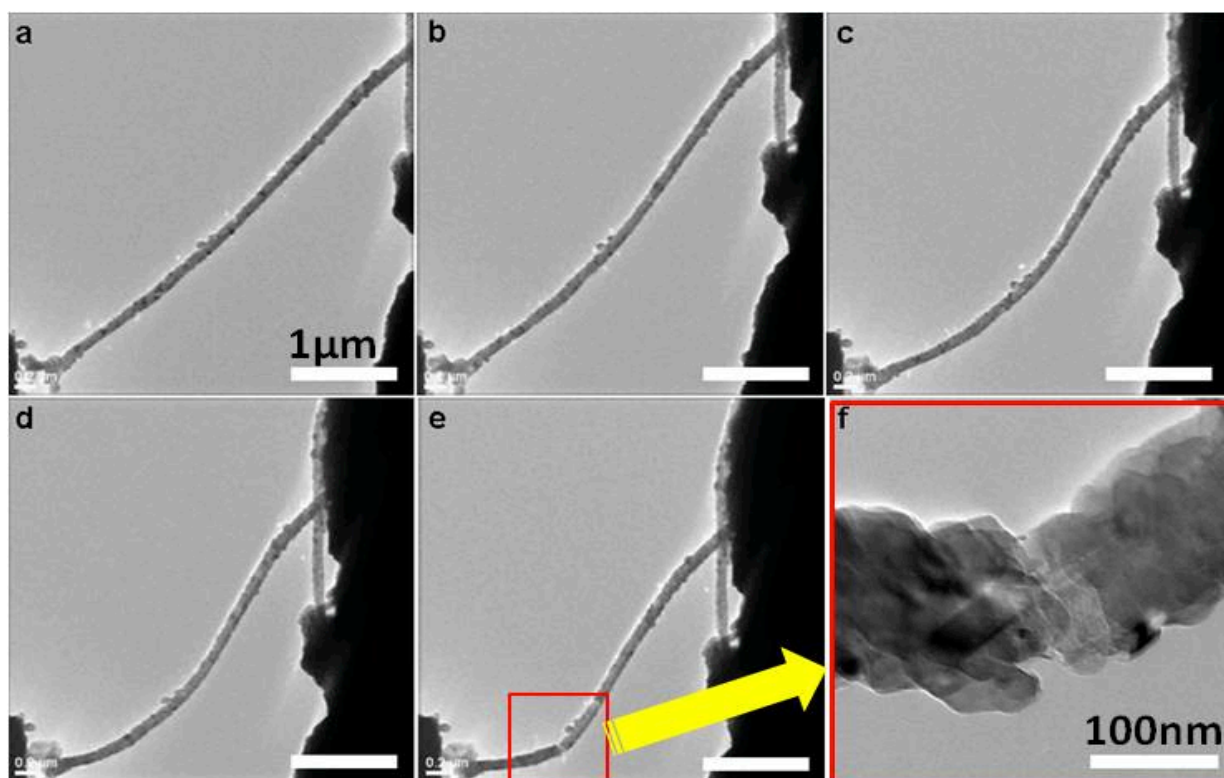

Figure 2.10 Representative direct in situ TEM bending test on an individual Al-BNNT nanocomposite coated with a 40 nm Al layer. (a-c) Consecutive TEM images of the bending process; scale bars indicate 1 μm. (f) Enlarged HRTEM image of the fractured portion. The multi-walled BNNT core becomes visible at this portion.

numerous Al nanoparticles and probably followed the path of the particle boundaries network, thus facilitating the effective dissipation of strain.

Under tension (Figure 2.12 (a)), an individual Al-BNNT nanocomposite covered with a 40 nm layer of Al elongated uniformly, showing clear strain contrasts within the Al phase, indicative of strong interfacial bonding and an effective stress transfer at the nanotube/metal composite interface. Until the mechanical limit of our measurement setup (6000 nN), the Al-BNNT nanocomposites responded purely elastically to the tensile force, as shown in Figure 2.12 (b), withstanding the tensile stress of at least 0.36 GPa. It is noted that we had to terminate the stretching experiment due to reaching the MEMS sensor its force limit; thus, the present nanohybrid is definitely stronger than that number. To compare: the ultimate tensile strength of a typical metallic Al has been known to be only ~40 MPa. Thus the present Al-BNNT nanohybrids can indeed be dramatically strengthened with respect to a non-armed pure Al metal, revealing a striking, approximately nine times enhancement of the tensile strength. An interfacial stress transfer and deformation mechanisms
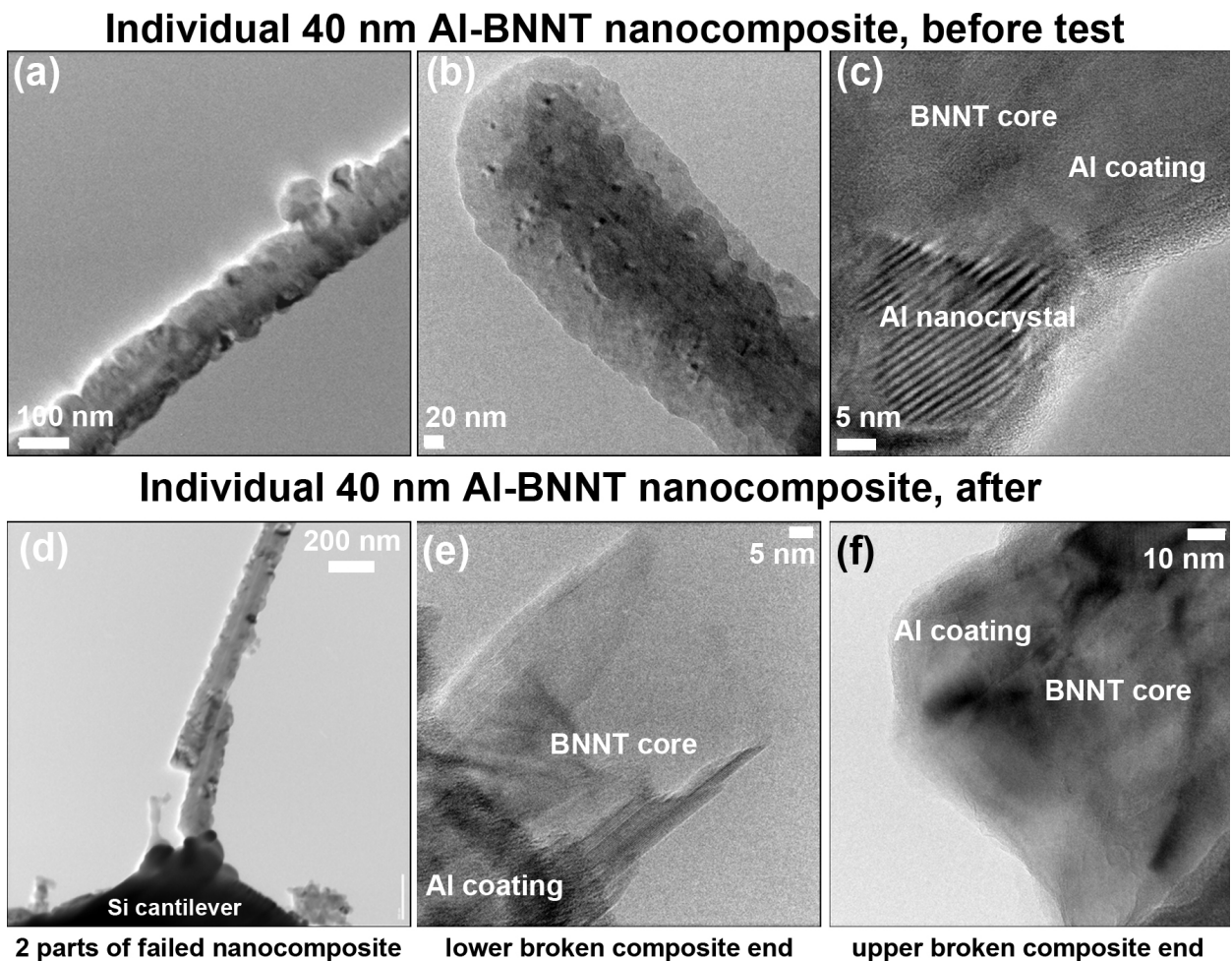

Figure 2.11 Structural details related to the bending experiment of Figure 2-10 (a-c). Characteristic TEM images of an Al-BNNT nanocomposite coated with a 40 nm Al layer before bending and clamping at various magnifications. (d-f) TEM images of a broken nanohybrid after the bending test at various magnifications. See text for details.

are very important for understanding recently discovered behaviors of the fabricated composites. Because of the entire electron scattering overlapping from Al crystals and BNNT shells on TEM images (i.e. the interface could not be clearly viewed edge-on without coming signals from the front and back portions of the Al shields along the electron beam direction) it is difficult to observe the Al-BNNT interface under clear atomic resolution. Cross-sectional TEM samples of composites were prepared by using a focused ion beam (FIB) technique; however, BNNTs were destroyed by high energy ion beams, leaving only Al crystals behind. It is particularly noted that no plastic deformation was observed in our experiments and the samples were fractured within the elastic range. We thus attempted to calculate the stresses within the BNNT cores (σ_{BN}) and Al coatings (σ_{Al}) using the following formula:

$$\sigma_{BN,Al} = \frac{F \times E_{BN,Al}}{S_{BN}E_{BN}+S_{Al}E_{Al}} \qquad (2)$$
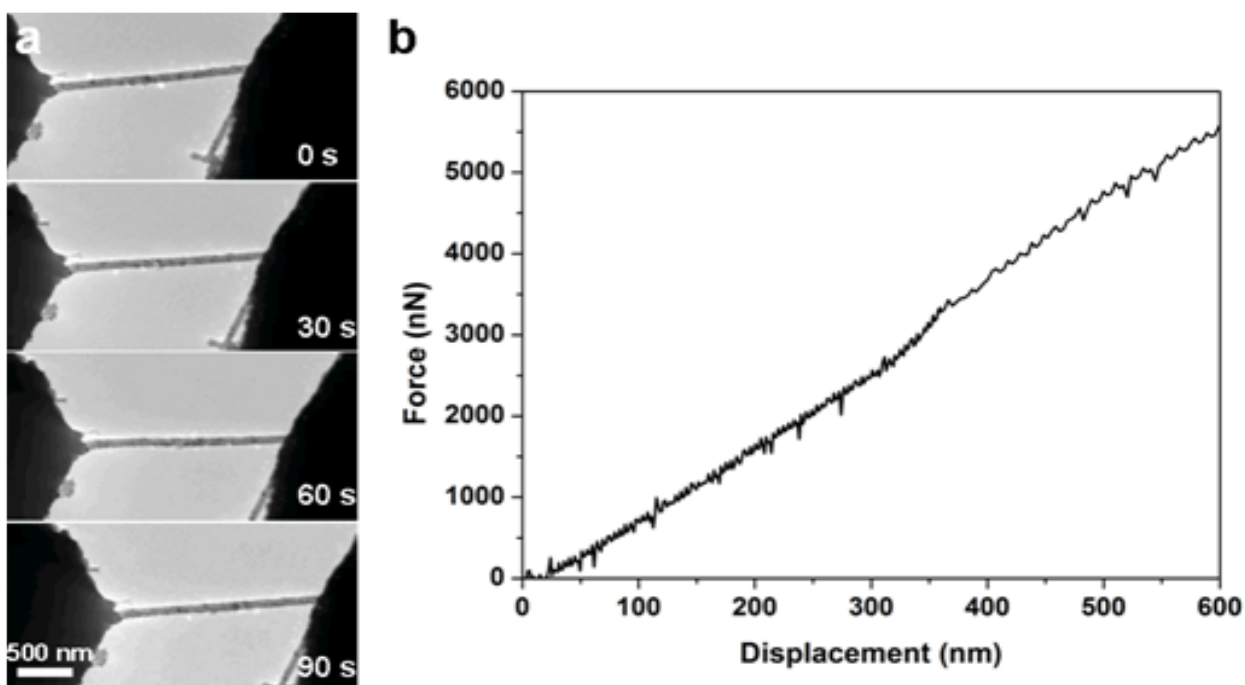
Figure 2.12 Representative direct in situ TEM tensile test on an individual Al-BNNT nanohybrid coated with a 40 nm thickness Al layer. (a) Consecutive TEM images displaying the elongation process in time. (b) A plot of measured force against the cantilever displacement. The reached tensile strength was calculated to be at least ~ 0.36 GPa (tensile loading was terminated at a ~ 600 nm displacement due to reaching the force limit of the experimental setup). A change in the serration appearance on the plot in (b) was caused by an abrupt increase in the deformation rate at a displacement of 370 nm.

in line with the elastic theory, where F is a force, E_{Al} and E_{BN} are the Young's modulus of bulk Al and in-plane elastic modulus of a hexagonal BN phase, respectively, and S_{Al} and S_{BN} are the corresponding cross-sectional areas of the two phases in a given composite. The stresses in BNNT domain and Al coating for a representative BNNT with an Al 20 nm coating sample were calculated to be 3.52 GPa and 0.24 GPa, respectively. In addition, during all the mechanical tests, the TEM contrast due to stresses was solely

31

observed within the Al crystals. Neither dislocations nor Al crystal relocations were found under tension. Sometimes the inner tubular shells of the BN core may even be pulled out of the outer BN layers rigidly fixed to the Al shield, as discussed later.

Figure 2.13 TEM and HRTEM images of fractured Al-BNNT nanocomposites (a-c) a BNNT coated with 20 nm of Al, fractured in tension, HRTEM image in (b) corresponds to the r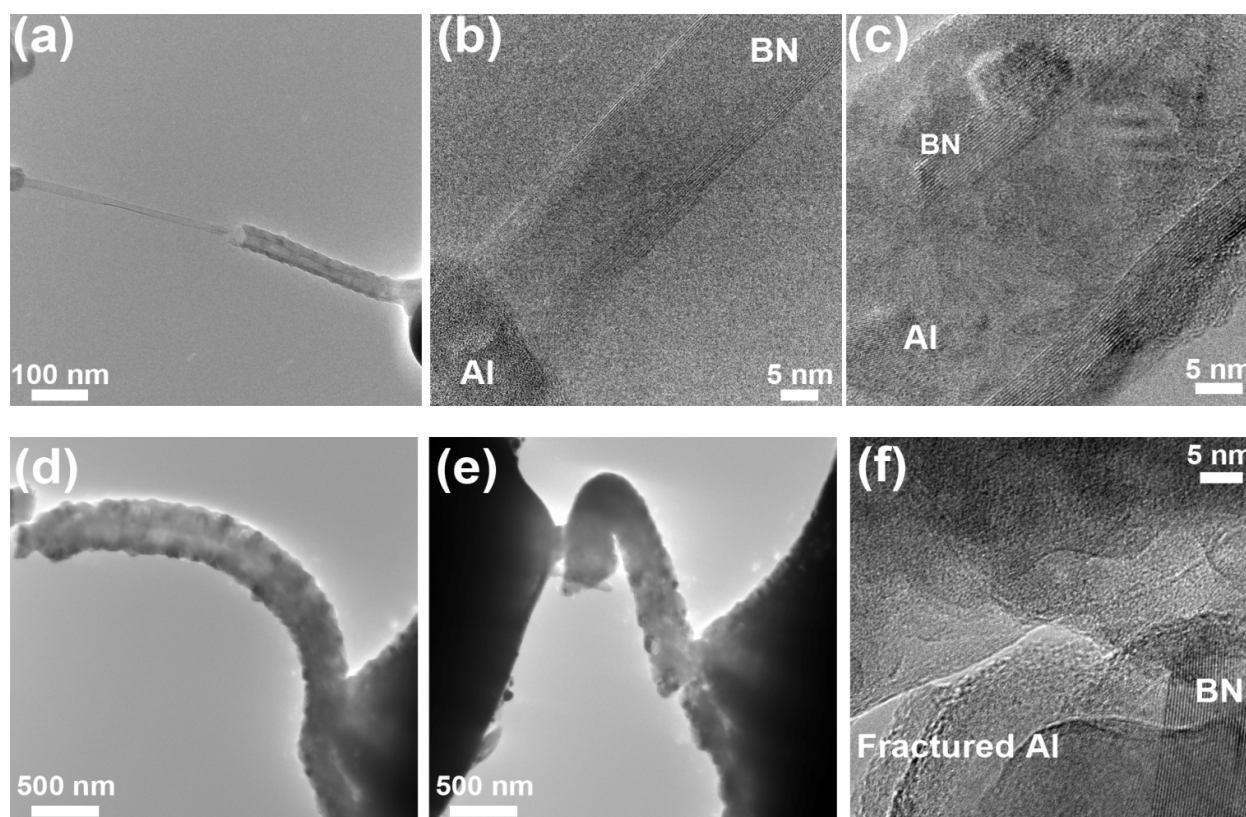emaining joint between Al coating and BNNT core on the left-hand-side of the image in (a); HRTEM image in (c) corresponds to the fractured nanocomposite right-hand end in (a); note that the remaining external BN layers within the Al shield are apparent; note that the experimentally measured ultimate tensile strength of this sample was 1.47 GPa; and (d-f): a BNNT coated with 200 nm Al broken under bending, HRTEM image corresponds to the lower broken end of the hybrid in (e).

By taking into account the accurately measured in TEM displacement difference for the initial and final stages, a total strain in Figure 2.12 was calculated to be 2.1 %. The displacement was measured by choosing two reference positions on the composite sample and measuring the distance difference between them while taking into account the TEM image changes in both vertical and horizontal directions on the imaging plane under loading. We also attempted to measure the strains by in situ measuring the changes of the SAED patterns (compared to the undeformed state) during and after the tensile tests. For example, for a BNNT with Al 20 nm coating sample the measured d spacing for (1 1 1) Al reflection was 0.245, 0.245 and 0.231 nm, before, under and after the tensile deformation, respectively (note that 0.233 nm is the standard value for the bulk Al); also the ratio of the vertical and horizontal length of electron diffraction (ED) of the Al (1 1 1) ring was 1.04, 1.05 and 1.05, correspondingly, so that the assumed elongation may be counted to be ~ 5%, which

is in the range of the standard error of electron diffraction techniques. That is the reason why we were not able to use ED data to accurately measure displacements and/or real strains.

Regretfully, at the present stage of the in situ TEM holder developments it is not possible to break and/or even provide enough stress to the thicker Al-BNNT nanocomposites (100 ~ 200 nm coatings) fabricated in the frame of this work. Indeed, the thickness of Al coatings should have an important influence on the mechanical properties and fracture behaviors of the nanohybrids. However, we still try to carefully carry out numerous tensile experiments on the samples with different Al coating thicknesses. We have accomplished the direct in situ TEM tensile tests on Al coated samples with nominal Al thicknesses of 20, 60, 100 and 300 nm, see Figure 2.4 (these correspond to the actual metal layer thicknesses of 20, 30, 40 and 200 nm, as accurately measured by HRTEM). As a result, we should admit that experimentally it was not possible to numerically compare the mechanical properties: the thicker nanohybrid samples could not be fractured or even sufficiently loaded during a tensile test due to the experimental force limit of the Nanofactory AFM holder. In fact, a previous paper from our group reported that most of the pure BNNT samples with a diameter of more than ~50 nm were not broken, and so it was difficult to obtain accurate values of the ultimate tensile strength or Young's modulus data using the present in situ AFM-TEM technique [9]. Anyway, according to the studied Al-BNNT samples which could be broken, it became clear that there is a certain difference for the fracture mechanism between thinner Al-layered and thicker Al-layered BNNT composites (Figure 2.13 (a–f)). On one hand, when an Al 20 nm-BNNT nanocomposite was completely fractured in tension, the inner portion of BNNT shells slipped out of the outer BN layers which had remained rigidly fixed to the Al shield, as shown in Figure 2.13 (a) and b. On the other hand, an Al-BNNT nanohybrid with a 200 nm Al layer, that did not fail under tension, was managed to be cracked under bending along the Al grain boundary, as shown in Figure 2.13 (d–f). The thinner sample fractured abruptly in a brittle way, while the thicker sample fracture (started within the Al grains) was stopped by the BNNT core and, providing the huge strength of BNNT multi-layers themselves, up to more than 30 GPa [10]; such nanocomposites may be expected to withhold greater forces and stresses.

It is worth noting that similarly positive and radical effects of multi-walled BNNTs on Al compressive properties have so far been noticed in a single publication dealing with these novel materials, i.e. under compression of Al-BNNT nanocomposites produced by standard powder metallurgy. In fact, a five times increase in microhardness and a three times increase in compressive strength were evidenced for Al-BNNT macrocomposites with 1.5 wt. % of BNNT fraction compared to pure aluminum [17]. These encouraging results, together with the presently carried out first ever direct bending and tensile tests of Al-BNNT composite nanohybrids, open up a wide horizon for future developments with regard to these unique "dream" structural materials of the future.

2.5   *Ab initio* atomistic computer simulations

2.5.1 Introduction

The complete understanding of the mechanical properties of Al-BNNT nanohybrids and composite materials where BNNTs are dispersed in the Al matrix is not possible without precise microscopic knowledge of the atomic structure of the interfaces between BNNTs and the Al matrix encapsulating the tubes. Although many phenomena may occur in Al-BNNTs nanohybrids under mechanical deformation, the response of the system to the external stress should depend on strength of the bonding between the matrix and the reinforcing agents. Indeed, mechanical load transfer from the matrix to nanotubes is essentially not possible if the bonding at the interface is too weak.

In this section, using first-principles (ab initio) atomistic computer simulations at the density-functional-theory (DFT) approximation, we study the bonding at the interface and estimate the critical shear stress. We consider boss the "ideal" interfaces between perfect Al (1 1 1) surface and defect-free BN sheets and also the interface between these systems when point defects are present. We demonstrated that critical shear stress at the ideal interface is very low, but introduction of defects such as vacancies and interstitial atoms may considerably improve the bonding at the interface and critical shear stress.
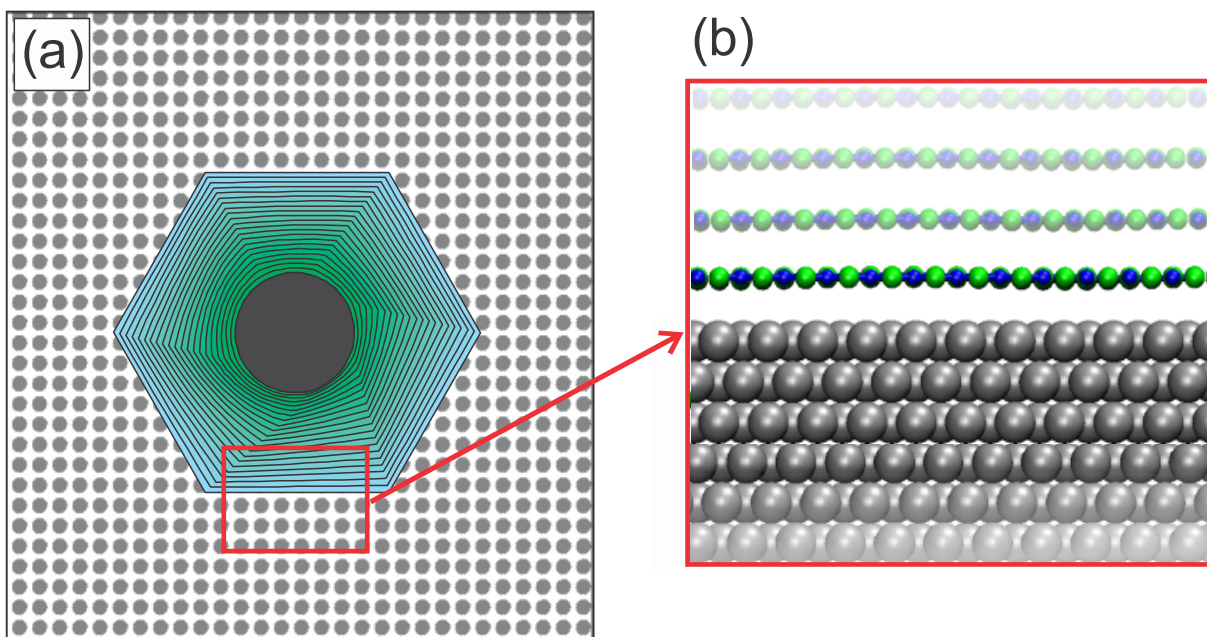

Figure 2.14 Schematic representation of a multi-walled BN nanotube embedded into Al matrix (a) and the atomistic picture of the BN-Al interface (b). Grey balls stand for aluminum atoms, blue for nitrogen, green for boron.

2.5.2 Computational approach used and the simulation setup

As the cross sections of multi-walled BNNTs with large diameters normally have shapes of polygons rather than cylinders, as schematically shown in Figure 2.14, the outer shell of the BNNT was modeled as a BN sheet.

It is well known that the (1 1 1) surface in FCC metals has the lowest energy, so that we simulated the Al matrix as a slab with the (1 1 1) surface facing the BN sheet. Certainly, other surfaces may be at the interface, but based on energy considerations, most of them should be low-index surfaces, and one can expect that their behavior should be similar to the case of (1 1 1) surface studied here. As shown below, the interaction between Al and BN is governed by very weak van der Waals (vdW) forces, so that the presence of BN should not change the energetics.

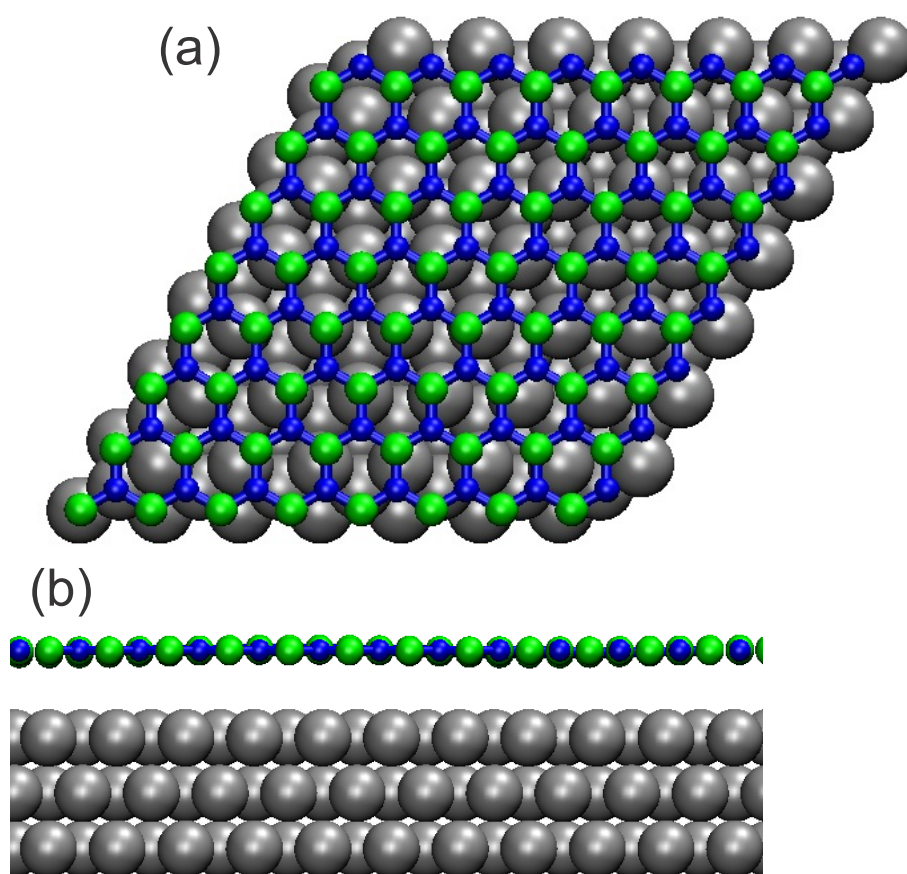**Figure 2.15** The top (a) and side (b) views of the system used in the DFT simulations. Grey balls stand for aluminum atoms, blue for nitrogen, green for boron.

Figure 2.14 (a) schematically shows a multi-walled BN nanotube embedded into Al matrix. The atomistic picture of the BN-Al interface is presented in Figure 2.14 (b). Grey balls stand for aluminum atoms, blue for nitrogen, green for boron.

The first-principles simulations were performed using DFT method as implemented in the plane-wave-basis-set Vienna ab initio simulation package [26] Projector augmented wave potentials [27] were used to describe the core electrons, and a vdW non-local functional (VV10) [28] which goes beyond the local and semilocal approximations to describe the exchange and correlation. Kinetic energy cutoff for the plane waves was set to 400 eV which was found to pride the total energies converged within 0.001 eV/atom. The same accuracy was achieved with regard to the number of k-points in the two-dimensional Brillouin zone. All the structures were relaxed until atomic forces were below 0.002 eV/Å. The VV10 functional tends to somewhat overestimate the binding [29], but it describes very well the geometry of the system. The calculations were done on CRAY supercomputer provided by the Center for Scientific Computing, Finland.

The BN-Al system used in DFT simulations is shown in Figure 2.15. The periodic boundary conditions imposed by the plane-wave approach made us to search for (nearly) commensurate BN/Al systems. This was achieved by considering 8×8 (in terms of unit cells) supercell of BN on top of 7×7 (1 1 1) surface supercell of Al. The mismatch between the sizes of the systems was less than 0.3%. The BN sheet consisted of 128 atoms, while the Al slab was composed of three closely packed planes and had 147 atoms. The atoms in the bottom plane were kept fixed during the geometry optimization.

To estimate critical shear stress σ_{max} corresponding to the minimum stress when the BN sheet starts sliding with respect to the Al matrix, we used the following simulation setup, Figure 2.16: The BN sheet was periodically shifted with regard to the Al slab with a step of 0.2 Å, and the total potential energy of the system was calculated for each position. The atoms in the BN sheet were allowed to move only in the direction perpendicular to the slab surface. The bottom layer in the Al slab was kept fixed. The energy landscape typical for such calculation is shown in Figure 2.16 (b). Point 1 corresponds to the global energy minimum of the system. The force presented in panel (c) was evaluated numerically, and σ_{max} was calculated as the maximum force over the total area. Point 2 corresponds to σ_{max}.
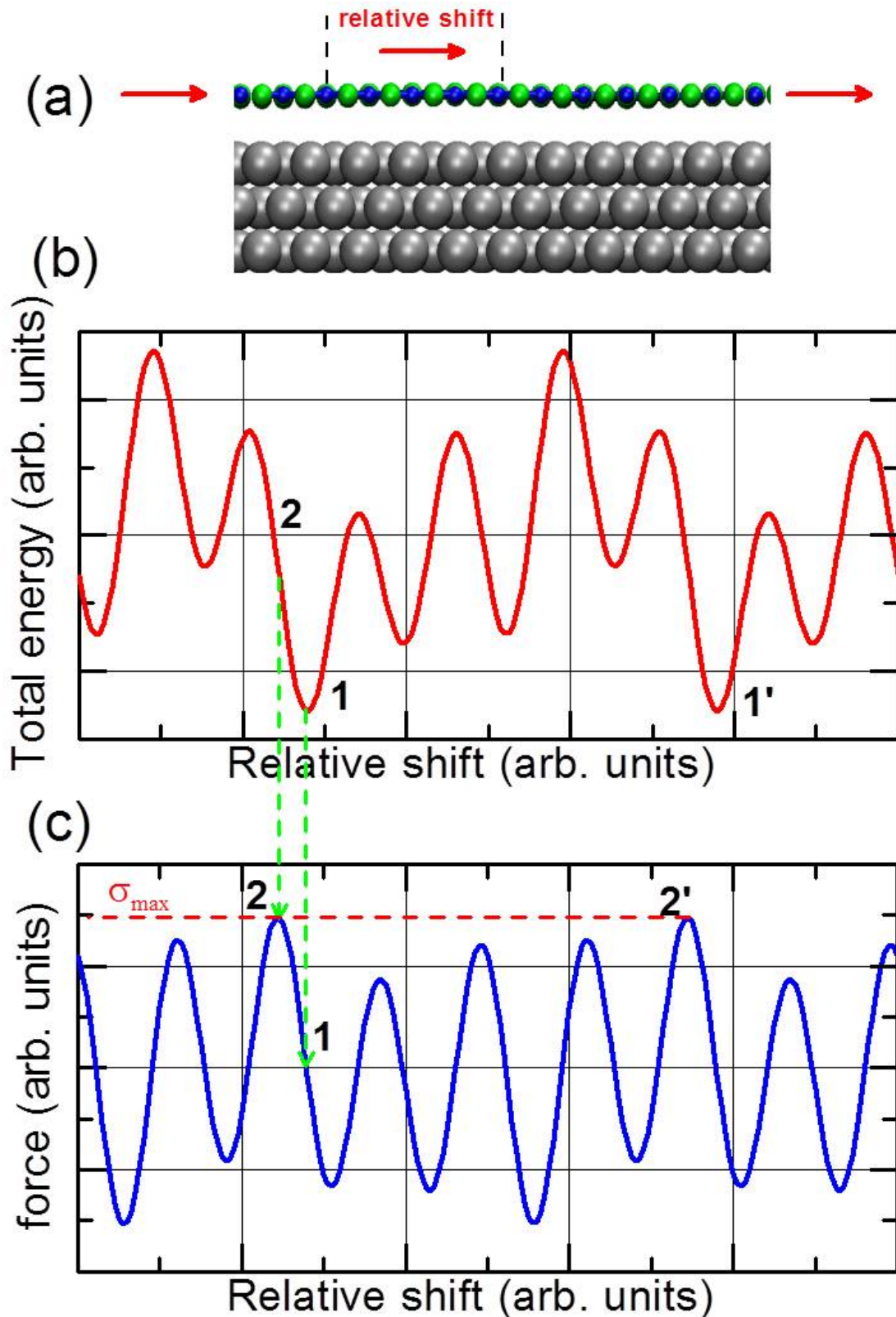
Figure 2.16 Schematic representation of the simulation setup (a). The BN sheet was periodically shifted with regard to the Al slab, and the total potential energy of the system was calculated. For each point, the atoms in the BN sheet were allowed to move only in the direction perpendicular to the slab surface. The bottom layer in the Al slab was kept fixed. (b) Energy landscape. Point 1 corresponds to the global energy minimum of the system. The force presented in panel (c) was evaluated numerically, and critical shear stress σ_{max} was calculated as the maximum force over the total area. Point 2 corresponds to σ_{max}.

2.5.3 Simulation results

2.5.3.1 The atomic structure of the interface between the ideal systems without any defects

Our simulations for the ideal systems without any defects at the interface showed that the bonding between Al and BN is indeed governed by the vdW interactions, and it is very weak. The binding energy is 21.1 me V/A², comparable to interlayer binding energy in graphite. The average separation between Al and BN was 3.6 A. The interaction between B/N and Al atoms in different areas of the simulation supercell resulted in the development of a Moiré pattern, similar to the case of graphene on metals [30]. The origin of the Moiré pattern is evident from Figure 2.17. The mismatch between atom positions in the BN sheet and Al gives rise to the development of Moiré pattern. Note that at point A the Al atoms correspond to the center of the hexagon, at point B the Al atom is exactly under nitrogen atom, while at point C the Al atom is under B atom.

Different mutual positions and thus different strengths of the local interaction between BN sheet and Al surface gives rise to the corrugation of the surface with amplitude of about 0.1 Å, as illustrated in Figure 2.18. Here the atoms in the BN sheet are colored according to their elevation.

2.5.3.2 Critical shear stress at the Al-BN interface without defects

Having studied the atomic structure at the interface, we moved on the calculations of the critical shear stress. As described above, the BN sheet was periodically shifted with regard to the Al slab with a step of 0.2 Å, and the total potential energy $E(x)$ of the system was calculated for each position. 6 different directions were studied. Forces were evaluated numerically for each position as:

$$f(x) = -dE(x)/dx \qquad (3)$$

and σ_{max} was computed as:

$$\sigma_{max} = max\{f\}/S \qquad (4)$$

, where S is the total area of the interface.

Our calculations gave a very low $\sigma_{max} \sim 5$ MPa. This value is even lower (but of the same order of magnitude) than critical shear stress in graphite (~10 MPa). As surfaces with other indices are also governed by vdW forces and are incommensurate with BN, one can expect similar values of the stresses. This indicates that bonding at the interface is determined by defects and possibly kinks in BN rather than the morphology of regular surface structures.
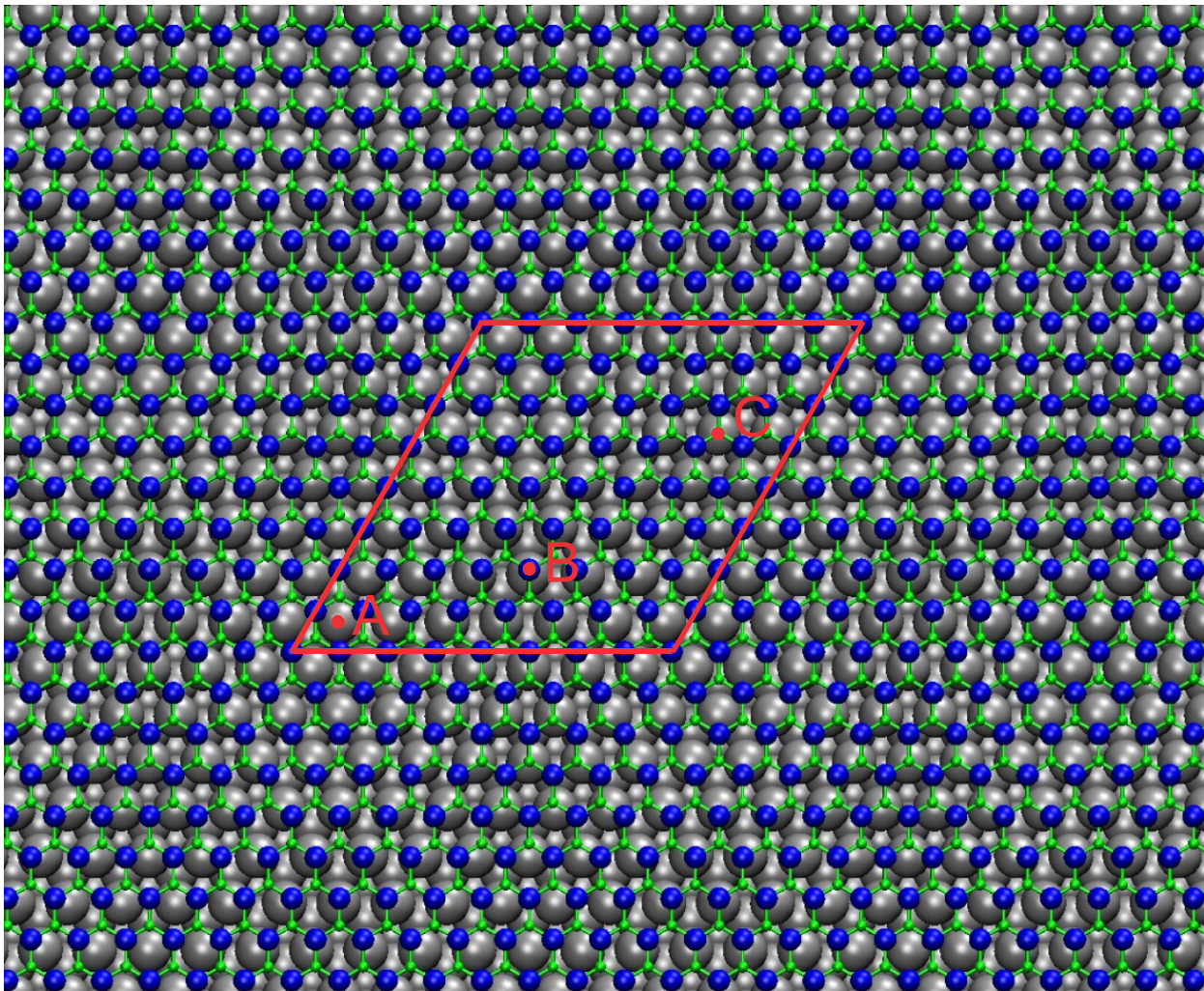
Figure 2.17 BN sheet on Al (111) surface. The simulation cell (the read diamond) is periodically extended. The mismatch between atom positions in the boron-nitride sheet and Al gives rise to the development of Moiré pattern. Note that at point A the Al atoms correspond to the center of the hexagon, at point B the Al atom is under nitrogen atom, while at point C the Al atom is under boron atom.

2.5.3.3 Critical shear stress at the Al-BN interface with defects

In order to get microscopic insight into the role of point defects, we also studied the bonding at the interface between the BN sheet with typical point defects, such as vacancies, and Al (1 1 1) surface. Figure 2.19 shows the atomic structure of the BN sheet with a missing B atom (B vacancy). Our DFT calculations demonstrated that the interaction between N atoms with dangling bonds and Al surface is so strong that the Al atom is pulled out from the surface. This gives rise to a considerable increase in the critical shear strength. It naturally depends on defect concentration, but our preliminary calculations indicate that for defect concentration of 1 defect per 4 nm^2, σ_{max} increases by more than 2 orders of magnitude as compared to the ideal interface, approaching 1 GPa. Qualitatively the same results were obtained for vacancies with an Al

atom attached to the dangling bond (vacancy plus interstitial, Figure 2.20). Currently we are working to getting the accurate numbers.
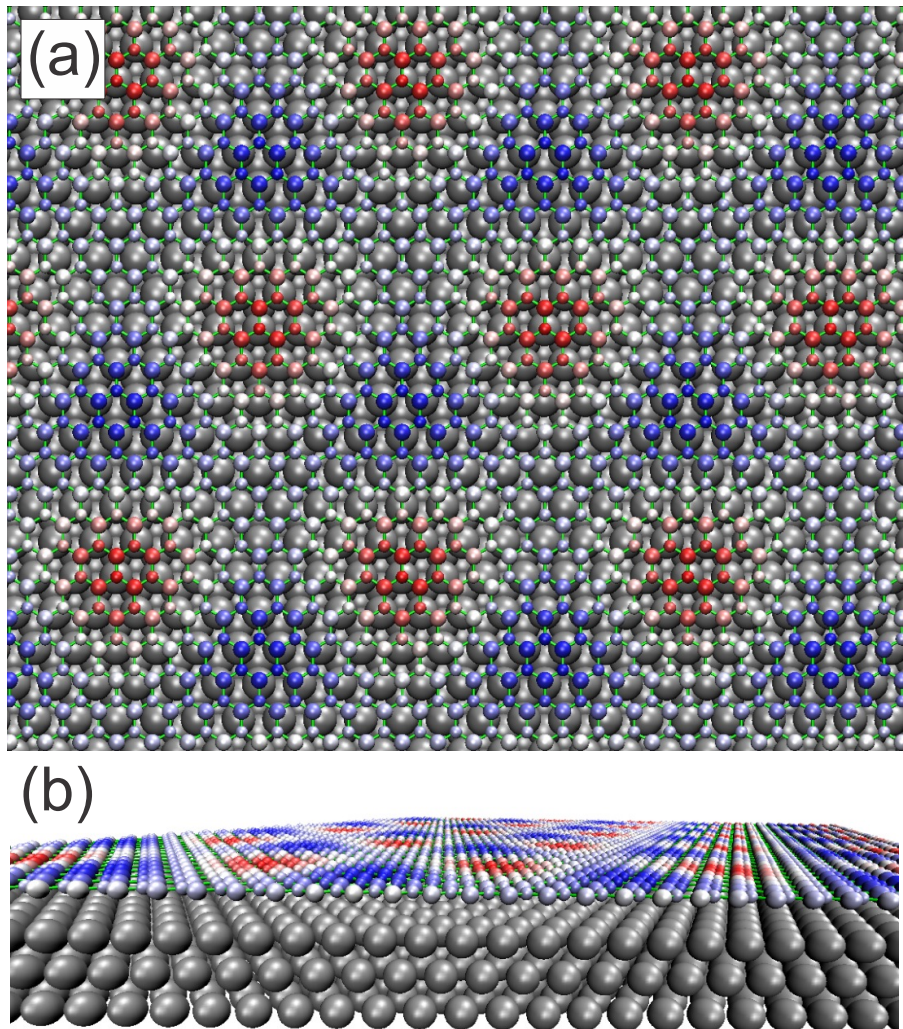
Figure 2.18 BN sheet on Al (111) surface, top view and perspective view. The atoms in the BN sheet are colored according to their elevation (the coordinate orthogonal to the surface). Red color corresponds to the 'low' areas, blue to 'high' areas.
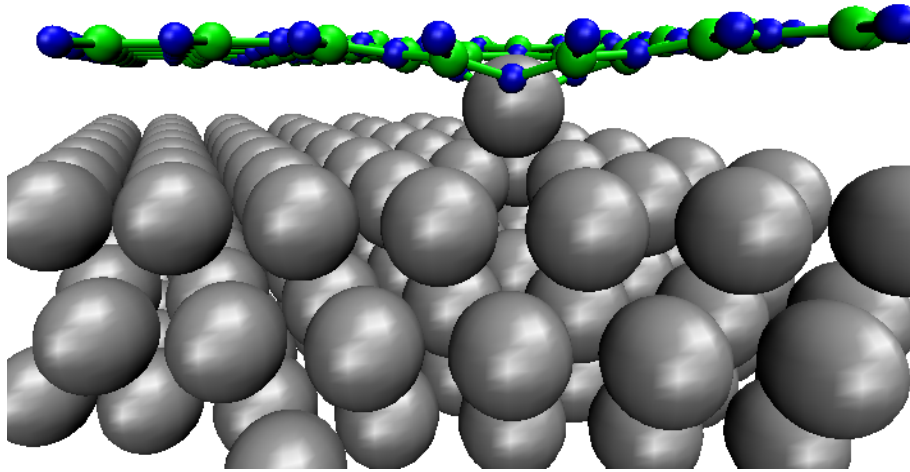
Figure 2.19 The atomic structure of a BN sheet on Al (111) surface with a B vacancy. The interaction between N atoms with dangling bonds and Al surface is so strong that the Al atom is pulled out from the surface.
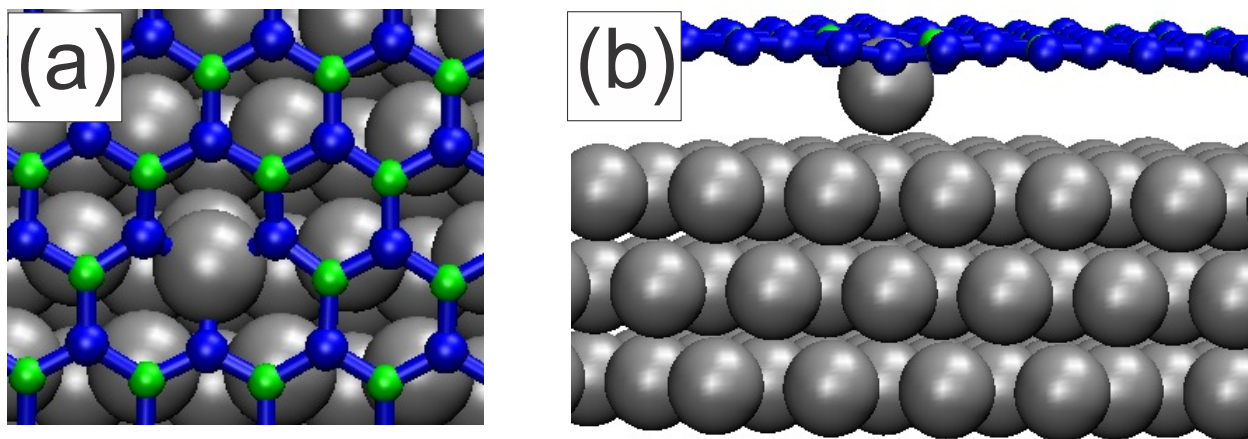
Figure 2.20 The atomic structure of a BN sheet on Al (111) surface with a B vacancy and Al interstitial atom.

2.6   Summary

We fabricated Al-BNNT composite nanohybrids with a varying Al coating thickness, from 5 nm to 200 nm, by magnetron sputtering. XRD, SEM, TEM, XPS and in situ TEM bending and tensile tests on individual nanohybrids shed a new light on their morphologies and atomic structures, chemical status and mechanical properties. We demonstrated that the applied synthetic route is an effective method for fabricating novel ultralight, superstrong individual Al-BNNT hybrid nanomaterials. Nanocrystalline Al coatings were documented on Al-wrapped BNNTs. The fabricated nanohybrids with suitably thick (~ 40 nm) Al coatings on BN nanotubes (of ~ 40–50 nm external diameter) demonstrated at least ~ 9 times increase in tensile stress which they can withstand without failure, compared to a pure non-armed Al metal.

We also simulated the effects of chemical bonding and regarded energies at the Al and BN intefaces by *ab initio* simulations. These indicate that the bonding between ideal Al and BN surfaces is weak and governed by van der Waals interactions. Critical shear stress is low, comparable to that of graphite. Point defects at the interface can give rise to a very big increase in critical shear stress, depending on defect concentration. Overall, the bonding in real Al-BN system is likely governed by defects rather than surface morphology.

2.7   References

[1] L. Ci, Z. Ryu, N.Y.J. Phillipp, M. Rühle. *Acta Mater.* **2006**, 54, 5367.

[2] Y. Zhang, Q. Zhang, Y. Li, N. Wang, J. Zhu. *Solid State Commun.* **2000**, 115, 51.

[3] S.M. Tripathi, T.S. Bholanath. *J Adv. Sci. Technol.* **2010**, 16, 31.

[4] X. Chen, J. Xia, J. Peng, W. Li, S. Xie. *Comp Sci Technol.* **2000**, 60, 301.

[5] Y. Zhang, N.W. Franklin, R.J. Chen, H. Dai. *Chem. Phys. Lett.* **2000**, 331, 35.

[6] Y. Zhang, H. Dai. *Appl. Phys. Lett.* **2000**, 77, 3015.

[7] W. Huang, H. Chen, J.M Zuo. *small*. **2006**, 2, 1418.

[8] W.X. Chen, J.P. Tu, L.Y. Wang, H.Y. Gan, Z.D. Xu, X.B. Zhang. *Carbon.* **2003**, 41, 215.

[9] D. Golberg, P.M.F.J. Costa, O. Lourie, M. Mitome, X.D. Bai, K. Kurashima, C.Y. Zhi, C.C. Tang, Y. Bando. *Nano Lett.* **2007**, 7, 2146.

[10] X.L. Wei, M.S. Wang, Y. Bando, D. Golberg . *Adv. Mater.* **2010**, 22, 4895.

[11] M.S. Wang, D. Golberg, Y. Bando. *Adv. Mater.* **2010**, 22, 93.

[12] D.M. Tang, C.L. Ren, X.L. Wei, M.S. Wang, C. Liu, Y. Bando, D. Golberg. *ACS Nano* **2011**, 5, 7362.

[13] D. Golberg, P.M.F.J. Costa, M.S. Wang, X. Wei, D.M. Tang, Z. Xu, Y. Huang, U.K. Gautam, B. Liu, H. Zeng, N. Kawamoto, C. Y. Zhi, M. Mitome, Y. Bando. *Adv. Mater.* **2012**, 24, 177.

[14] Y. Li, P. Liu, X. Wang, H. Jin, J. Yang, G. Qiao. *Scripta Mater.* **2010**, 63, 185.

[15] M. Du, J.Q. Bi, W.L. Wang, X.L. Sun, N.N. Long, Y.J. Bai. *Mater. Sci. Eng. A.* **2011**, 530, 669.

[16] Z.G. Chen, J. Zou, Q. Liu, C. Sun, G. Liu, X. Yao, F. Li, T. Sekiguchi, H.M. Cheng, G.Q. Lu. *ACS Nano.* **2008**, 2, 1523.

[17] S.K. Singhal, A.K. Srivastava, R. Pasricha, R.B. Mathur. *J. Nanosci. Nanotechnol.* **2011**, 11, 5179.

[18] R.B. Patel, J. Eng, Z. Iqbal. *J. Mater. Res.* **2011**, 26, 1332.

[19] H. Kwon, C.R. Bradbury, M. Leparoux. *Adv. Eng. Mater.* **2011**, 13, 325.

[20] S.R. Bakshi, D. Lahiri, A. Agarwal. *Int. Mater. Rev.* **2010**, 55, 41.

[21] D. Golberg, Y. Bando, C.C. Tang, C.Y. Zhi. *Adv. Mater.* **2007**, 19, 2413.

[22] H. Chen, H. Zhang, L. Fu, Y. Chen, J.S. Williams, C. Yu, D. Yu. *Appl. Phys. Lett.* **2008**, 92, 243105.

[23] E.A. Obrastsova, D.V. Shtansky, A.N. Sheveiko, A.M. Kovalsky, M. Yamaguchi, D. Golberg. *Scripta Mater.* **2012**, 67, 507.

[24] E.A. Obrastsova, D.V. Shtansky, A.N. Sheveiko, M. Yamaguchi, A.M. Kovalskii, J.Y. Mevellec, S. Lefrantm, D. Golberg. *J. Nanoelectro. Optoelectro.* **2013**, 8, 87.

[25] M.S. Wang, I. Kaplan-Ashiri, X.L. Wei, R. Rosentsveig, H.D. Wagner, R. Tenne, L. M. Peng. *Nano Res.* **2008**, 1, 22.

[26] G. Kresse, G, J. Furthmuller. *Phys. Rev. B.* **1996**, 54, 11169.

[27] P.E. Blochl. *Phys. Rev. B.* **1994**, 50, 17953.

[28] O.A. Vydrov, T. Van Voorhis. *J. Chem. Phys.* **2010**, 133, 244103.

[29] T. Björkman, A. Gulans, A. Krasheninnikov, R.M. Nieminen. *Phys. Rev. Lett.* **2012**, 108, 235502.

[30] J. Wintterlin, M.L. Bocquet. *Surface Science*. **2009**, 603, 1841

Chapter 3

Microcomposites

3. Microcomposites

Chapter 3 Microcomposites

3.1   Introduction

For testing novel aircraft materials, an Al matrix has been the most popular one for making MMC using CNTs. Since I have studied Al-BNNT nanoscale structures and mechanical properties, as shown in chapter 2, and demonstrated their high potentials for MMC, now, the next logic-driven step would be a try to design and fabricate lightweight BNNT-containing composites with meaningful dimensions (e.g., dozens of centimeter ranges) in which BNNTs are somehow distributed in a real crystalline Al matrix.

Melting and solidification processing is one of the most conventional techniques for producing MMC that has also been utilized for fabricating nanotube-reinforced composites. However, there have been only a few studies available for MMC-CNT composites using low melting point metals. Due to a requirement of rather high temperature for melting any metal, the process may cause damage to CNTs or initiation of chemical reactions leading to the formation of Al_4C_3 phases at the CNT/metal interface [1]. Another limitation is that suspended CNTs tend to form clusters due to surface tension forces [1]. Melting-driven techniques include melt-spinning [2], casting [3-5], metal infiltration [6] and laser deposition [7]. The rapid solidification (RS) technique allows the extension of alloying levels and more refined microstructures, which can lead to enhanced mechanical and physical properties. In addition, RS processing may help nanotubes to survive the melting process because of flash and controllable melting required for this technique. As the initial step toward this goal, I report the first time utilization of a melt-spinning technique to prepare BNNT-loaded lightweight Al composite ribbons and studies on their structure, Al/BN interfaces and mechanical properties. Also in this study the objective was to find the origin of Al/BN phases interactions and energy dissipations inside the fabricated composites over a wide temperature range.

3.2 Experimental conditions

Multi-walled BNNTs were synthesized at a high yield (approximately 1.0 g per single experimental run) through the so-called boron oxide-assisted CVD (BOCVD) method, as was reported in our previous chapters. After subsequent high-temperature purification in argon atmosphere, the nanotubes were dispersed in ethanol. Al-BNNT composite ribbons were prepared using melt spinning (a machine by Nisshin Giken Corp., Japan) in argon atmosphere. Figure 3.1 shows a sketch of the fabrication procedure. To disperse BNNTs well within an Al powder, the tubes were kept in ethanol during their mixing with the powder (50 to 150 μm, purity 99.5 %). It was a very important step as some tube clustering may occur under powder mixing and further formed Al-BNNT pellets cannot be electrically conductive (BNNT fraction is an electrical insulator). This would prevent their further melting under induction heating. The Al powder and dispersed BNNTs were mixed by a mechanical mixer; approximately 0.5 g of the mixed material was put in a die and pressed at a pressure of approximately 20 MPa at room temperature, and numerous starting Al-BNNT pellets were fabricated. About 2.0 to 2.5 g of the prepared Al-BNNT pellets were used for a single experimental run. They were pre-placed in a quartz tube, which had a nozzle diameter of 1 mm, melted by the induction currents, and melt-spun on a rotating water-cooled copper drum at a wheel rotation speed of 24 ms^{-1}. The
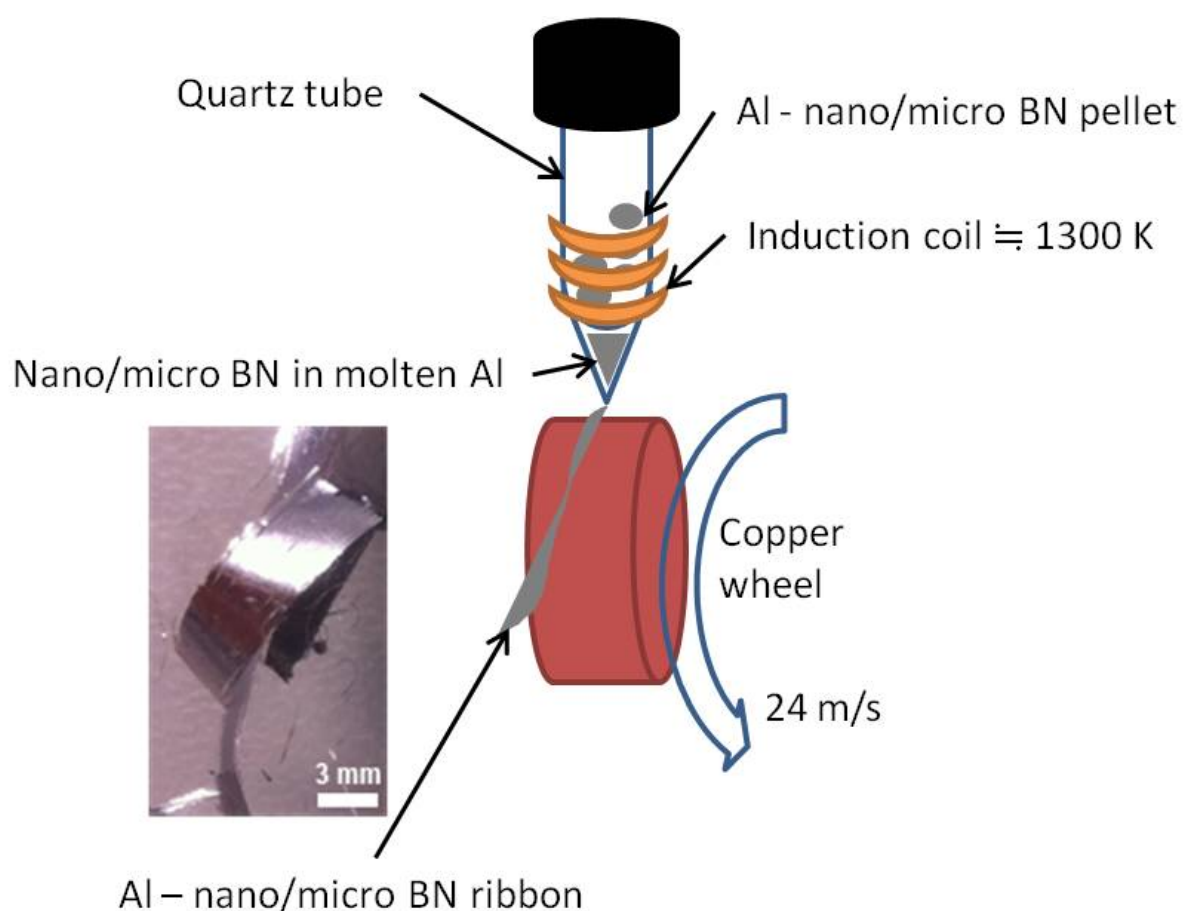

Figure 3.1 Fabrication procedure of Al-BNNT composite ribbons.

fabricated melt-spun ribbons were approximately 50 μm in thickness and 4 to 5 mm in width. The length of the ribbons varied and was dependent on the stability of casting. As a rule, the fragments up to 1 m long could be obtained. The phase compositions and crystal structures of the prepared composites were analyzed by X-ray diffraction (XRD; RINT2000 Ultima III, Rigaku Corporation, Japan) using Cu Kα1 radiation. The morphologies and micro and atomic structures of the composite ribbons were studied by scanning electron microscopy (SEM; S4800, Hitachi Ltd., Japan) and high-resolution transmission electron microscopy (TEM; JEM-2100F (200 kV), JEM-3000F (300 kV) and JEM-3100FEF (Omega filter) instruments, JEOL Ltd., Japan). TEM samples were prepared by using focused ion beam (FIB) polishing. Energy dispersive X-ray spectrometry under SEM and TEM investigations (EMAX EX-220, Horiba Ltd., Kyoto, Japan; JEM-3100FEF microscopes) at accelerating voltages of 10 kV (SEM) and 300 kV (TEM), respectively, were employed to identify the composite chemistry and to spatially map the constituting species. Tensile tests were carried out at room temperature on a "Shimadzu" testing machine (AG-plus 10kN, SHIMADZU, Japan) at a deformation rate of $1.67 \times 10^{-4} s^{-1}$.

3.3 Mechanical properties analysis and structural characterization of Al-BNNTs ribbons

Representative room temperature stress-strain curves of pure melt-spun Al ribbons and those with various BNNT loading fractions are shown in Figure 3.2. The maximum measured strengths of ribbons are 60 MPa (Al), 75 MPa (Al-BNNT 0.5 wt%), 115 MPa (Al-BNNT 1.0 wt%), and 145 MPa (Al-BNNT 3.0 wt%). The curves for Al and Al-BNNT 0.5 wt% ribbons look nearly similar, meaning that at such low BNNT loading fractions, the tensile properties still cannot be modified. However, with increasing BNNT content, the tensile strength and the slope of the curves (and thus the Young's modulus) dramatically change. For example, the ultimate tensile strength and the Young's modulus more than doubled in the sample with 3.0 wt% BNNTs. It would be interesting to compare the obtained tensile strength data with the previously reported results for Al-CNT composites. For example, Kuzumaki et al. [8] measured these values for pure Al samples and for those with 2.5 and 5.0 wt% of CNT loadings, before and after annealing the samples over 50 and 100 hours at 873 K. The tensile strength values of 90 MPa for untreated Al samples, and 45 MPa and 40 MPa for these after consecutive annealing, and unchanged values of 80 MPa (either before or after heat treatments) for the samples with CNTs were reported. Salas et al. [9] documented only 20 MPa strength for Al samples with 5.0 wt% of CNTs. Therefore, the figures obtained in our work markedly prevail over literature data for Al-CNT composites at approximately the same or even lower loading fractions of reinforcing BNNTs. Figure 3.3 (a) shows a SEM image taken from a starting Al-BNNT 3.0 wt% pellet before melt casting. Individual (not bundled) BNNTs are seen randomly distributed within the pellet (as arrowed). The typical tube length reaches approximately 5 μm. Figure 3.3 (b) depicts a SEM image of the same sample after melt casting and FIB treatment. The BNNT network is clearly seen at the edge of the Al matrix. Many nanotubes protrude out of the polished Al phase, creating a sort of internal microframe. The
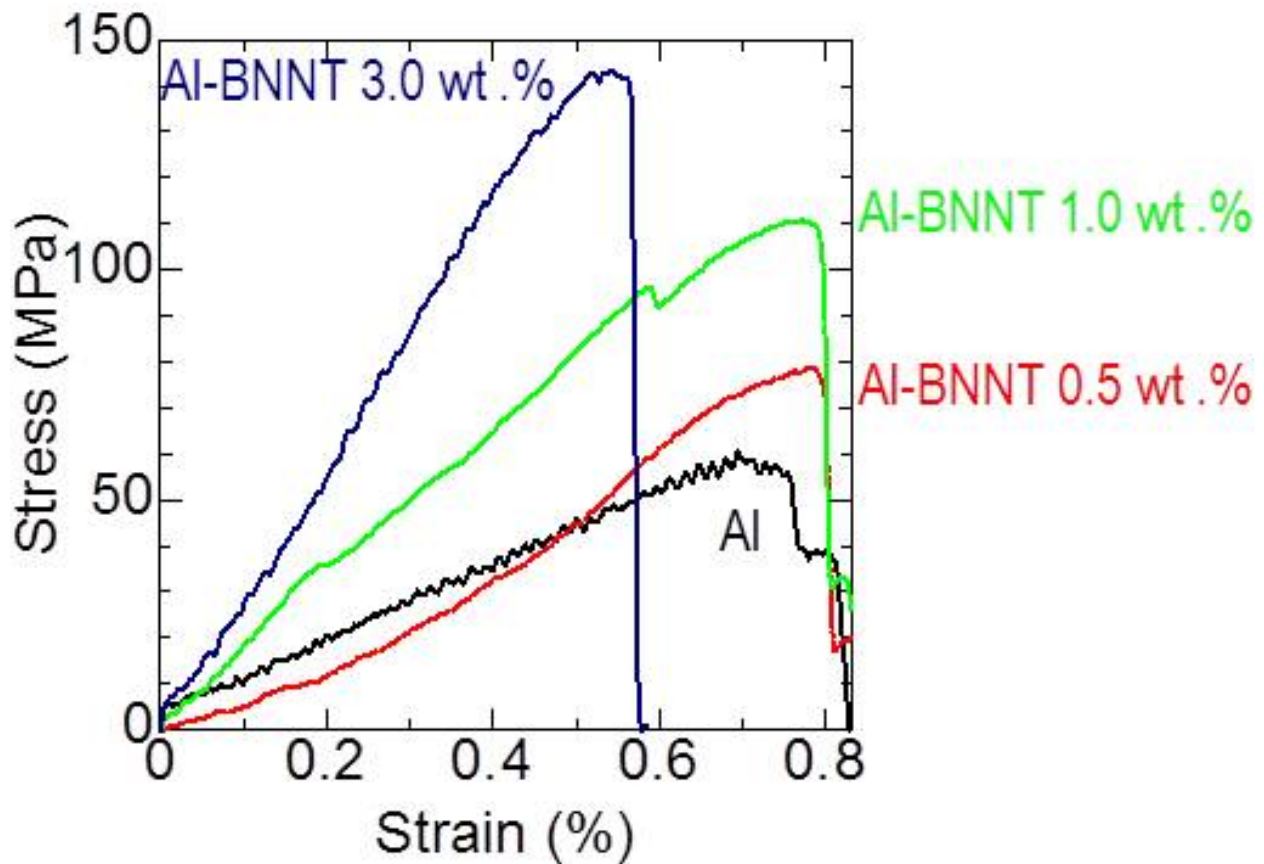
Figure 3.2 Stress-strain curves of pure Al and composite Al-BNNT melt-spun ribbons under tension at room temperature.

inset to this figure displays an optical image of the same ribbon after polishing and chemical etching of its surface. Most of the Al grains after melt spinning are very fine, around only 2 to 3 μm in size. Figure 3.3 (c) and (d) show SEM images of the fractured surfaces of an Al-BNNT 3.0 wt% ribbon after the tensile test. Some BNNTs embedded in the Al matrix are seen at that surface (arrowed), which is an indication of their contribution to carrying a tensile load. The ribbon casting rate can hardly be controlled using the present experimental setup. It is determined by the specific melting conditions inside the inductor of the melt-spinning equipment, which sometimes may vary. Perfect texturing / orientation of BNNTs within the melt-spun ribbons are difficult to achieve, and the tubes are mostly randomly oriented within the ribbons, having only a sort of quasi-alignment along the casting direction. Viscosity of the melt can be controlled by its overheating; this may result in better nanotube orientation under casting, but the overheating can lead to the negative phenomenon of BNNTs floating to the upper molten zone and inhomogeneous tube distribution in the ribbons after casting.
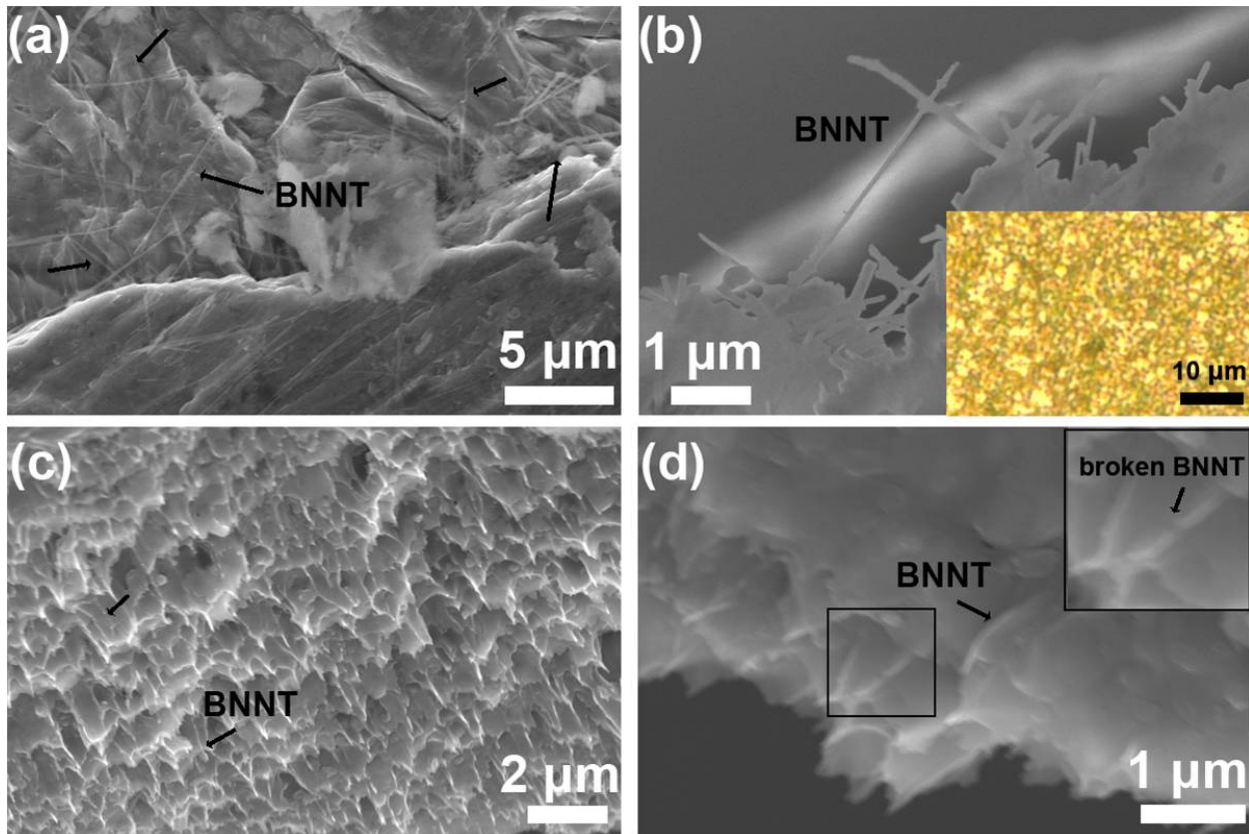
Figure 3.3 Structural characterization of Al-BNNTs ribbons. (a) SEM image of Al-BNNT (3wt%) composite pellet before melt casting. (b) A morphology formed in the melt cast ribbon; the inset is an optical image of the cast of ribbon after polishing and etching. This reveals an approximately 1.5 to 3 μm Al grain size. (c and d) Representative fracture surfaces of the tensile tested sample (3wt%) at various magnifications; individual BNNTs are seen at those surfaces (arrowed); thus they, at least partially, carry the applied tensile load and participated in the deformation process. A framed area shows a tube presumably broken into two halves under tension; this area is specially enlarged in the upper right inset.

Figure 3.4 shows low- and high-resolution TEM images, EDS, and XRD analyses of the obtained Al-BNNT 3.0 wt% composite ribbons close to the fracture surfaces after the tensile tests. The EDS spectrum at the inset of Figure 3.4 (a) confirms the pure Al composition of the matrix after melt casting - a weak B peak is coming out of the dispersed nanotubes, Cr and Mo peaks are due to the TEM holder, and minor Si and O signals are possibly originated from the traces of the quartz in the melt-spun samples. The clean Al micrograins and their triple boundaries are seen at a high magnification (Figure 3.4 (b)); importantly, no other phases like Al borides or nitrides form in the Al matrix according to a detailed X-ray analysis on numerous samples (the central inset to Figure 3.4 (b) depicts a representative X-ray spectrum). The atomically resolved TEM image in Figure 3.4 (c) displays a microcrystalline Al grain viewed along the [1 1 0] zone axis. The traces of remaining BNNTs embedded into the Al matrix are also apparent (Figure 3.4 (d-f)). The nanotubes may be located inside the grains (Figure 3.4 (d and e)) or be somehow assembled along the grain boundaries (Figure 3.4 (f)).

3. Microcomposites

The above-presented microscopic analysis revealed several important features of the nanotube-containing melt-spun material and its deformation process: (1) the multiwalled BNNTs are randomly distributed in the melt-spun ribbons; (2) no other phases except pure Al and well-preserved BNNTs are present in them; (3) BNNT cohesion strength with the metal is high enough and allows them not to be pulled out from the metal during tension; (4) the nanotubes, at least partially, carry the tensile load, as evidenced by their microscopic images for which the tube axes are somehow aligned along the deformation axis (for instance, Figure 3.4 (c and d), and sometimes the nanotubes are seen broken in pieces (the framed area and the corresponding inset) close to the fracture surface (Figure 3.3 (d). It is known that nanophase precipitates can serve as pinning sites for the dislocation movement, thus leading to the Al matrix hardening. This mechanism has widely been accepted, and most likely, it is applicable here. In fact, the BNNTs distributed within or along the grain boundaries (Figure 3.4 (d-f)) may hinder the dislocation glide and lead to the restriction of a plastic flow and matrix strengthening. Additionally, the particular appearance of nanotubes,
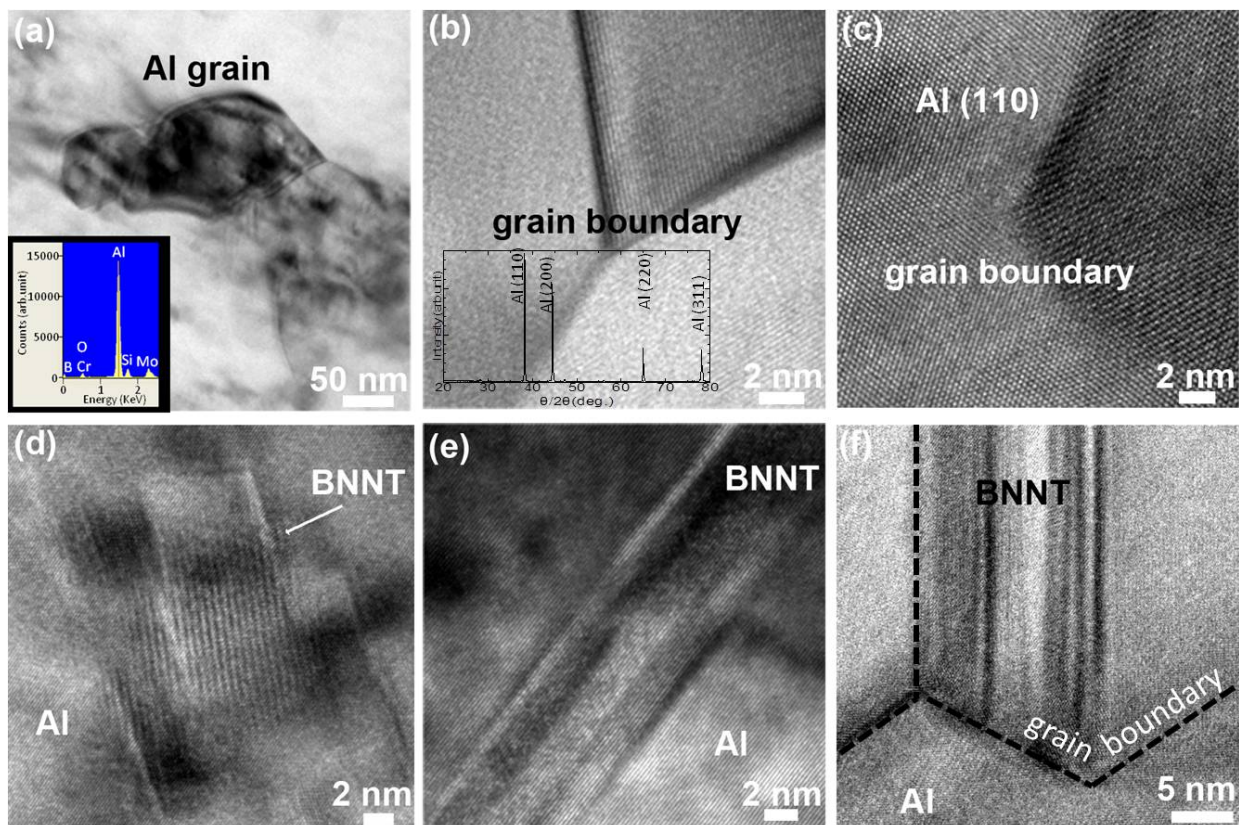
Figure 3.4 TEM image of an Al-BNNT 3wt% composite ribbon near the fractured surface after a tensile test. (a) The smallest Al grains found in the melt-spun Al-BNNT matrix; the inset depicts an EDS pattern record from this area. (b and c) A triple grain boundary in the Al-BNNT matrix at various magnifications; the central inset in (b) shows a representative X-ray spectrum confirming no other phases formed in the matrix except Al; the (110), (200), (220) and (311) Al peaks are marked, (c) in the case, the Al matrix is nicely oriented along the [110] zone axis of the fcc Al lattice. (d to f) A fading contrast peculiar of images relevant to individual multi-walled BNNTs present in the fractured ribbons either within the rains (d and e) or along the grain boundaries (f).

which are seen being broken at the fractured surfaces (Figure 4d), tells us that a load transfer from the Al matrix to the reinforcing nanotubular agents has indeed taken place under room-temperature tension. The tensile strength of the reinforcing BNNTs is much higher compared to that of the pristine Al matrix (approximately 30 GPa [10, 11] and 40 to 80 MPa, respectively); therefore, the former may effectively work during tension, if the nanotube orientation happens to be along the loading axis. More work is clearly needed to perfectly align the BNNTs and/or to texture them inside the Al matrix, and to check the deformation kinetics at the intermediate (100 °C to 300 °C) and high (400 °C to 600 °C) deformation temperatures. The effects of the Al grain growth and the influence of embedded BNNTs on this process should also be evaluated with respect to the mechanical properties at temperatures higher than the room temperature.

Figure 3.5 reveals HRTEM images of the Al-BNNT 3.0 wt% ribbons, which displayed the highest degree of the reinforcement, deformed in tension at room temperature. Numerous edge dislocation cores were found to exist close to the fractured edges of the samples, as framed in Figure 3.5 (a). The distinguishing feature of the samples with BNNTs was the structural evidences of the tube participation in carrying the tensile load. For instance, the image in Figure 3.5 (b) displays two parts of an individual nanotube found within the Al matrix close to its fractured edge. The inner tube part (marked as 1) was telescopically pulled out of the external tubular layers (marked as 2) during tension. Another example of the decent tube loading under the deformation is illustrated in Figure 3.5 (c). In this case the regarded nanotube was found being protruded from the broken ribbon edge. The nanotube is seen to be fractured onto two parts along its axis direction evidencing that the structure was indeed severely loaded during a tensile test.

The room temperature Young's modulus determined from the slope of the curves in Figure 3.2 was increased under BNNT loading from approximately 15 GPa (for pure Al ribbons) to approximately 35 GPa (for the ribbons having 3.0 wt% of BNNTs). It is noted that the determined Al ribbon's Young's modulus is several times lower compared to the literature data for the bulk Al. This may be caused by a microcrystalline nature of the samples and/or some morphological peculiarities of the presently cast ribbons, for instance, porosity. Therefore, the Young's modulus of the present samples may only be compared qualitatively from sample to sample, rather than with other Al materials; taking this into account, one may document more than a two-time increase from pure Al to a composite ribbon with 3.0 wt% of BNNTs. The obtained composite tensile strength values (maximum of 145 MPa) are much higher compared to pure Al (60 MPa). The analogous dramatic effects of multiwalled BNNTs on Al mechanical properties (under compression) were reported by Singhal et al. [12] who had used a powder metallurgy route and checked the microhardness and a compressive strength of the samples loaded with 1.5 wt% BNNTs. These values were correspondingly increased five and three times compared to pure Al samples prepared under the same technology. It is worth noting that the present strength data for melt-spun Al-BNNT composite ribbons are comparable or somewhat lower than those for the cast or wrought Al alloys, for example, 483 MPa and 248 MPa for conventional 2014-T6 and 6063-T6 materials, and thus are still far from the satisfaction of engineers. But we believe that there is still a large room for improvement. The potential of BNNT strengthening has not been fully realized as yet due to several technological obstacles. The foreseen ways of the further Al-BNNT composite

enhancement are proposed by us as follows: (1) increasing the BNNT loading fraction and the tube texturing / alignment in a given matrix, (2) functionalization and / or perforation of the external BNNT surfaces to increase their cohesion with the Al matrix, (3) pre-heat treatment of the ribbons before the tensile tests directed to the second phase precipitation at the Al-BNNT interfaces and increasing the efficiency of a load transfer via chemical bonding at the nanotube-metal interfaces, and (4) trying advanced powder metallurgy routes, i.e., spark-plasma sintering, to fabricate ultimately denser and larger BNNT-containing lightweight Al-based composites. Finally, it could be mentioned that combination of BNNTs and BN nanosheets [13] as a reinforcing phase in Al-based composites may also be an interesting direction. Such complex hybrids may possess an enhanced efficiency of the load transfer from a weak Al matrix to the strong and resilient nano-BN phases. These are the topics of our ongoing research.
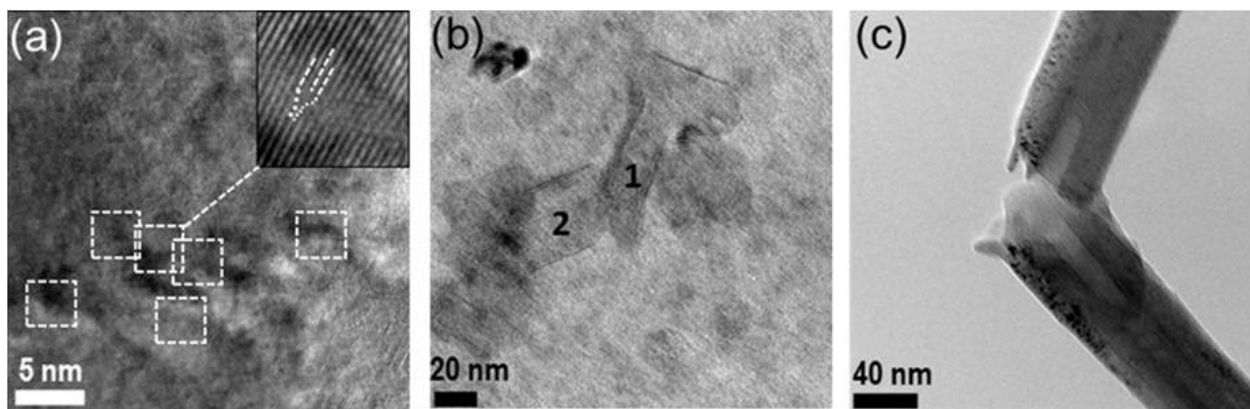

Figure 3.5 HRTEM images showing deformed structures of the Al-BNNT 1 wt% melt-spun ribbons after the tensile tests at room temperature. (a) Numerous edge dislocations cores (framed) found close to the fractured sample surfaces; the inset presents the enlarged view of a selected core. (b) A telescopically pulled-out BNNT segment observed within a deformed Al-matrix; the inner and outer nanotube portions are marked with number 1 and 2, respectively. (c) An individual cracked nanotube protruding from the deformed Al-matrix surface

3.4   Internal friction

3.4.1 Experimental conditions

In this section, I report utilization internal friction analysis by using a particularly sensitive experimental technique, to find the origin o two-phases interactions and energy dissipations inside the fabricated composites over a wide temperature range. Here besides the Al-BNNTs microribbons, Al-BN microparticle (BNMP) composites were prepared by using commercial powder (Wako Pure Chemical Industries Ltd.) to trace the comparative effects of BNMPs and our home-made BNNTs. Sample list is shown in Table 3.1.

Internal friction was measured in a high-vacuum vibrating-reed apparatus with a single-electrode capacitive excitation- detection system (see e.g. [14, 15] and Figure 3.6 for more details). Small samples (up

to 10 × 2 mm^2) were cut from the melt-spun ribbons, clamped at one end, and electrostatically subjected to flexural vibrations in the fundamental resonance mode (frequency ~ 350-1200 Hz). By heating at a rate of 2 K min^{-1}, the loss factor (internal friction) Q^{-1}, from the logarithmic decrement:

$$\delta = \pi Q^{-1} \qquad (1)$$

of freely decaying vibrations, and the resonance frequency f (reflecting the relative changes of Young's modulus $E \propto f^2$) of these vibrations were measured as a function of temperature between about 80 and 800 K. At least two consecutive measurements were made on each sample, in order to see the effect of thermal treatment from the previous measurement. The strain amplitude is not specified but generally low (of the order 10^{-6}), and variable by about 1 to 2 orders of magnitude. As some amplitude variation may result from thermally induced changes of the sample-electrode distance, the setup is ideal for measuring amplitude-independent damping; however, any amplitude dependence is usually seen during regularly necessary readjustments of the electrode position.

Table 3.1 Sample list for internal friction measurement.

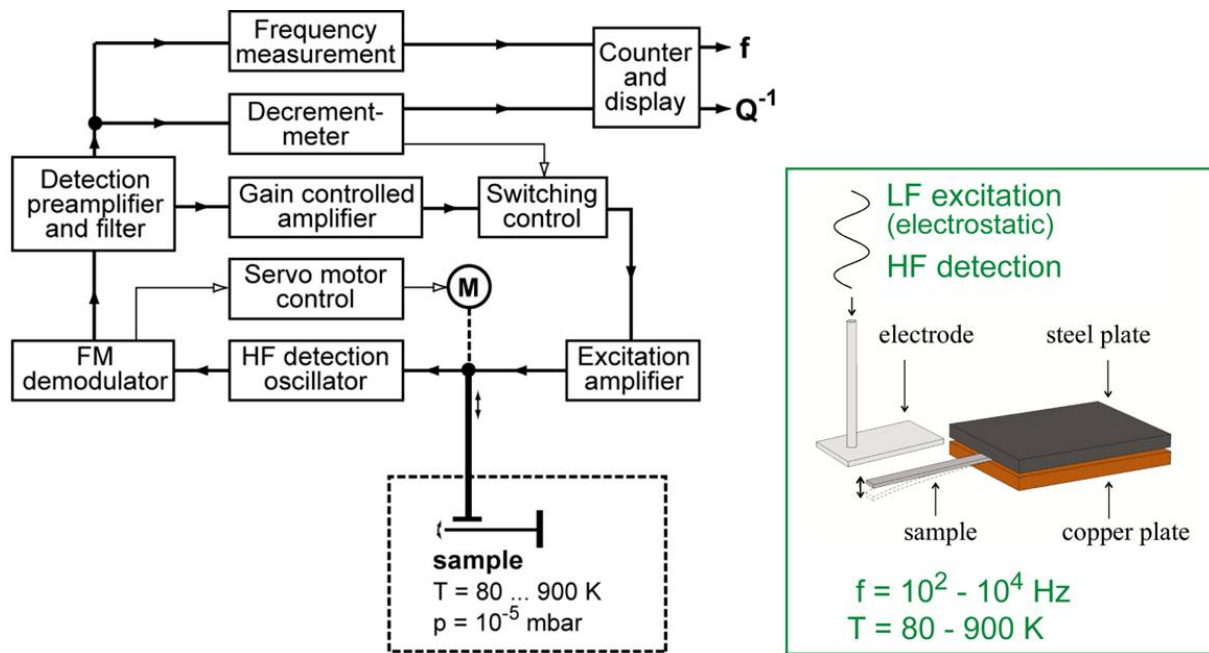| Sample No	Melt-spun ribbons	Nano-BN fraction	Notation
1	Pure Al		Al
2	Al-BN microparticles	1wt.%	BNMP1
3	Al-BN nanotubes	1 wt.%	BNNT1
4	Al-BN microparticles	5 wt.%	BNMP5
5	Al-BN nanotubes	3 wt.%	BNNT3

Figure 3.6 Operating principle of the vibrating-reed technique with single-electrode excitation-detection system (detection with frequency-modulated 40 MHz HF signal): simplified block diagram (left), and scheme of sample clamping (right).

3.4.2 Results and discussions

As an example, Figure 3.7 shows two typical heating sequences of mechanical spectra of melt-spun ribbons made of pure Al and of an Al-5.0 wt% BNMP composite (we named "BNMP5" in the graphs), respectively. Included are both the mechanical loss factor Q^{-1} (on a logarithmic scale because of the large variation, up to three orders of magnitude, over the temperature range considered), and the resonance frequency f. The latter, mainly reflecting the temperature dependence of Young's modulus, exhibits opposite annealing characteristics in both cases: a softening in pure Al, but stiffening in the composite. However, in view of different undefined factors influencing this quantity, such as texture (elastic anisotropy), defect content, recovery and re-crystallization processes, as well as possible undefined changes in sample geometry, the behavior of resonance frequency will not be considered further. Our considerations will thus focus on the loss factor based on the reasonable assumption that the differences observed between pure Al and the different Al-BN composites are mainly due to modifications of dissipation processes in the Al matrix by the addition of the BN phase, rather than dissipation in the BN phases itself. A rich literature (see e.g. [16-18] and references therein) is available on an elastic relaxation and internal friction mechanisms in Al and related metallic and composite materials. A key factor characterizing the variety of these mechanisms is the interaction and competition between the stress-induced mobility of dislocations and the temperature-induced mobility of point defects. Under the conditions of our vibrating-reed experiments, the following types of dissipation processes, sketched schematically in Figure 3.8, may at least be distinguished:

- *Linear thermoelastic background* (LTB). According to Zener's classical theory of transverse thermal currents, this fundamental damping component should be proportional to the temperature and show a maximum at frequencies $\gg$10 kHz for Al samples with thicknesses $\ll$50 µm. With estimated room temperature loss factors between 0.0001 and 0.0004, the LTB is of little importance in the present frequency interval [18].

- *High-temperature background* (HTB). A roughly exponential increase of damping with temperature common to most materials, connected with thermally activated viscous deformation, and mostly associated with diffusion-controlled dislocation motion.

- *Low-temperature dislocation motion (I)*. The basic mechanism in this range is the so-called Bordoni relaxation, i.e. the bowing-out of locally mobile dislocation segments between immobile pinning points, which involves thermally activated formation and motion of kink pairs. The Bordoni relaxation ideally occurs in pure Al and may be suppressed by segregated impurities, so that it is normally observed only after "fresh" plastic deformation. It may be superimposed by an additional, amplitude dependent component (symbolized by a dashed line in Figure 3.8) from the thermally activated breakaway ("depinning-repinning") of dislocations from point defects [19].

- *Fast point-defect dragging (II)*. While in range I most point defects can be considered immobile on our experimental time scale (milliseconds), with increasing temperature they can increasingly be dragged along with moving dislocation segments. Special types of fast diffusion (such as "pipe diffusion" in the dislocation cores [20], special impurity/ vacancy complexes [21] or complex cooperative processes [22]) must be involved in such dragging processes near and below room temperature where normal volume diffusion of solutes is still too slow. The transition to the pure (amplitude-independent) dragging regime may occur gradually in competition with amplitude-dependent depinning processes, leading to an additional transitory dependence of damping on time (heating rate) [19].

- *Diffusion-controlled loss peak (III)*. The classical interpretation of relaxation peaks at about 500 ~ 600 K in Al is grain-boundary sliding [23-25]. However, details of the microscopic processes are still unclear, and other diffusion-controlled processes such as dislocation climb [26] have also been found in this range. Thus, there may be different types of defects contributing to inelastic deformation and mechanical losses, all of them controlled kinetically by bulk atomic (self-) diffusion and thus appearing in the same temperature range [27].

3. Microcomposites

In melt-spun pure Al (Figure 3.7 (a)), the "grain boundary" peak (III) is most pronounced, while no clear peaks can be distinguished in the low-temperature regime. The loss spectrum hardly changes on annealing, apart from a shift of the peak from about 600 to 570 K, i.e. some apparent acceleration of relaxation kinetics from the as-prepared to the annealed state.
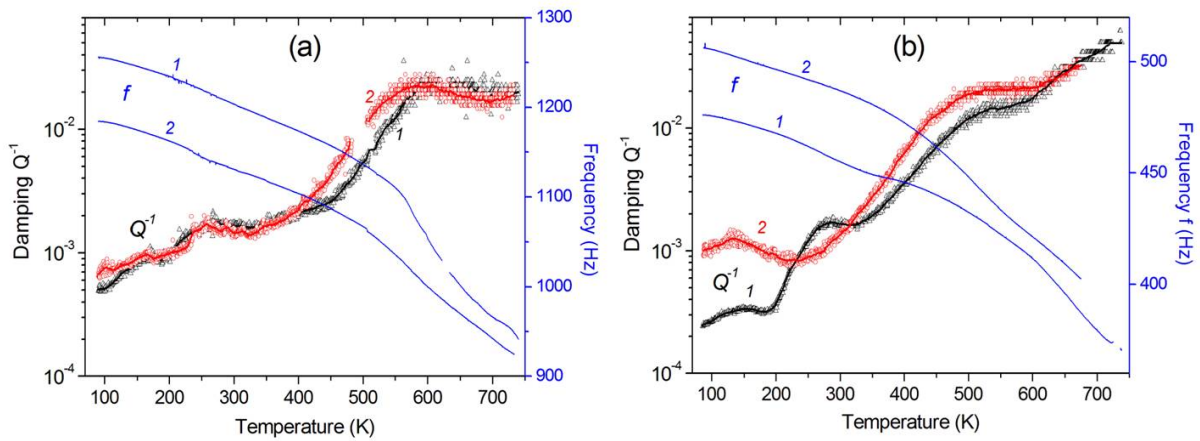

Figure 3.7 Mechanical loss factor (internal friction) Q^{-1} and resonance frequency f of melt-spun samples during two subsequent heating runs at 2 K min^{-1}: (a) pure Al, (b) Al with 5 wt% BNMP (BNMP5), after some plastic bending during clamping The sooth lines for Q^{-1} have been obtained an "adjacent averaging" procedure on the original data points.
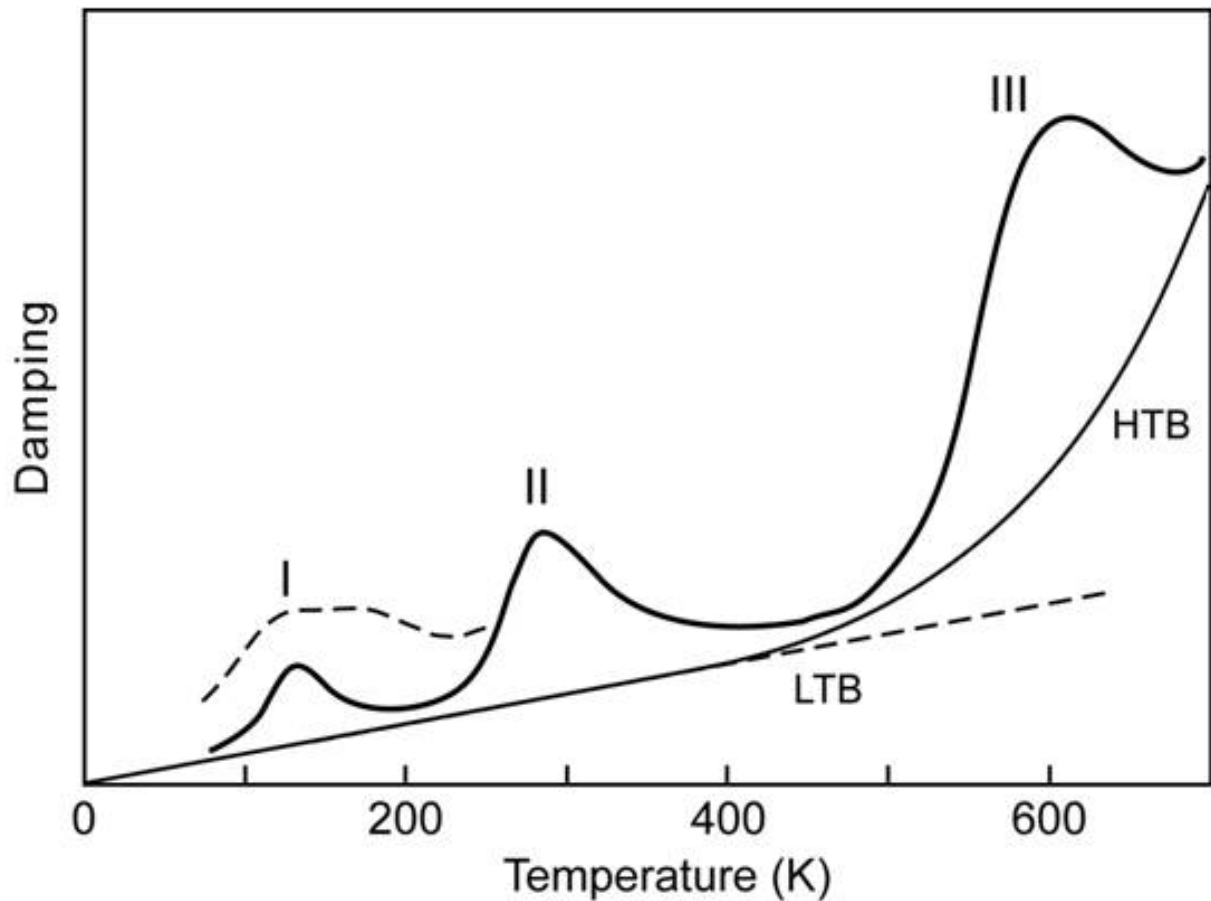
Figure 3.8 Simplified qualitative scheme of temperature-dependent damping effects in Al-based materials at frequencies around 1 kHz (see text).
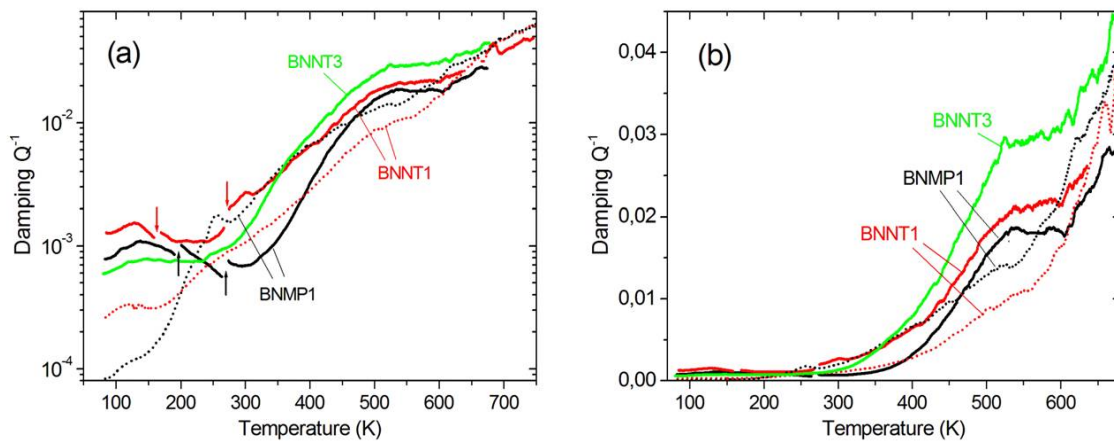

Figure 3.9 Comparison of mechanical loss spectra of melt-spun Al composite ribbons containing 1 wt% BNMPs (BNMP1, 600 Hz), 1wt% BNNTs (BNNT1, 550-1000 Hz with re-clamping, see text), and 3 wt% BNNTs (BNNT3, 650 Hz), respectively. Dotted lines: first heating at 2 K min-1 up to 738-791 K; solid lines: second heating. (a) Logarithmic damping scale (with arrows indicating amplitude jumps at electrode readjustment) and (b) linear damping scale.

3. Microcomposites

In the Al-5.0 wt% BNMP (BNMP5) sample (Figure 3.7 (b)), however, most of the phenomena depicted in Figure 3.8 can be identified; compared to pure Al, the "exponential" HTB (appearing linear in Figure 3.7 (b) with logarithmic Q^{-1} scale) is higher but peak III is smaller, broader and shifted to still lower temperature (~ 500 K). Peaks I and III are enhanced in the second heating run after the sample has been annealed in the first one, while peak II vanishes. As peak II was observed so clearly only in this sample which had been accidentally bent during clamping, it is obviously a result of this unintentional plastic deformation. Amplitude- dependent effects were completely absent in these two cases.

Looking at the different composite ribbons (Figure 3.9), they all show a similar enhancement, not found in pure Al, of the low-temperature Bordoni-type peak I in the second heating run as compared to the first one (regime below 200 K in Figure 3.7 (b) and 3.9 (a)). Such effects are also known from other metal–matrix composites such as Al-SiC [28] or Ni-Al$_2$O$_3$ [15], where they have been attributed to fresh dislocations generated in situ during thermal cycling, as a result of thermal mismatch stresses between metal matrixes and reinforcing ceramic phase accommodated by microplastic deformation. Such microplastic stress accommodation, without interface damage, may be taken as an indication of a good bonding between the Al-matrix and the reinforcing BN phase. A superimposed amplitude dependence, seen as jumps in Q^{-1} during electrode readjustment i.e. change in the distance between sample and electrode and consequent change in the amplitude of vibrations (see above), and possibly indicating additional dislocation depinning processes from point defects-is found in the low-temperature regime only for the second runs of composites with 1.0 wt% BN phase (both BNNTs and BNMPs), but not at higher BN amounts.

In the high-temperature regime, the differences compared with pure Al observed in Figure 3.7 (b) for Al-BNMP 5.0 wt% (higher HTB but relatively smaller, broadened peak III shifted to ~ 500 K, enhanced by annealing) also hold for the composites in Figure 3.9. Generally, both high temperature diffusion-controlled phenomena - the monotonically increasing HTB and the "grain-boundary peak" III - are difficult to separate in the composites. In particular, even in the linear plot of Figure 3.9 (b), hardly any peak can be distinguished from the "background" in the initial, melt-spun state of the composites with 1% wt. BN phase. While the effects described so far are not very different between ribbons reinforced with BN microparticles and nanotubes, respectively, a surprising difference is found in the loss spectra at intermediate temperatures, where both types of composites show opposite annealing behavior: a decrease in mechanical losses for microparticles, but an increase for nanotubes. This opposite behavior is clearly seen in Figure 3.9 for the two samples with 1.0 wt% BN (BNNT1 and BNMP1) in the temperature interval between 250 and 450 K, where the same kind of thermal treatment causes an annihilation of dissipation processes in the composite with microparticles, but a generation of new dissipation processes in the presence of nanotubes. These additional dissipation processes bridge the gap between ranges II and III in Figure 3.9, leading to particularly broad damping spectra both in the first run of the 1 wt% BNMP sample and in the second run of the 1 wt% BNNT sample, respectively. It should also be noted that the damping behavior of the 1 wt% BNNT sample was accompanied by a particularly strong static creep: after the first heating at 2 K min^{-1} up to 791 K, the

horizontally clamped sample was bent downward by almost 90° under its own weight, so that re-clamping at a shorter length (with almost doubled frequency, see Figure 3.9) was necessary for the second measurement.

Unlike the low-temperature regime, the microscopic origin of the effect of nano/micro-BN additions on the internal friction spectra at higher temperatures remains rather speculative at the present stage. A broad spectrum of diffusion paths may generally be offered by the Al/BN interfaces, together with modified dislocation structures, and direct interface sliding cannot be ruled out at high temperatures as well. The higher HTB, together with the shift, broadening, and delayed evolution of the "grain boundary peak" (III), and possibly connected with an enhanced tendency to creep, needs closer examination. A possible interpretation of the opposite annealing behavior of dissipation processes between 250 and 450 K, observed in Figure 3.9 for samples BNNT1 and BNMP1, is that nanotubes may generally be more effective in defect accumulation at thermal cycling, while such defect accumulation might partially be overcompensated by recovery processes in case of composites with microparticles, in particular at low BN amounts.

3.5   General trends

Since the experimental Young's moduli observed in Figure 3.2 are far below the natural values for pure Al, we restrict ourselves to the analysis of the ultimate tensile strength values, and do not discuss quantitatively the elastic properties. This discrepancy is most likely due to the overestimated displacement values during the tensile tests caused by tiny sample sizes, micrometer range thickness and possible sliding within the pneumatic clamps of the large tensile machine under high stresses. Nevertheless, qualitatively there is a clear trend for increasing curve slopes in Figure 3.2 with nano/micro-BN embedding. More accurate elastic and plastic strain values should be measured on a microtensile unit compatible with a scanning electron microscope. These experiments are in our future agenda. Because the absence of possible binary Al-based phases, such as AlB_2 or AlN [3-29-31], was documented in all melt-spun ribbons, the effects of Al-matrix strengthening should be caused by the above-mentioned grain refinement in BN loaded samples (see Figure 3.10) and/or dislocation pinning at nano/micro-BN inclusions. In fact, both studied BN phases distributed within grains (e.g. Figure 3.3 (BNNT) and Figure 3.11 (BNMP)) may hinder the dislocation glide and lead to the restriction of a plastic flow and matrix strengthening. In order to sum up the above-presented data, several important features of the melt-spun composite ribbons should be emphasized. There is a similar trend in significant grain size refinement of nano/micro-BN-loaded samples compared to pure Al ribbons. Nano/micro-BN phases which should be in the solid state from the beginning of Al crystallization (e.g. the hBN melting point (3246 K) is far above that of Al (933 K)) may enhance nucleation and hinder the growth of solid Al grains. The overall number of grain embryos (per sample volume) increases, leading to the observed grain size decrease. Such grain refinement contributes to the tensile stress rise in line with the Hall-Petch relation. There are also clear differences between BNMP- and BNNT-loaded Al-based samples with respect to both internal friction behavior and the strengthening effects. It is known that nano/micro-phases may hinder dislocation glide, thus leading to Al-matrix hardening. This mechanism is widely accepted and

should be applicable here. The nanotubes produce much more profound strengthening of the Al-matrix. This phenomenon agrees well with the model of Kelly [32], who many years ago theoretically demonstrated that strengthening by rods should prevail over strengthening by spheres of the same mass/volume loading. If one takes the averaged geometrical parameters of the present BNNTs, a length of 2 μm and an external diameter of 50 nm, the aspect ratio (*l/d*) becomes 40. According to Kelly's approach, a gain in strengthening of ~ 1.75 should exist for such rods compared to spheres. More recent developments [33], while taking into account the load transfer from matrix to reinforcing agents by means of a shear stress at the interfaces, have also highlighted the importance of an embedded fiber aspect ratio. The increase in the overall composite strength is suggested to be proportional to this ratio, where the fiber length in taken along the stress direction. The dislocation density around the long and thin BNNTs should likely be much higher compared to round BNMPs, verifying the more profound matrix strengthening observed experimentally for the former case. Another concern is a thermal mismatch between BN phases and an Al-matrix. Along the direction perpendicular to the c-axis (i.e. the BNNT axis direction) hBN phases have a coefficient of thermal expansion of -2.7 × 10^{-6} K^{-1} [34], while Al possesses a much higher coefficient of ~ 24 × 10^{-6} K^{-1} Such a large difference between the matrix and filler thermal expansion (i.e. thermal reduction in the case of Al-matrix) would result in the production of significant misfit thermal strains at numerous Al/BN interfaces during rapid crystallization from the melt and subsequent thermal treatments. These strains induce local thermal stresses that may be higher than the yield stress of the Al-matrix and may generate new dislocations at the matrix/reinforcing phase interfaces, which could be detected by the low-temperature Bordoni-type loss peak as discussed above. The interfacial regions thus become good sites for dislocation accumulation. Another process that should be taken into account is so-called Orowan looping [35]. According to this model, the motion of dislocations is inhibited by any sort of precipitate. The dislocations bend between such precipitates and produce a back-stress which prevents further dislocation migration and results in a stress increase. However, this mechanism has no prime significance for rather coarse BNMPs with a large interparticle spacing (see Figure 3.11). By contrast, rather long, randomly distributed BNNTs (see Figure 3.3 (a)), whose length may reach 10–20 lm, present a meaningful obstacle to the dislocation glide. In addition, due to the huge strength of BNNTs, their shearing does not adversely affect the resultant composite strength, though it is known that particle shearing usually restricts the maximum strength that can be achieved along with the Orowan mechanism [36]. A load transfer from the Al-matrix to the embedded reinforcing fillers, so-called shear lag [37], is another important factor to consider [38, 39]. If this transfer exists, then the natural stiffness of nano/micro-BN may fully be utilized. High aspect ratio reinforcements are favored with this model too. The strength of BNNTs is much higher than that of hexagonal BNMPs. The latter are typically deformed by an easy shear due to weak Van der Waals forces, giving a profound lubricant effect which is utilized in a wide range of applications. By contrast, a rigid, fully sealed tubular structure, which particularly exploits the strength of covalent intralayer B-N bonds, leads to a huge ultimate tensile strength of BNNTs exceeding 30 GPa [11]. Perfect wetting between matrix and reinforcing agents is required to fully transfer the load from a weak metal to a strong BNNT. Most likely, this is hardly ever achieved in the present

composites due to the large difference between the surface tension of Al and the nanotubes (~ 865 and ~ 27 mN m^{-1} [40], respectively). However, the particular appearance of BNNTs in tensile tested samples, which are seen being broken in pieces or telescopically pulled out from their external segment at the fractured surfaces (see Figure 3.5 (b and c)), verifies that a load transfer from the Al-matrix to the reinforcing high-strength BNNT agents, has indeed, at least partially, taken place under room temperature tension. This explains the profound reinforcing effect of rather long, stick-like BNNTs (up to 10 ~ 20 lm) and the more modest one in case of round-shaped (~ 1 μm in size) BNMPs which do not directly carry the tensile load and may be cut and/or overcome by moving dislocations.
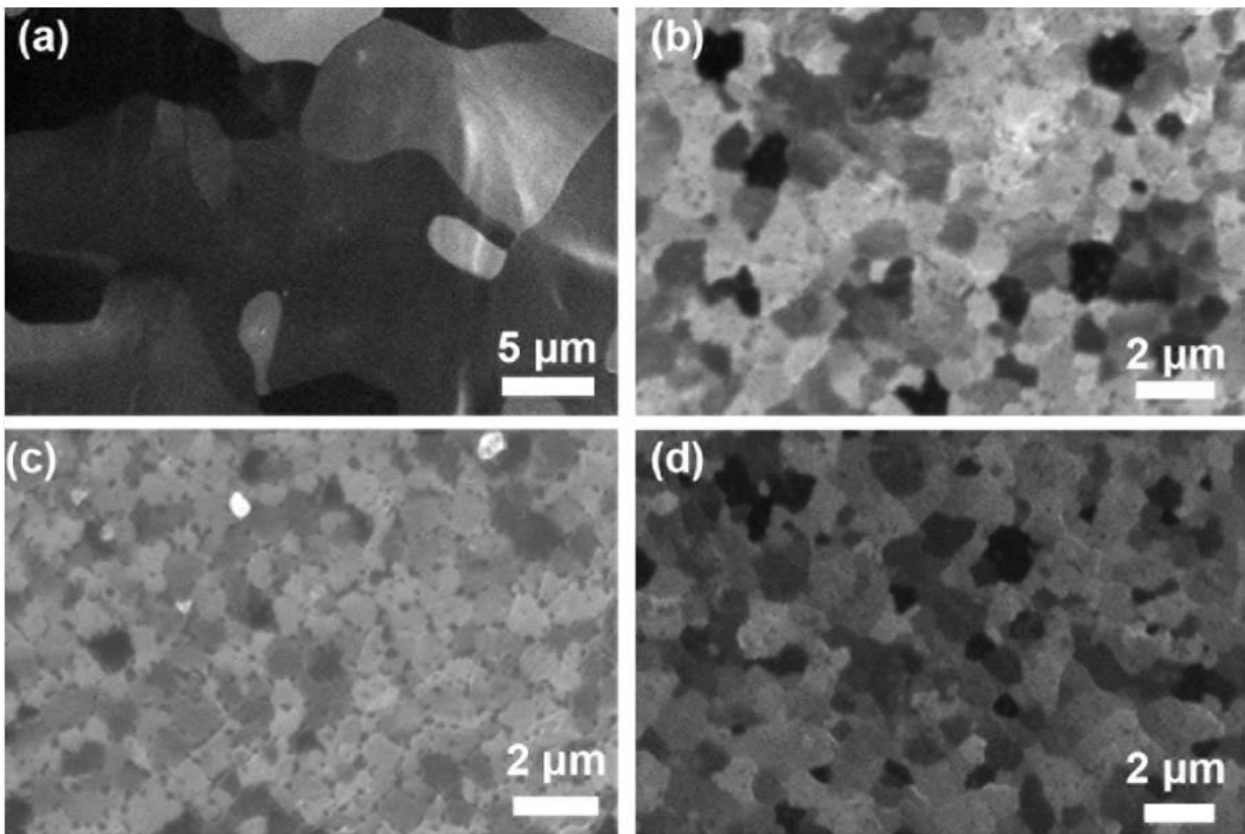

Figure 3.10 Representative optical micrographs revealing the grain structures of pure melt-spun (a) Al ribbons, (b) those with 1wt% of BNMPs, and (c) 1 wt% and (d) 3 wt% of BNNTs, respectively, embedded.
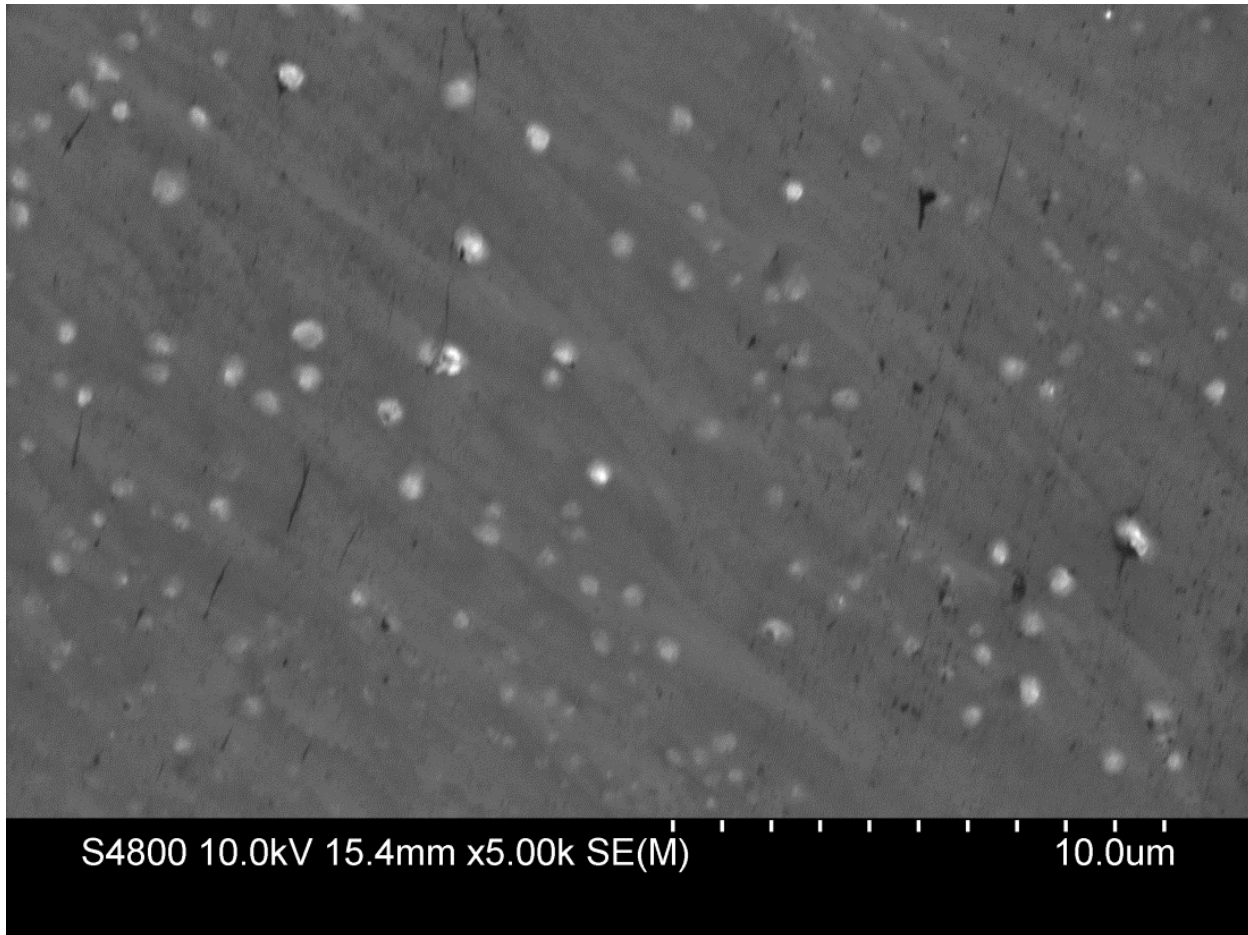
Figure 3.11 Representative comparative SEM images revealing micro BN phases present in the melt-spun Al-matrix.

3.6 Summary

In summary, for the first time, we fabricated Al-BNNT composite ribbons (~ 1 m long) with various multi-walled BNNT (0.5 to 3.0 wt%) or BNMP (up to 5.0 wt%) contents by melt spinning. Scanning and transmission electron microscopy, X-ray diffraction, and energy dispersive X-ray analysis confirmed the decent integration of the two phases into a dense and compact composite. No other phases, like Al borides or nitrides, form in the resultant melt-spun composites. The BNNTs are randomly oriented within the Al matrix and partially participate in carrying the tensile load, as evidenced by their presence and breakage at the composite fracture surfaces. The ultimate tensile strength of the composite ribbons with 3.0 wt% of BNNT at room temperature was more than doubled (145 MPa) compared to non-loaded pure Al ribbons (60 MPa).

Further details of Al-matrix / BN-phase interaction s were studied by means of wide-temperature (80 ~ 800 K) mechanical loss spectra showing a rich variety of dissipation processes. Some of the modifications caused by the BN additions could be attributed to dislocation emission at the Al / BN interfaces due to thermal stresses, to competing accumulation and recovery of defects during thermal cycling, with comparatively more effective accumulation in case of nanotubes, and to an enhanced viscous deformation at high temperature.

3.7   References

[1] S.R. Bakshi, D. Lahiri, A. Agarwal. *Int. Mater. Rev.* **2010**, 55, 41.

[2] Y.B. Li, Q. Ya, B.Q. Wei, J. Liang, D.H. Wu. *J. Mater. Sci. Lett.* **1998**, 17, 607.

[3] C.S. Goh, J. Wei, L.C. Lee, M. Gupta. *Mater. Sci. Eng. A.* **2006**, 423, 153.

[4] C.S. Goh, J. Wei, L.C. Lee, M. Gupta. *Comp Sci Technol.* **2008**, 68, 1432.

[5] H. Uozumi, K. Kobayashi, K. Nakanishi, T. Matsunaga, K. Shinozaki, H. Sakamoto, T. Tsukada, C. Masuda, M. Yoshida. *Mater. Sci. Eng. A.* **2008**, 495, 282.

[6] S.M. Zhou, X.B. Zhang, Z.P. Ding, C.Y. Min, G.L. Xu, W.M. Zhu. *Comp. A.* **2007**, 38, 301.

[7] J.Y. Hwang, A. Neira, T.W. Scharf, J. Tiley, R. Baneree. *Scripta Mater.* **2008**, 59, 487.

[8] T. Kuzumaki, K. Miyazawa, H. Ichinose, K. Ito. *J. Mater. Res.* **1998**, 9, 2445.

[9] W. Salas, N.G. Alba-Baena, L.E. Murr. *Met. Mater. Trans. A.* **2007**, 38, 2928.

[10] D. Golberg, P.M.F.J. Costa, O. Lourie, M. Mitome, X. Bai, K. Kurashima, C.Y. Zhi, C.C. Tang, Y. Bando. *Nano Lett.* **2007**, 7, 2146.

[11] X.L. Wei, M.S. Wang, Y. Bando, D. Golberg. *Adv. Mater.* **2010**, 22, 4895.

[12] S.K. Singhal, A.K. Srivastava, R. Pasricha, R.B. Mathur. *J Nanosci. Nanotechnol.* **2011**, 11, 5179.

[13] A. Pakdel, C.Y. Zhi, Y. Bando, D. Golberg. *Mater. Today.* **2012**, 6, 256.

[14] H.R. Sinning. *J. Phys.: Condens. Matter.* **1991**, 3, 2005.

[15] H.R. Sinning, G. Vidrich, W. Riehemann. *Acta Mater.* **2011**, 59, 4504.

[16] A.S. Nowick, B.S. Berry. *New York: Academic Press.* **1972**.

[17] R. Schaller, G. Fantozzi, G. Gremaud. *Mater. Sci. Forum.* **2001**, 366-368.

[18] M.S. Blanter, I.S. Golovin, H. Neuhäuser, H.R. Sinning. *Internal friction in metallic materials, a handbook. Springer Verlag*, **2007**.

[19] G. Gremaud. *Mater. Sci. Forum.* **2001**, 366–368, 178.

[20] Q.F. Fang, C.C. Wang. *J. Alloys. Compd.* **2000**, 310, 72.

[21] Q.F. Fang, T.S. Kê. *Acta Metall. Mater.* **1990**, 38, 419.

[22] X.S.Guan, H. Numakura, M. Koiwa. *Mater. Trans. JIM .***1999**, 40, 498.

[23] C. Zener. *Phys. Rev.* **1941**, 60, 906.

[24] T.S. Kê. *Phys. Rev .***1947**, 71, 533.

[25] Q.P. Kong, W.B. Jiang, P. Cui, Q.F. Fang. *Solid State Phenom.* **2012**, 184, 33.

[26] M.L. Nó, C. Esnouf , J. San Juan, G. Fantozzi. *Acta Metall.* **1988**, 36, 827.

[27] W. Benoit. *Mater. Sci. Forum.* **2001**, 366–368, 306.

[28] S. Kustov, S. Golyandin, K. Sapozhnikov, A. Vincent, E. Maire, G. Lormand. *Mater. Sci. Eng. A.* **2001**, 313, 218.

[29] Z.P. Xia, Z.Q. Li, C.J. Lu, B. Zhang, Y. Zhou. *J. Alloys. Compd.* **2005**, 399, 139.

[30] Y. Du, S. Li, K. Zhang, K. Lu. *Scripta Mater.* **1997**, 36, 7.

[31] Y.F. Han, Y.B. Dai, J. Wang, D. Shu, B.D. Sun. *Appl. Surf. Sci.* **2011**, 257, 7831.

[32] P.M. Kelly. Scripta Metall. 1972, 6, 647.

[33] Z. Trojanova, Z. Szaraz, J. Labar, P. Lukac. *J Mater. Process. Tech.* **2005**, 162–163, 131.

[34] M.E. Levinstein, S.L. Rumyantsev, M.S. Shur. *John Wiley & Sons*, **2001**, 67.

[35] Orowan E. Z Phys 1934;89:634.

[36] R. George, K.T. Kashyap, R. Rahul, S. Yamdagni. *Scripta Mater.* **2005**, 53, 1159.

[37] Clyne TW. An introduction to metal matrix composites. Cambridge: Cambridge University Press; 1995. p. 26.

[38] Q. Li, C.A. Rottmair, R.F. Singer. *Comp. Sci. Technol.* **2010**, 70, 2242.

[39] Bakshi SR, Agarwal A. *Carbon.* **2011**, 49, 533.

[40] Yum K, Yu MF. *Nano Lett.* **2006**, 6, 329.

Chapter 4

Macrocomposites

4. Macrocomposites

Chapter 4 Macrocomposites

4.1   Introduction

Since I have shown promising results in the previous chapters in regards of nano- and micro-composites of Al-BNNTs, they may be considered as a prospective and promising "superlight" and "superstrong" material. Here I prepared "cm" range samples to address their issues of their structures and mechanical properties; these materials are referred below as d "macrocomposites".

Most of the MMC-CNT composites are produced by powder metallurgy techniques such as mechanical alloying, sintering, hot pressing and compacting [1]. After the initial mixing step a blend of CNTs and metal is consolidated to high density. This step is the key for making bulk samples with a good dispersion of nanotubes within a metal matrix. A wide range of compaction processes is applied to reach a sufficient densification, such as spark plasma sintering (SPS) or high-pressure torsion (HPT).

SPS is a comparatively new sintering technique and some researchers used it for CNT-MMCs studies (mostly for Al [2] and Cu-CNT systems [3, 4]). The main characteristic of this technique is that the pulsed DC current directly passes through a graphite die, as well as the powder compact, in case of conductive samples. Joule's heating effect was found to play a dominant role in the densification of powder compacts which had resulted in achieving near theoretical density at a lower sintering temperature compared to conventional sintering techniques [5]. The heat generation is internal, in contrast to the conventional hot pressing, where the heat is provided by the external heating elements. This facilitates very high heating or cooling rates and the sintering process generally is very fast (within a few minutes). The general speed of the process ensures that it has the potential of densifying powders with nanosize dimensions or those made of nanostructures while avoiding coarsening which accompanies standard densification routes. While the term "SPS" is commonly used, such term is somewhat misleading since neither a spark nor plasma are present in the process [6]. It has been experimentally verified that densification is facilitated by the use of a current. There is only one report about SPS-made Al-BNNTs composite from by *Lahiri et al.* [7]. The authors state that BNNTs survive the high pressure and temperature over prolonged time needed for SPS. And micro-pillar compressive tests show 450% improvement in both yield and compressive strength with 5.0 vol% BNNT addition in an Al matrix. Kwon *et al.* [8] and Kurita *et al.* [9] mentioned that CNTs were well dispersed into Al matrix by using hetero-agglomeration principle and 5.0 vol% CNTs addition could remarkably elevate the strength to about thrice that of pure Al. The improved mechanical properties were attributed to particular strengthening by the CNTs, which strongly bonded with the matrix through the generated aluminum carbide phase [8]. A fully dense 1.0 vol% MWCNT-Al matrix composite bulk has demonstrated a 40 % improved tensile strength with respect to pure Al and an elongation to failure was of 27.3 % similar to that of cast pure Al [9]. Other than the mechanical properties study, thermal properties are also one of the most important topics for the MMC-CNTs research (Al [10], Cu [11, 12]). In the SPS-related

section below, I show the fabrication process of Al-BNNT macrocomposites, their structural analysis, mechanical and thermal property results and discuss them.

HPT is one of severe plastic deformation (SPD) techniques which allow achieving ultrahigh deformations without heating, under the vacuum or sintering conditions. Although HPT method is generally applied for the grain refinement in bulk coarse-grained metals [13, 14], it is also capable to consolidate pure metallic powders [14] or their blends with CNTs [15, 16]. Due to the very high applied pressure and imposed strain, ultrafine-grained (UFG) or nanocrystalline microstructures can be achieved in the consolidated samples, even if the initial powder consists of coarse grains. Grain refinement is important for increasing hardness according to the Hall-Petch relationship [17]. For the MMC-CNT works by HPT, Al [18-20] and Cu [21-23] have been the main metal candidates, similar to SPS studies. Tokunaga *et al.* [18], Joo *et al.* [19] and Janei *et al.* [21] studied the difference of hardness depending on the area from the center of the samples [18] because the torsion under high pressure may differently affect the central and edge sample areas. In this section, I focus on the structural analysis of HPT-made Al-BNNTs compacts and their mechanical properties using hardness and tensile strength test and study the effects of torsion on an Al-BNNTs macrocomposite.

4.2 Spark plasma sintering (SPS)

4.2.1 Experimental conditions

Multi-walled BNNTs were synthesized by boron oxide-assisted CVD (BOCVD) method, as was reported in our previous chapters. After subsequent high-temperature purification in argon atmosphere, the BNNTs were dispersed in ethanol using ultrasonic agitator for about an hour. As mentioned earlier, this dispersion process is the key for making macrocomposites with respect to perfect nanotube dispersion in a bulk metal matrix, as was previously documented for CNTs The clue of such dispersion is that functional groups are attached onto nanotubes, and the electrostatic repulsive force between nanotubes overcomes the Van der Waals forces leading to a homogeneous nanotube suspension within a solvent. There are some reports which used special dispersion processes such as nanoscale dispersion (NSD) [24, 25], surface modification processes using acid [9] or molecular level mixing process [26]. The NSD process using nitric acid was also tried for the BNNTs, however, it did not work well like for the CNTs. It would be better having simpler way for powder mixing preparation process, and so I decided to use only ethanol, as I did for the microcomposites, but made the dispersion time longer. After BNNTs were dispersed well in ethanol, an Al powder (20 μm, 99.9%, Kojundo Chemicals, Japan) was added into the BNNTs-ethanol solvent and mixed by a stirrer for about 2 hours. Ethanol should be evaporated after the sample preparation. It took longer time to make an Al-BNNTs powder mixture compared to processing of melt-spun samples as it would be more severe dispersion issue for bigger samples than for micrometer thick ribbons.

The Al-BNNTs powders were prepared with 1.0 to 5.0 wt% (1.9 to 9.6 vol%) BNNTs. The dried powder mixtures were consolidated by SPS (Dr Sinter SPS-511S, Sumitomo Coal Mining Co., Japan) in

vacuum at 600 °C and 50 MPa pressure for 20 min in a graphite die, the heating rate was 60 °C/min. Figure 4.1 shows the schematics of the SPS apparatus.

The phase compositions were identified by X-ray diffraction (XRD; RINT2000 Ultima III, Rigaku Corporation, Japan) using Cu Kα radiation. The morphologies of polished and fractured sample surfaces were investigated by scanning electron microscopy (SEM; S4800, Hitachi Ltd., Japan) and high-resolution transmission electron microscopy (TEM; JEM-2100F (200 kV), JEM-3000F (300 kV) and JEM-3100FEF (Omega filter) instruments, all made by JEOL Ltd., Japan). TEM samples were prepared by using focused ion beam (FIB) polishing. Energy dispersive X-ray spectrometry under SEM and TEM investigations (EMAX EX-220, Horiba Ltd., Kyoto, Japan; JEM-3100FEF microscopes) at accelerating voltages of 10 kV (SEM) and 300 kV (TEM), respectively, were employed to identify the composite chemistry and to spatially map the constituting species. Microhardness was determined by Vickers indentation using a diamond indenter (Durascan 70, EMCO-TEST Prüfmaschinen GmbH, Austria) under a load of HV0.2. All the reported values were the average of at least 4 measurements.

Additionally, thermal diffusivity measurements were performed by a laser flash apparatus (Thermal constant analyzer TC-7000, ULVAC-RIKO, Japan) at room temperature. A disk specimen with a diameter of 10 mm and 2 ~ 3 mm thickness was used. A layer of colloidal graphite spray was coated onto the surface of the sample for enhancing the absorption of Xenon light pulse energy and the emission of infrared (IR) radiation to the temperature detector.
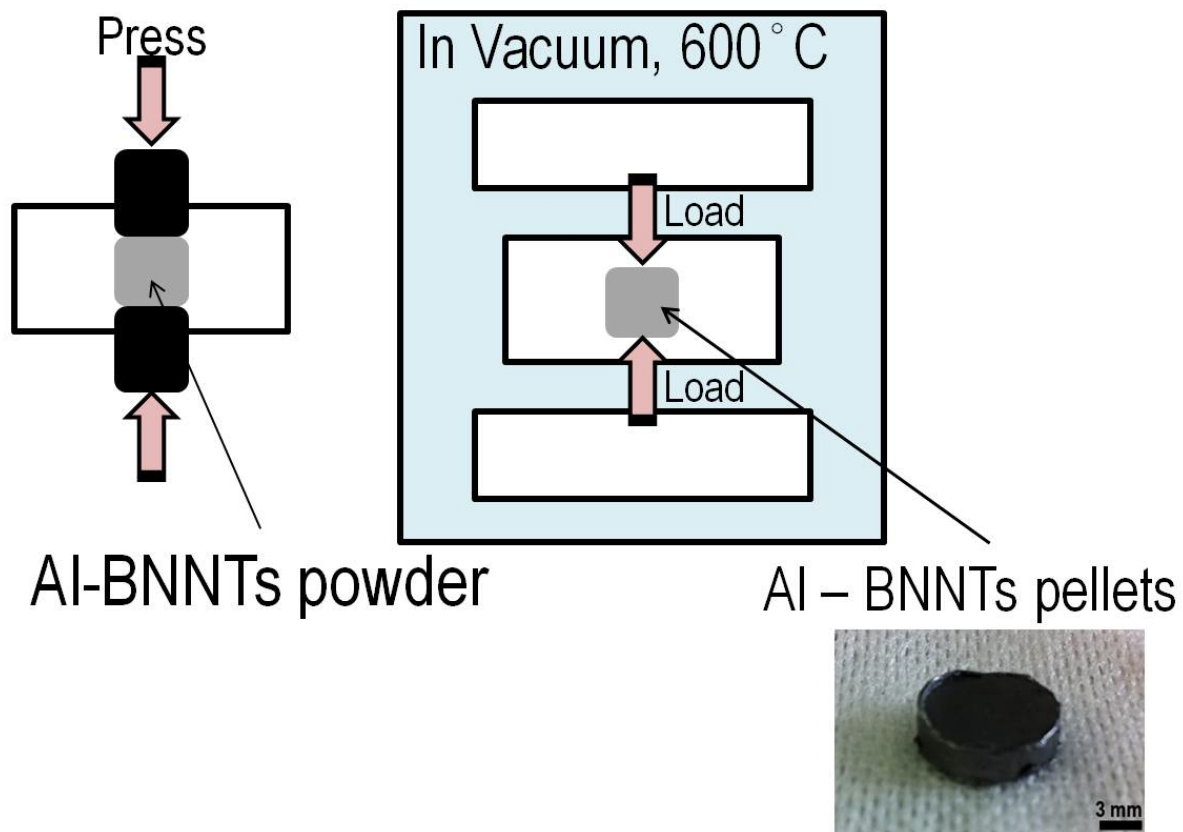

Figure 4.1 A schematic image of spark plasma sintering (SPS). The SPS-made compact has a 10 mm diameter and about 2-3 mm thickness (image on the right side)

4.2.2 Structural characterization and mechanical properties analysis

Figure 4.2 shows optical microscopy and SEM images taken from an Al-BNNT 3.0 wt% SPS pellet after polishing and chemical etching. Polishing and chemical etching methods used for this compacts are sketched in appendix. The Al grain size was about 10 ~ 20 μm, as seen in Figure 4.2 (a). Many BNNTs were found bundled at the Al grain boundaries (Figure 4.2 (b)). Figure 4.3 shows XRD spectra before (a) and after SPS (b). Before and after SPS, Al is polycrystalline. A weakly visible BN (0 0 2) peak can be seen at 26.63 ° (inset in Figure 4.3 (a)). Those results proved that no other phases like Al borides or nitrides had been formed in the Al-BNNTs composite. Figure 4.4 shows high-resolution TEM images of an obtained Al-BNNT 3.0 wt% composite. Aluminum triple grain boundaries are seen in Figure 4.4 (a). Figure 4.4 (b) and (c) depict the nanotubes located inside the grains (b) or somehow assembled along the grain boundaries (c).
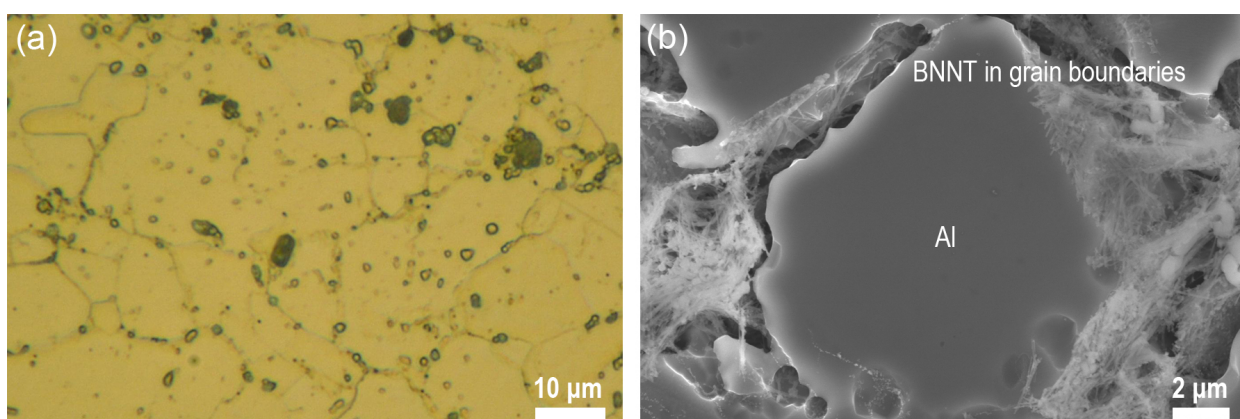
Figure 4.2 An optical microscopy (a) and a SEM image (b) of SPS-made compact sample after polishing and etching. The Al grain size is about 20 ~ 50 μm according to (a). BNNTs are embedded along the grain boundaries (b).

Representative room temperature microhardness test results on pure sintered Al samples and those with various BNNT loading fractions are presented in Figure 4.5. The maximum measured hardness of SPS compact was 35 MPa (Al) and the hardness was slightly decreased with increasing amount of BNNTs in the composites. As pure Al and Al-BNNT composites exhibit nearly similar microhardness values – it means that BNNTs made little change to pure Al structure. Kurita et al reported that the hardness of the Al-CNT 5 wt% SPS sample was about 35 MPa, about the same value as measured here [49]. Good dispersion and alignment of nanotubes in the matrix, as well as formation of decent metal/nanotubes interface were found to be the prime factors for the improvement of mechanical properties [27]. Since many nanotubes in the present samples were seen at the grain boundaries, the dispersion process had not been effective enough, also the interfaces of Al / BNNTs were probably not so tight. All these factors led to a notable microporosity of Al-BNNTs bulks structure, detrimental for the mechanical performance.
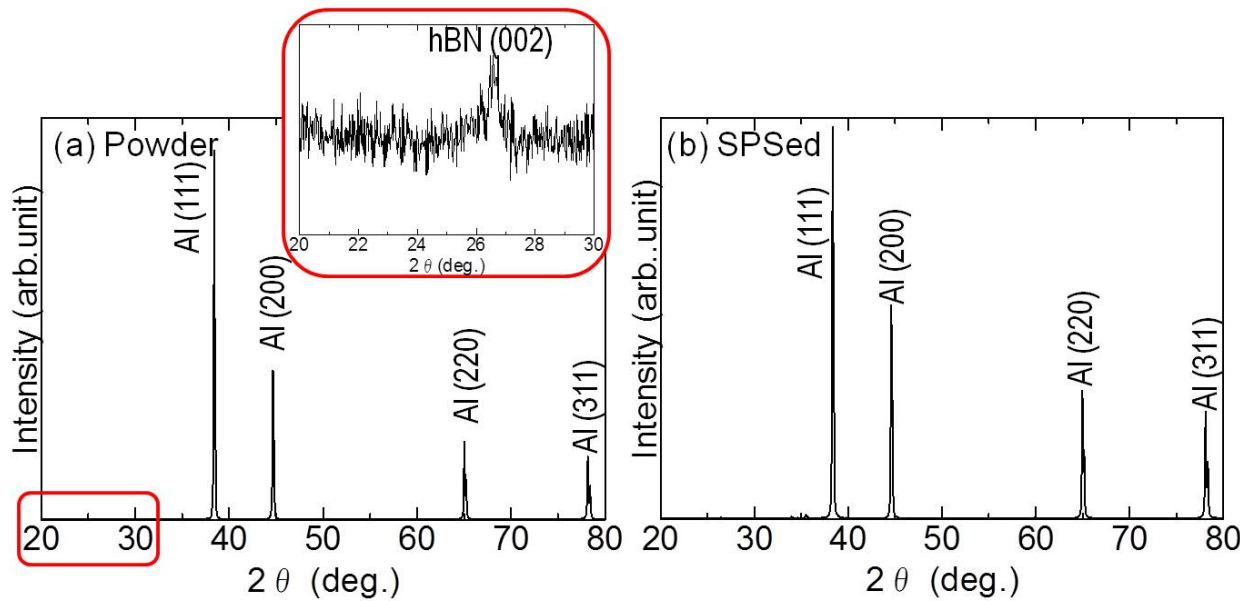
Figure 4.3 XRD spectra of an Al-BNNT mixture powder (a) and a SPS-made pellet using this powder (b). Al is polycrystalline and BN phase shows characteristic hBN (0 0 2) reflection at 26.63° (inset in (a)). Al and BN phases do not make any new components such as AlN or AlB_2 within the composite.
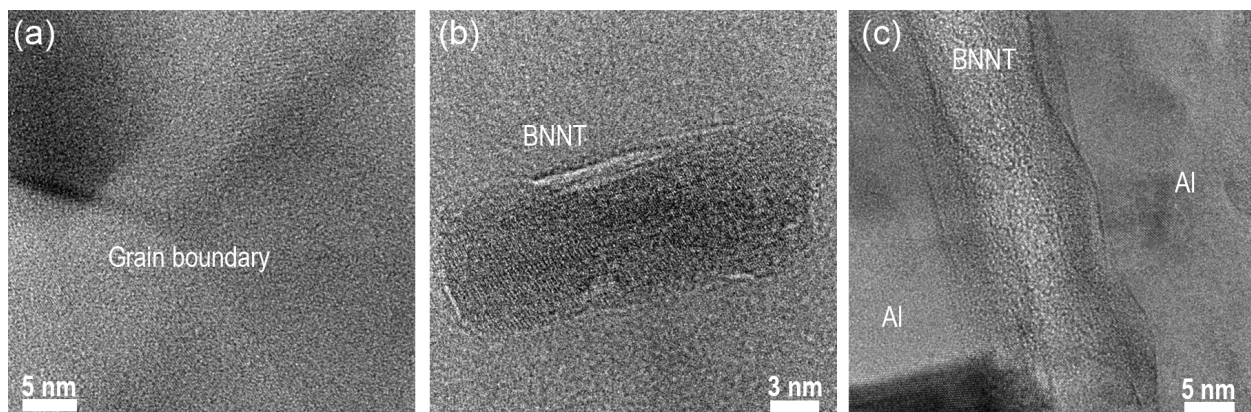

Figure 4.4 TEM images of an Al-BNNT 3wt% macrocomposite by SPS. (a) Grain boundaries in Al. BNNTs were rarely found within Al grains (b) and mostly along the grain boundaries (c).

4.2.3   Thermal diffusivity

Figure 4.6 depicts the schematic image of a laser flash apparatus that was used to measure thermal diffusivity. An energy pulse heats one side of a plane-parallel sample. The temperature rise on the backside due to the energy input is time-dependent detected. The higher the thermal diffusivity of the sample, the faster the heat reaches the backside. The thermal diffusivity of Al was 1.04 cm^2/s and that of Al-BNNT 1 wt% was 0.95 cm^2/s. A bulk Al (1.9 cm square) thermal diffusivity is 0.86 cm^2/s at 20 °C [28] and there is no big difference compared to my experimental data, so the measured values look reasonable. This is contrary to the expectations of improved thermal diffusivity due to the additions of BNNTs, however the overall almost unchanged (or even slightly decreased) thermal diffusivity of the Al-BNNT composite leads us to the

conclusion that the BNNT clusters at grain boundaries might be the reason for this, a hitherto obvious but unproved notion. Agarwal *et al.* mentioned that well dispersed nanotubes could make the thermal diffusivity better for an Al-CNT composite, however if there are any CNT clusters within the Al matrix, those might cause the thermal diffusivity decrease [10].
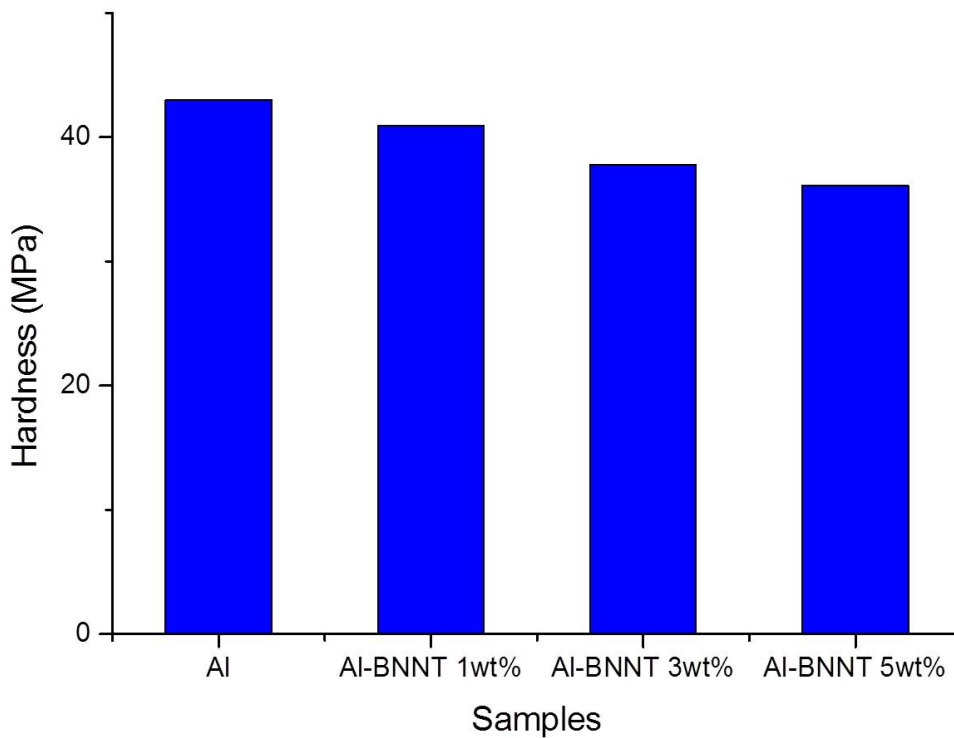

Figure 4.5 Micro-Vickers hardness comparisons of pure Al and Al-BNNTs macrocomposites by SPS. The hardness is slightly decreased with increasing BNNT contents.
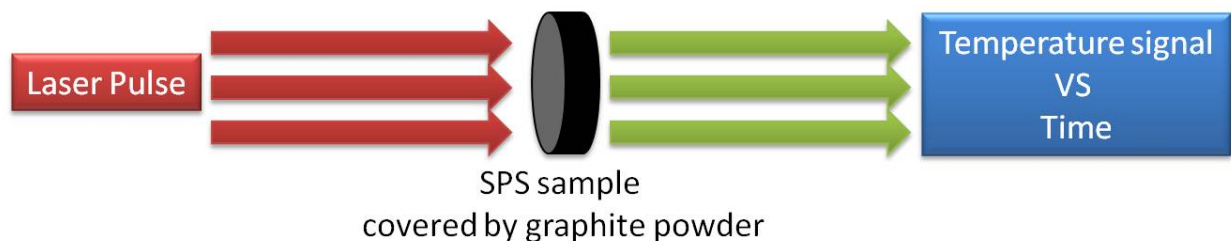
Figure 4.6 A schematic image of Laser flash method to measure thermal diffusivity of pure Al and Al-BNNT 1 wt% SPS-made samples. The SPS pellets were coated with a graphite powder to provide a stable laser pulse.

4.3   High-pressure torsion (HPT)

4.3.1 Experimental conditions

The same Al-BNNTs powder mixtures were used as those for the SPS experiments in this work. The dried powder mixtures were compacted by HPT (REP-HPT-60-05, Riken Enterprise Co., Ltd., Japan). Approximately 0.1 g of the powder mixture was put in a circular shallow hole of 10 mm in diameter and located at the center on the lower anvil of the HPT machine, as illustrated in Figure 4.7. The lower anvil was lifted to contact the upper anvil having the same dimensions as the lower anvil, and was rotated with respect to the upper one at a rotation speed of 1 rpm. This HPT operation was undertaken at room temperature with an applied pressure of 2.5 GPa. The rotation was initiated 10 s after the load application and terminated after 10 turns. The sample's thickness was about ~ 0.5 mm.

The phase compositions were identified by X-ray diffraction (XRD; RINT2000 Ultima III, Rigaku Corporation, Japan) using Cu Kα radiation. The morphologies of polished and fractured sample surfaces were investigated by scanning electron microscopy (SEM; S4800, Hitachi Ltd., Japan) and high-resolution transmission electron microscopy (TEM; JEM-2100F (200 kV), JEM-3000F (300 kV) and JEM-3100FEF (Omega filter) instruments, JEOL Ltd., Japan). TEM samples were prepared by using focused ion beam (FIB) polishing. Energy dispersive X-ray spectrometry under SEM and TEM investigations (EMAX EX-220, Horiba Ltd., Kyoto, Japan; JEM-3100FEF microscopes) at accelerating voltages of 10 kV (SEM) and 300 kV (TEM), respectively, were employed to identify the composite chemistry and to spatially map the constituting species. Microhardness was determined by Vickers indentation using a diamond indenter (Durascan 70, EMCO-TEST Prüfmaschinen GmbH, Austria) under a load of HV0.2. All the reported values were the average of at least 4 measurements. Also tensile strength was measured at room temperature by using a tensile test machine (AUTOGRAPH AGS-10KNJ, Shimadzu, Japan) at a deformation rate of 2.0 $\times 10^{-3} s^{-1}$. The displacements were controlled by a video extensometer with a 3 μm resolution. The samples were cut to "dog bone" shapes by electrical discharge machining (EDM). All the reported values were the average of at least 4 tested samples.
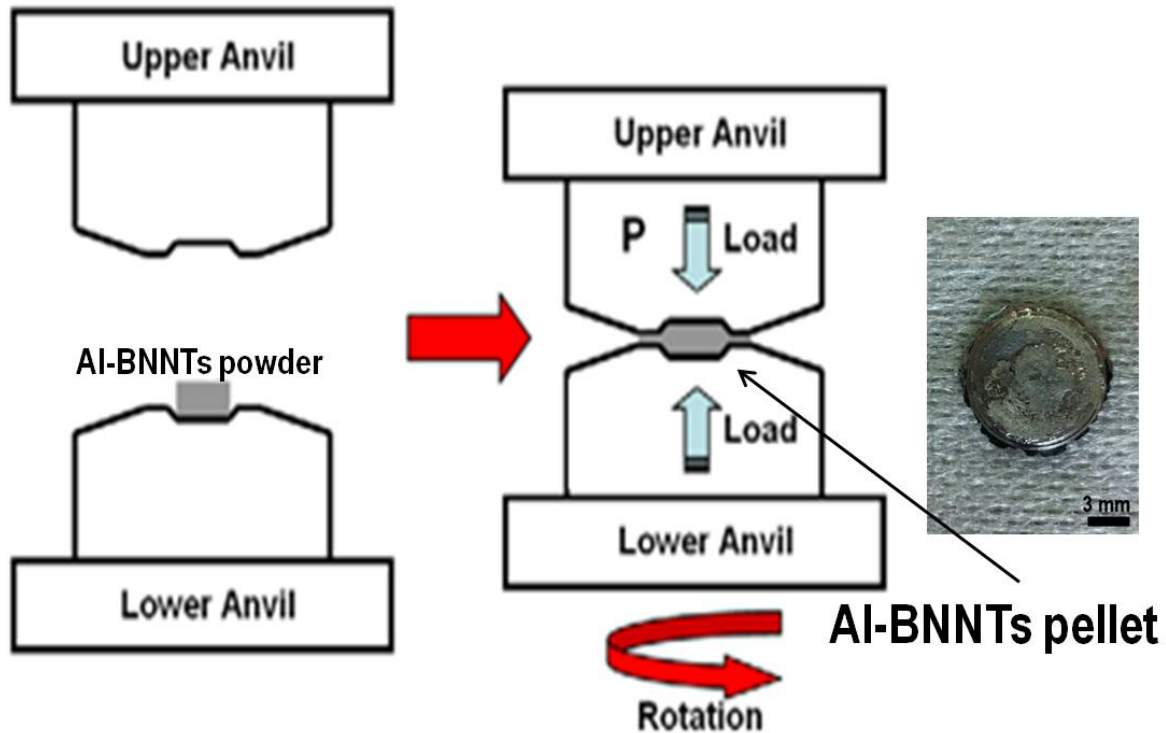
Figure 4.7 A schematic image of high-pressure torsion. A mixed powder was put into the lower anvil and uploaded toward the upper anvil.

4.3.2 Mechanical properties and structural characterization analysis

Figure 4.8 illustrates the micro-Vickers hardness data of pure Al and Al-BNNT HPT-made samples. Hardness increased with increasing BNNTs contents. The hardness of pure Al is ~ 90 MPa and the Al-BNNT 3 wt% is ~ 190 MPa, so the hardness became more than doubled compare to that of pure Al. The hardness differences for various samples were checked, as shown in Figure 4.9. 10 to 12 points were measured for each section. With increasing BNNT content, the error bar is getting larger and it was more than 50 MPa differences in the Al-BNNT 5 wt% sample. On all areas, the hardness value is increased with increasing BNNT content compared to pure Al samples. In plain areas, in the central part the hardness values are larger compared to their edge parts. On the other hand, in the cross sectional area, the edge parts tend to have higher hardness values. Since pure Al sample has constant hardness data in any area, it could be said that BNNTs made the whole structure hardness less homogeneous.

Additionally, hardness tests were carried out after the heat treatment at 370 and 470 °C for an hour. Hardness is decreased after sample annealing, as seen in Figure 4.10. This is a reasonable result as the Al grain size would become bigger with heat treatment [29]. These annealing temperatures might be too high for hardening Al-BNNTs macrocomposite samples according to the literature. In fact, there has been a report that by choosing the right combination of annealing temperature and time, a desired combination of strength and ductility can be achieved. The focus has been on nanostructured metals that have extreme strength but limited ductility and formability, which reduces their applicability. The extreme strength has been obtained through a structural refinement of the grains down to nanometer dimensions, and the optimization of ductility has been sought through annealing [30].
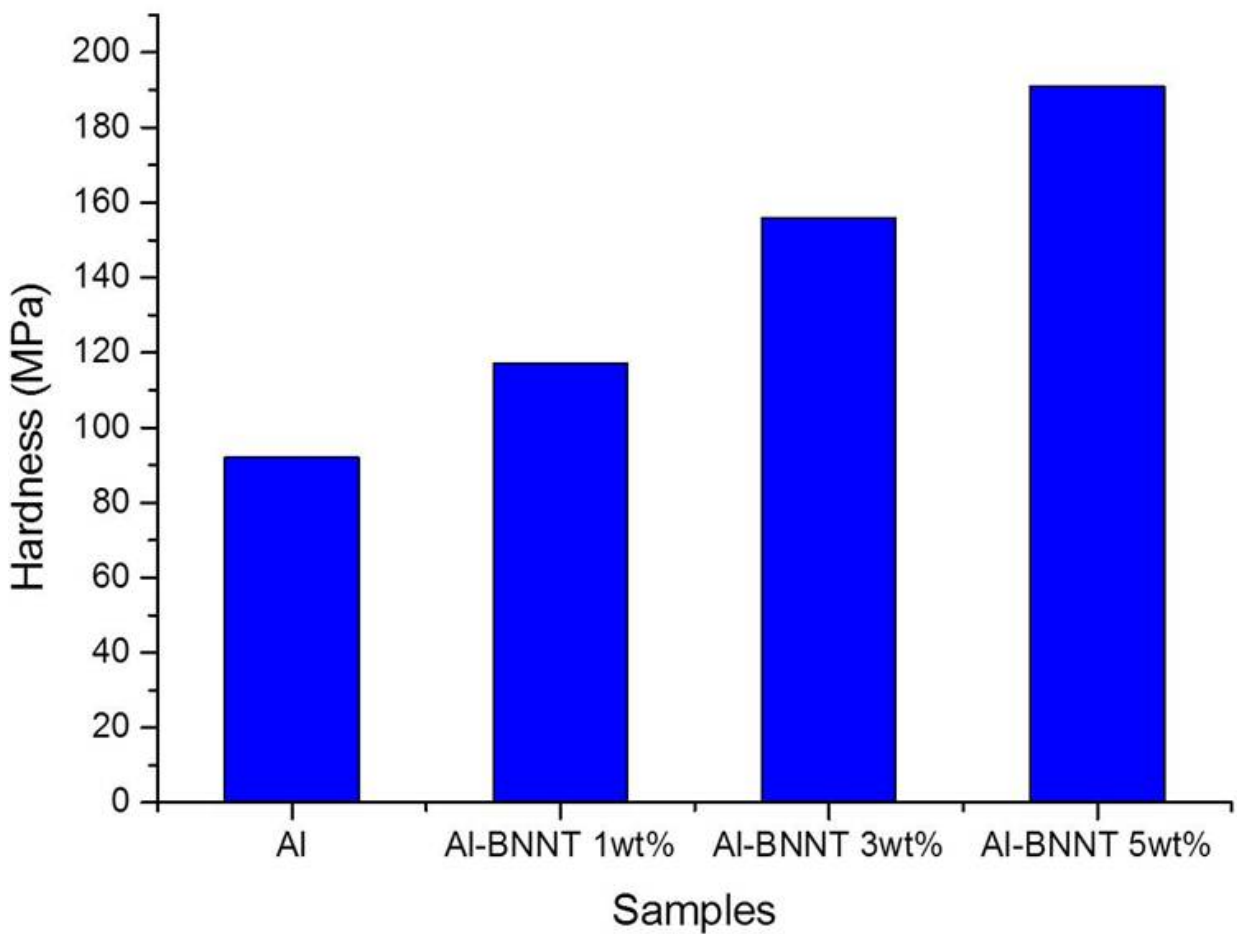

Figure 4.8 Micro-Vickers hardness comparison of pure Al and Al-BNNTs macrocomposites by HPT. The hardness increased with increasing BNNT contents. The hardness of Al-BNNTs 3 wt% is ~ 190 MPa; thus it became more than doubled compared to pure Al (~ 90 MPa).

Representative room temperature stress-strain curves of a pure Al HPT sample and those with various BNNTs fractions are shown in Figure 4.11. The maximum measured strength was 350 MPa (Al-BNNT 3.0 wt%) and that of Al-BNNT 1.0 wt% and Al were around 200 MPa. The curves for Al and Al-BNNT 1.0 wt% samples look nearly similar, as we have early seen for the melt-spun samples in Chapter 3, *i.e.* low BNNTs contents cannot modify the material tensile properties. However, for a 3.0 wt% BNNT sample, the

tensile strength and the slope of the curves (and thus the Young's modulus) dramatically changed. The averaged ultimate tensile strength is ~ 1.5 times larger than that of pure Al. This value is already comparable with the tensile strength of an alloyed steel, like, for example, A36 (that has 400 MPa tensile strength) but our composite material is 3 times lighter (density of ~ 7.5 and 2.5 g/cm^3, respectively). Compared between pure Al and Al-BNNT composite samples, the strain behavior is notably different. The strain to fracture for pure Al is ~ 0.25 while for an Al-BNNT 1.0 wt% it is 0.10 and for a 3.0 wt% it is 0.06. It could be said that the strain is decreased with increasing BNNT content. To see the difference in the fracture surfaces, herein the SEM images of the fractured pure Al and Al-BNNT 3 wt% samples are illustrated in Figure 4.12. The pure Al HPT-made sample has a typical dimple-like fracture surface, consistent with a large strain range of a plastic flow, see Figure 4.12 (a). More or less similar features are seen at the low loading
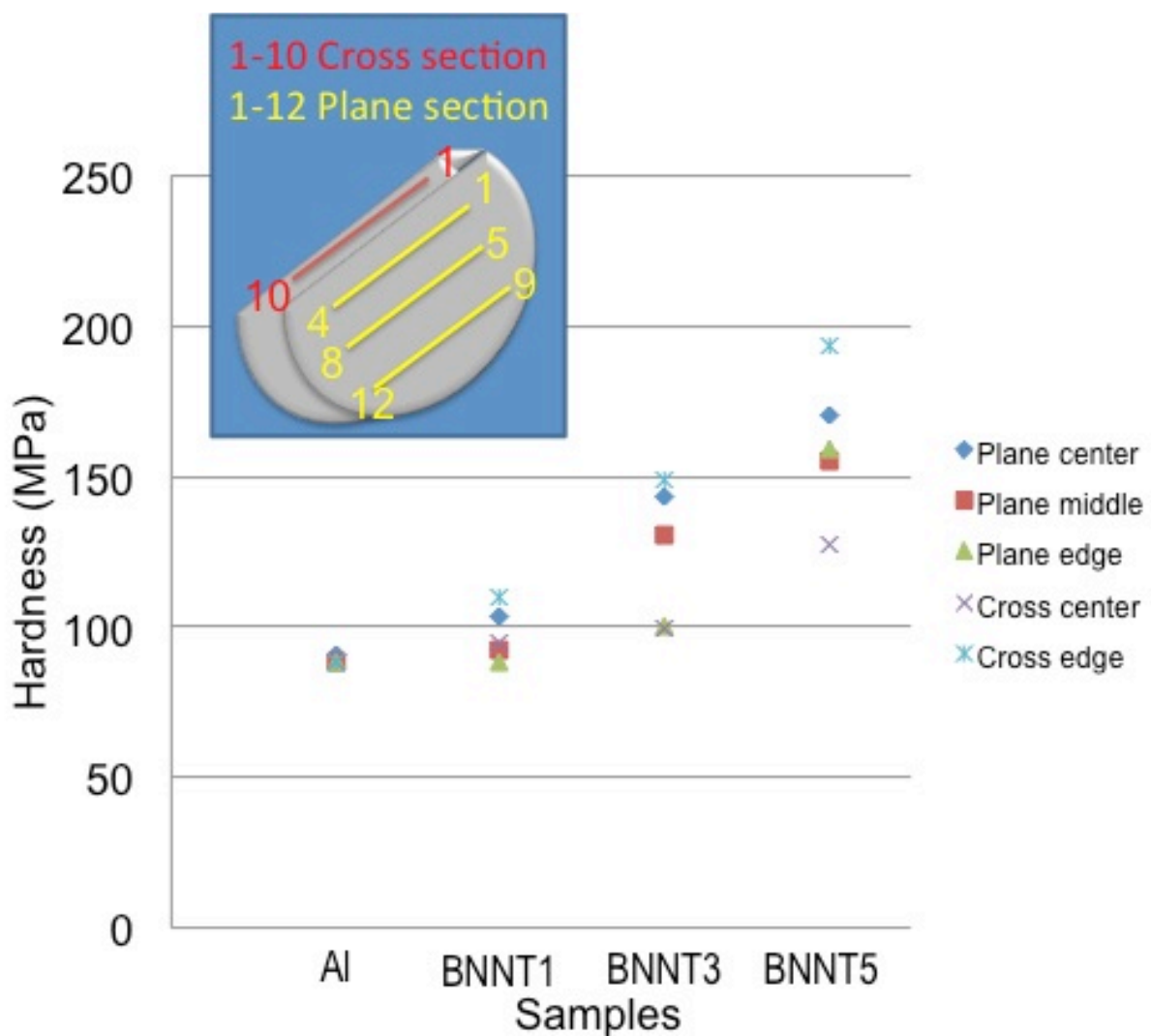

Figure 4.9 The micro-Vickers hardness comparison of HPT-made pure Al and Al-BNNTs macrocomposites within selected areas. (Al-BNNT 1 wt%: BNNT1, Al-BNNT 3wt%: BNNT3 and Al-BNNT 5wt%: BNNT5 in the graph). Hardness tests were carried out from two sides of the samples (cross section and in plain). The error bar is getting larger with increasing BNNTs contents but there is no notable area dependence. All the areas show that the hardness increased with increasing BNNTs contents.

fraction of BNNT (1.0 wt%), Figure 4.12 (b), however the dimple structure becomes more coarse with much less developed dimple network evident. Some traces of transgranular fracture are apparent in Figure 4.12 (b). However the fracture surfaces of BNNT-containing samples at high BNNT loading fraction (3.0 wt%) tend to demonstrate a sort of brittle transgranular failure. The image in Figure 4.12 (c) depicts that in some parts the nanotubes fully survived after the sample breakage. Individual BNNTs create a crossed bridge between two portions of an Al matrix through the existing micropore, thus cementing the whole structure, in accord with the observed drastic increase in a HPT composite hardness and strength noticed in Figures 4.8 and 4.11, respectively.
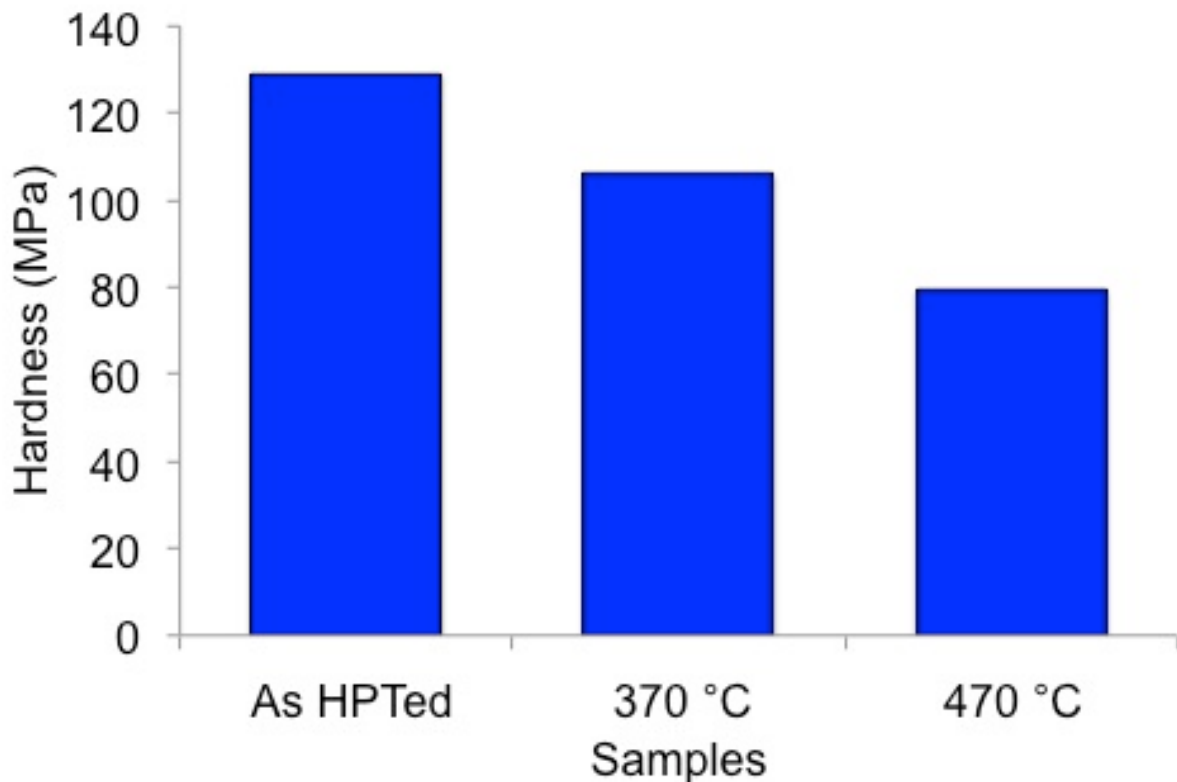

Figure4.10 The micro-Vickers hardness comparison of Al-BNNT 1 wt% samples after 1 hour heating at 370 and 470 °C. With increasing annealing temperature, the hardness decreased slightly. It is considered that Al grains grew under heating and the sample becomes softer.

Figure 4.13 shows a XRD spectrum of an Al-BNNT 3.0 wt% HPT pellet. Same Al-BNNTs mixed powder was used as that for SPS samples see Figure 4.3 (a). As for nano- and microcomposite samples shown in the former chapters, Al was polycrystalline. Again, no other phases like Al borides or nitrides form in the Al matrix according to a detailed X-ray analysis. Figure 4.14 depicts low- and high-resolution TEM images of the Al-BNNT 3.0 wt% HPT composite near its fracture area after the tensile test. The clean Al nanoscale grains and some nanotubes are seen even on the low-magnification image (a). It can be seen that BNNT is torn out at the Al grain boundary (b) and may even be totally collapsed during the HPT process (c). Also Al and BN diffraction patterns were detected in Figure 4.14 (c). With a twisting force and high pressure

during HPT processing, BNNTs were not able to entirely keep their straight morphology in the Al matrix while carrying the load. Some of them could be found whirled, smashed and/or entagled (Figure 4.14 (c)).
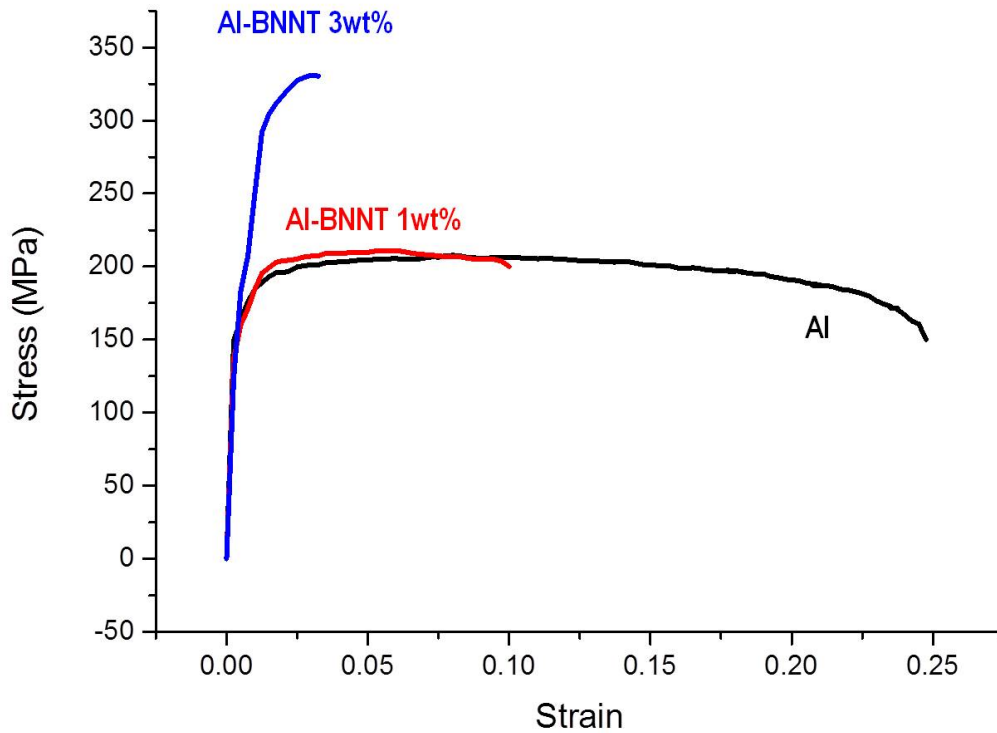

Figure 4.11 Engineering stress-strain curves of pure Al and Al-BNNTs macrocomposites by HPT. The ultimate strength increased with increasing BNNTs contents. For an Al-BNNT 3wt% composite, it is ~ 300 MPa, which is ~ 1.5 times larger than for pure Al (200 MPa). On the other hand, the strain is decreased with increasing BNNTs contents.
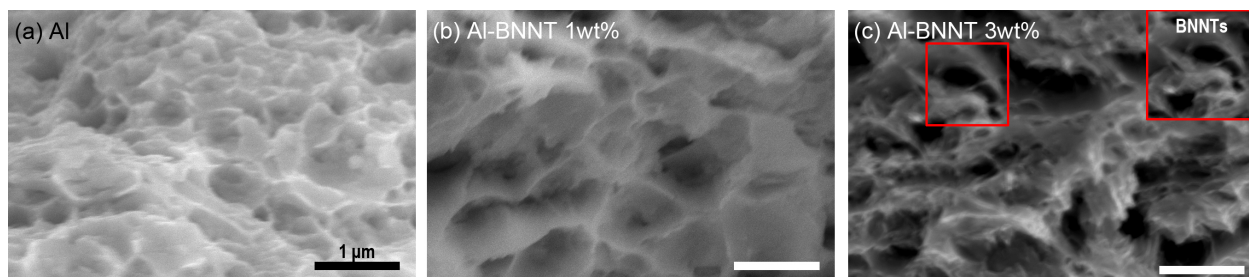

Figure 4.12 SEM images of the fracture surfaces of tensile tested pure Al (a), Al-BNNT 1 wt% and Al-BNNT 3 wt% HPT composites. The inset in (c) shows the enlarged framed area where three individual BNNT are seen bridging the two Al bulk portions across the existing micropore. All the scale bars are 1μm.
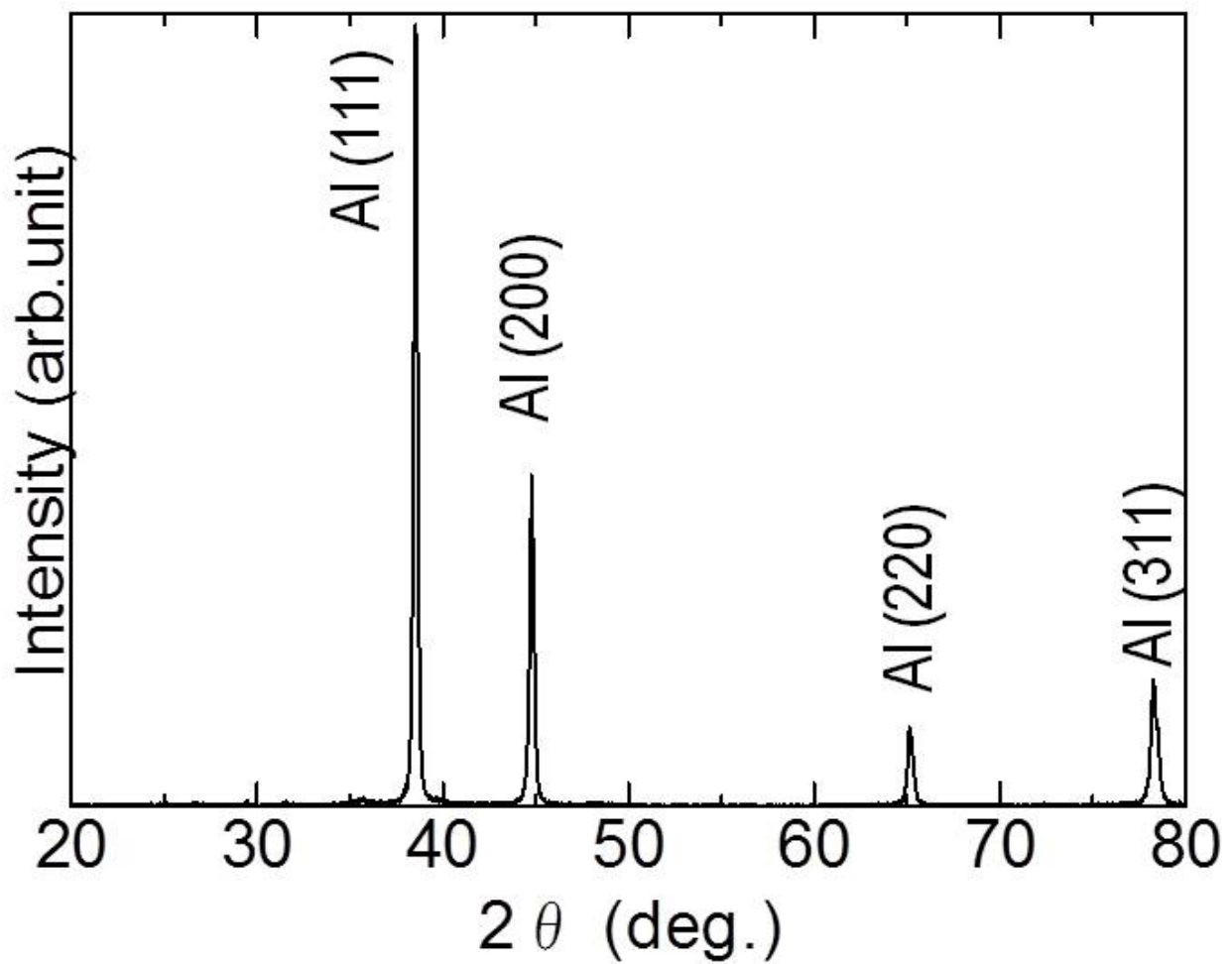
Figure 4.13 A XRD spectrum of an Al-BNNT 3wt% macrocomposite by HPT. Al is polycrystalline and there were no other phases notices such as Al nitrides or borides.
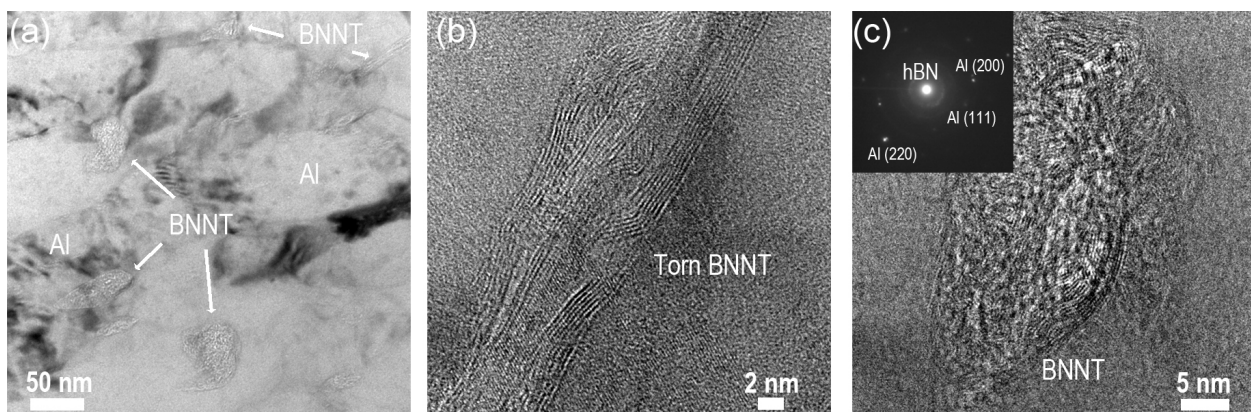

Figure 4.14 Low- (a) and high resolution (b and c) TEM images of an Al-BNNT 3 wt% macrocomposite by HPT near fractured area after the tensile tests. Both Al nanocrystals and BNNTs (whirled and straight) are seen in the area (a). Torn BNNT (b) and whirled BNNT (c) were also found.

81

4.4   Summary

In summary, for the first time, we fabricated Al-BNNT macrocomposites by using two different methods – SPS and HPT using various multi-walled BNNTs fractions (from 1.0 to 5.0 wt%). Scanning and transmission electron microscopy, X-ray diffraction, and energy dispersive X-ray analysis confirmed the decent integration of the two phases into a dense and rather compact composite. No other phases, like Al borides or nitrides, form in the Al-BNNTs.

For SPS samples the BNNTs were mostly embedded along the Al grain boundaries.The hardness of the SPS-made pure Al and Al-BNNTs pellets was measured by using micro-Vickers hardness tester. The value is slightly decreased with increasing BNNT contents. Thermal diffusivity of SPS-made pure Al and Al-BNNTs composites was measured by using laser flash method at room temperature. A value of Al-BNNTs (0.95 cm^2/s) slightly decreased compared to pure Al (1.04 cm^2/s). As mentioned earlier, many of BNNTs were embedded along the Al grain boundaries and created the nanotube clusters. Those clusters might cause less quality in terms of thermal pathways.

The BNNTs were randomly oriented within the Al matrix in the HPT-made Al-BNNT compacts. BNNTs were found to exist both along the grain boundaries and within the Al grains.

The hardness of the HPT-made pure Al and Al-BNNTs compacts was also measured by using same micro-Vickers machine as for SPS-made samples. The hardness was increased with increasing BNNTs contents in the Al matrices. The value of Al-BNNT 3.0 wt% (5.8 vol%) was more than doubled (190 MPa) compared to pure Al (90 MPa). The ultimate tensile strength of the composite was also measured at room temperature using "dog-bone" shape HPT-made samples. The averaged tensile strength of Al-BNNTs containing 3.0 wt% (5.8 vol%) nanotubes (~300 MPa) was ~1. 5 times larger than that of a nanotube-free compact (200 MPa).

For both SPS and HPT samples, the same pure Al and mixed Al-BNNTs powders were used, however, the Al grain size and acting of BNNTs in the Al matrix were different depending on the fabrication method. In SPS-made Al-BNNT composite samples, some notable microporosites were found, especially at the grain boundaries, which cannot be overcome during sintering and spoil the effects of possible reinforcement owing to a strong BN phase. The porosity and related grain boundary discontinuity is progressing with an increase of BNNT contents explaining further decline in sample hardness. Notably, the nanotube and Al phases do not have a strong cohesion to each other. BNNT are seen being easily pulled out of the metal matrices. This tells us that the poor adhesion of BNNT to metals, and their known nonwettability, that put severe restrictions on an effective load transfer from a soft Al-matrix to the hard BNNT phase, are still the serious existing issues limiting the possibilities of making strong Al-BNNT SPS composites. On the other hand, HPT method is one of the severe plastic deformation techniques which lead to the grain refinement [31]. The HPT samples were highly dense.

The distinct difference between SPS and HPT composite sample performance is suggested to be due to a drastically different grain size and various degrees of microporosity for the two sample series. HPT

processing makes much denser composites where the effects of matrix strengthening (due to BNNT effectively incorporated within the grains) prevail over detrimental effects of porosity. Additionally, according to the Hall-Petch relationship shown in Figure 4.15 [32], around 20 ~ 60 nm grain sizes would guarantee the best performance for the sample hardening. Since HPT-made samples could be categorized as "nanosized-materials" with respect to the grain size and SPS-made samples are of "conventional grain size" the results of hardness tests look reasonable. Notable grain refinement in HPT samples compared to SPS ones also leads to an overall denser structure with a lesser number of micropores between the sintered Al grains.
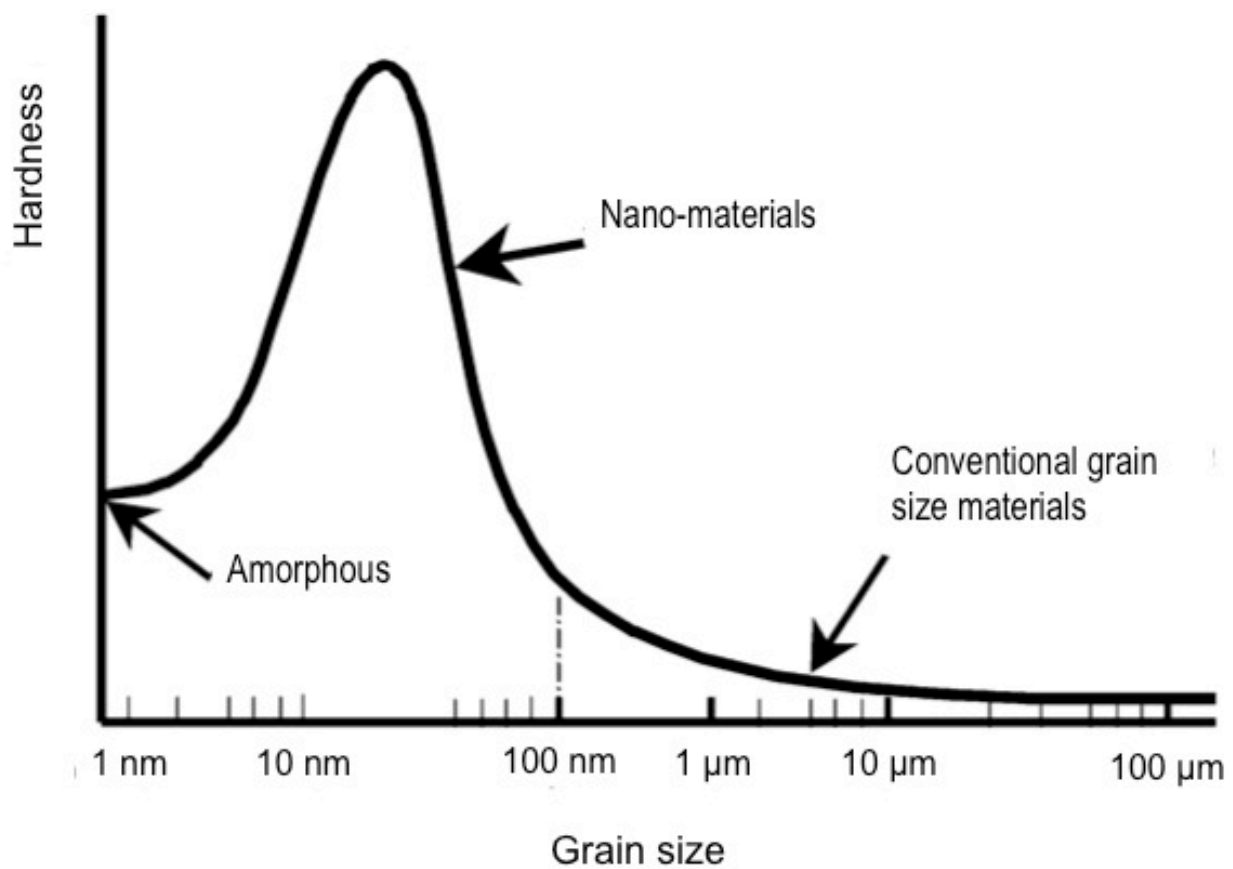

Figure 4.15 Hall-Petch relationship graph from the reference [4-32]. It can explain that between around 20 ~ 60 nm the grain size is optimal to achieve sample hardening. It would be one of the reasons why HPT samples had much higher hardness than SPS samples of the same compositions.

Overall, Al-BNNTs macrocomposites were successfully fabricated using several methods. The key of fabricating bulk Al-BNNTs composites is dispersion BNNTs into an Al matrix. Compared SPS with HPT processes, HPT looks to be simpler way to fabricate Al-BNNTs composites without heating or sintering processes. Also grain size could be refined and BNNTs could be located more randomly within the Al matrix compared to SPS-made samples. Although this study is still undergoing, the tried two methods are promising ways to fabricate bulk Al-BNNTs composites for the future applications.

4.5   References

[1] S.R. Bakshi, D. Lahiri, A. Agarwal. *Int. Mater. Rev.* **2010**, 55, 41.

[2] K.T. Kim, S.I. Cha, S.H. Hong, S.H. Hong. *Mater. Sci. Eng. A.*, **2006**, 430, 27.

[3] S.I. Cha, K.T. Kim, S.N. Arshad, C.B. Mo, S.H. Hong. *Adv. Mater.*, **2005**, 17, 1377.

[4] K. Sairam, J. K. Sonber, T. S. R. C. Murthy, C. Subramanian, R. K. Fotedar, P. Nanekar, R. C. Hubli. *Int. J. Refract. Met. Hard Mater.*, **2014**, 42, 185.

[5] D.Lahiri, V. Singh, L.H. Li, T. Xing, S. Seal, Y. Chen, A. Agarwal. *Mater. Res.*, **2012**, 27, 2760.

[6] D.M. Hulbert, A. Anders, J. Andersson, E.J. Lavernia, A.K. Mukherjee. *Scripta Mater.*, **2009**, 60, 835.

[7] D.Lahiri, V. A. Hadjikhani, C. Zhang, T. Xing, L.H. Li, Y. Chen, A. Agarwal. *Mater. Sci. Eng. A.*, **2013**, 574, 149.

[8] H. Kwon, M. Estili, K. Takagi, T. Miyazaki, A. Kawasaki. *CARBON.*, **2009**, 47, 570.

[9] H. Kurita, H. Kwon, M. Estili, A. Kawasaki. *Mater. Trans.*, **2011**, 52, 1960.

[10] S.R. Bakshi, R.R. Patel, A. Agarwal. *Computational Mater. Sci.*, **2010**, 50, 419.

[11] S. Cho, K. Kikuchi, T. Miyazaki, K. Takagi, A. Kawasaki, T. Tsukada. *Scripta Mater.*, **2010**, 63, 375.

[12] S. Cho, K. Kikuchi, A. Kawasaki. *Acta Mater.*, **2012**, 60, 726.

[13] R.Z. Valiev, T.G. Langdon. *Prog. Mater. Sci.*, **2006**, 51, 881.

[14] A.P. Zhilyaev, T.G. Langdon. *Prog. Mater. Sci.*, **2008**, 53, 893.

[15] H.J. Choi, J.H. Shin, B.H. Min, J.S. Park, D.H. Bae. *J. Mater. Res.*, **2009**, 24, 2610.

[16] H. Li, A. Misra, Y. Zhu, Z. Horita, C.C. Koch, T.G. Holesinger. *Mater. Sci. Eng. A.*, **2009**, 523, 60.

[17] N. Hansen. *Scripta Mater.*, **2004**, 51, 801.

[18] T. Tokunaga, K. Kaneko, Z. Horita. *Mater. Sci. Eng. A.,* **2008**, 490, 300.

[19] S.H. Joo, S.C. Yoon, C.S. Lee, D.H. Nam, S.H. Hong, H.S. Kim. *J. Mater. Sci.*, **2010**, 45, 4652

[20] H.J. Choi, G.B. Kwon, G.Y. Lee, D.H. Bae. *Scripta Mater.*, **2008**, 59, 360.

[21] P. Janei, E.Y. Yoon, J. Gubicza, H.S. Kim, J.L. Lábár, T. Ungár. *Mater. Sci. Eng. A.*, **2001**, 528, 4690.

[22] P. Janei, E.Y. Yoon, J. Gubicza, H.S. Kim, J.L. Lábár, T. Ungár. *Mater. Sci. Forum.*, **2013**, 729, 228.

[23] P. Janei, J. Gubicza, E.Y. Yoon, H.S. Kim, J.L. Lábár. *Composite A.*, **2013**, 51, 71.

[24] T. Noguchi, A. Magario, S. Fukazawa, S. Shimizu, J. Beppu, M. Seki. *Mater. Trans.* **2004**, 45, 602.

[25] J. Yuuki, H. Kwon, A. Kawasaki, A. Magario, T. Noguchi, J. Beppu, M. Seki. *Mater. Sci. Forum*, **2007**, 53, 889.

[26] K.T. Kim, S.I. Cha, S.H. Hong. Mater. Sci. Eng. A. 2007, 449-451, 46.

[27] G. Majkic, Y.C. Chen. *Proc. 47th AiAA Conf.*, Newport, Rhode Island, **2006-07**, 1-5.

[28] W.E. Forsythe. Smithsonian Physical Tables, compiled. *The Smithsonian Institution*, Washington, D.C., **1954**, ninth revised ed.

[29] C.R. Barrett, J.L. Lytton, O.O. Sherby. *7th Technical Report Project*, N-ONR 225 (60), **1965**, NR 031-ee2.

[30] X. Huang, N. Hansen, N. Tsuji. Science. 2006, 312, 249.

4. Macrocomposites

[31] Y. Estrin, A. Vinogradov. _Acta Mater._, **2013**, 61, 782.

[32] J. Schiotz. _Proc. 22th Riso Int'l Sympo. Mater. Sci._, Roskilde, Denmark, **2001**, 127.

4. Macrocomposites

Chapter 5

Conclusions

5. Conclusions

Chapter 5 Conclusions

In this Thesis, I focused on aluminum (Al) based boron nitride nanotubes (BNNTs) reinforced composites by using three different scales of dimensions , nano-, micro- and macrocomposites were fabricated and their structures and mechanical properties were studied to see their usage possibilities for new structural materials in automotive, aircraft and aerospace industries.

First of all, in Chapter 2, I introduced the structural and mechanical analyses of Al coated BNNTs nanocomposites prepared by magnetron sputtering deposition. Al was coated onto BNNTs uniformly and its thickness was controlled by magnetron sputtering conditions. There were only two phases, Al and BN and no other phases such as aluminum nitride or boride were found. We successfully carried out individual Al-BNNT nanocomposites tensile and bending tests by in-situ STM-AFM system and studied their mechanical fracture behavior by TEM. The ultimate tensile strength was ~ 360 MPa; thus 9 times larger than that of Al (40 MPa, reference data). During the mechanical tests, we found that Al-BNNTs have a negligible cohesion between Al and BN phases so that frequently BNNT "cores" may be pulled out of Al "shell" under the tensile tests. Also we noticed that only Al layer is cracked and there was no damage to the core BNNTs when such Al-BNNT nanocomposites broke by bending. To analyze sheer stress, theoretical calculations were carried out by using *ab initio* atomistic computer simulations. The result is that making some defects on BNNT surface would lead to higher stresses due to the enhanced nanotube cohesion to Al. The tensile strength for such material may rise up to 1 GPa.

Secondly, in Chapter 3, I presented the results of Al-BNNTs melt-spun ribbon studies. Al and BNNTs were mixed mechanically and the mixtures were used for melt-spinning. Representative tensile tests on ribbons were carried out using a standard "Shimadzu" testing machine. The ultimate tensile strength of Al-BNNTs was 145 MPa; so it was more than doubled compared to non-BNNT-loaded pure Al ribbons (60 MPa). Further details of Al-matrix / BN-phase interactions were analyzed by means of comparative measuring mechanical loss spectra in a wide-temperature range (80 ~ 800 K) on Al melt-spun ribbons reinforced with BN nanotubes and spherical BN microparticles. These demonstrated a rich variety of energy dissipation processes. Some of the modifications caused by the BN additions could be attributed to dislocation emission at the Al / BN interfaces due to thermal stresses, to competing accumulation and recovery of defects during thermal cycling, with comparatively more effective accumulation in case of nanotubes than in case of microparticles, and to an enhanced viscous deformation at high temperature.

Finally, in Chapter 4, I fabricated and compared Al-BNNT macrocomposites by using two different methods of powder metallurgy – SPS and HPT, and using various reinforcing multi-walled BNNTs fractions (from 1.0 to 5.0 wt%).

For the SPS-made samples, the Al grain size was 10 ~ 20 μm. Representative room temperature microhardness tests on sintered samples were carried out. The maximal measured hardness of SPS compact was 35 MPa (for the pure Al pellets). It remained basically unchanged or even slightly decreased with an

increased amount of BNNTs in the composites. This means that BNNTs made a little change to overall Al mechanical properties for the regarded samples.

On the other hand, HPT-made samples had several hundred nm Al grain size. The hardness increased with increased contents of BNNTs. The hardness of a pure Al sample is ~ 90 MPa, whereas that of an Al-BNNT 5.0 wt% was ~ 190 MPa, more than a doubled figure. The hardness value increased with increasing BNNT content compared to pure Al samples. The averaged measured tensile strength was close to ~300 MPa (Al-BNNT 3.0 wt%) and that of Al-BNNT 1.0 wt% and Al were around 200 MPa. The averaged ultimate tensile strength thus became ~ 1.5 times larger than in the case of a pure Al HPT compact. This value is already comparable with the tensile strength of an alloyed steel, like, for example, A36 (that has 400 MPa tensile strength) but our composite material is 3 times lighter (density of ~ 7.5 and 2.5 g/cm^3, respectively).

The distinct difference between SPS and HPT composite sample performance is suggested to be due to a drastically different grain size and various degrees of microporosity for the two sample series. HPT processing makes much denser composites where the effects of matrix strengthening (due to BNNT effectively incorporated within the grains) prevail over detrimental effects of porosity. Notable grain refinement in HPT samples compared to SPS ones also leads to an overall denser structure with a lesser number of micropores between the sintered Al grains.

Overall, I studied BNNTs reinforced Al composites by using nano-, micro- and macro-dimension scales. Their structural and mechanical properties analyses were carried out in details. Additionally the theoretical simulations and internal friction measurements for Al / BN interfaces were performed within several collaborative projects. All these works would lead to the promotion of bulk Al-BNNTs materials toward their future implementation for automotive, aircraft and aerospace industries of the future.

Chapter 6

Future project development

6. Future project development

Chapter 6 Future project development

Through nano-, micro-, and macro- Al-BNNTs composite studies, several issues which negatively affect further structural and mechanical improvement of the composites were realized. Mainly, there are two main factors determined. One is a weak cohesion at the Al/BN interfaces within the composites. In Chapter 2, I mentioned that the BNNT "core" is easily pulled out from an Al "shell" during the composite stretching.. Also, in Chapter 4, SPS-made samples were found to possess "numerous micropores at the matrix grain boundaries containing BNNTs. Another problem is making decent dispersions of BNNTs in the Al matrix. Especially for macrocomposites (Chapter 4), it is very important to have well-dispersed nanomaterial within a bulk composite. Here I illustrate some future projects based on theoretical predictions of these problem solutions toward the accomplishment of my dream-goal: achieving a "1 GPa" strength ultralight Al-BNNTs composite.

6.1   Mechanical property optimization based on theoretical predictions

As some experimental problems related to BNNT wetting by an Al matrix and cohesion strength at the Al/BNNT interfaces were realized in the course of my work, in the final part of my Thesis some additional theoretical estimates are done with respect to the ways showing how to overcome these problems, and to optimize the overall mechanical performance of a Al/BNNT composite.

First we decided to analyze how absorbed atoms on the nano-BN surface and BN sheet edge effects may affect the cohesion strength at the Al/BNNT interfaces.

As a method of the computations the scheme of Density Functional Theory (DFT) in the frame of Local Density Approximation (LDA) was selected. All computations were performed using the theory of electron density functional realized with the VASP package. For calculations of the atomic structures, the Brillouin zone was separated along with the Monkhorst-Pack scheme with 4 k-points in all periodic directions. Optimization of the structural geometry was performed until the energy *per* atom becomes lower than 0.05 eV/Å.

The main value entirely characterizing Al and nano-BN cohesion strength was selected to be the activation barrier needed for a nano-BN atomic sheet displacement over a length equal to one elemental unit cell of a modeled nanocomposite. As the first try, an ideal BN nanosheet was taken surrounded by Al atoms (Figure 6.1 (a)). The computed plot of energy *vs* an elemental moving step shows only a marginal increase, below 0.001 eV/BN (Figure 6.1 (b)). This tells us about a very low chemical activity of nano-BN surface within the Al matrix. And we suggest that it may significantly be increased using adsorbed adatoms on the BN nanosheet surface.
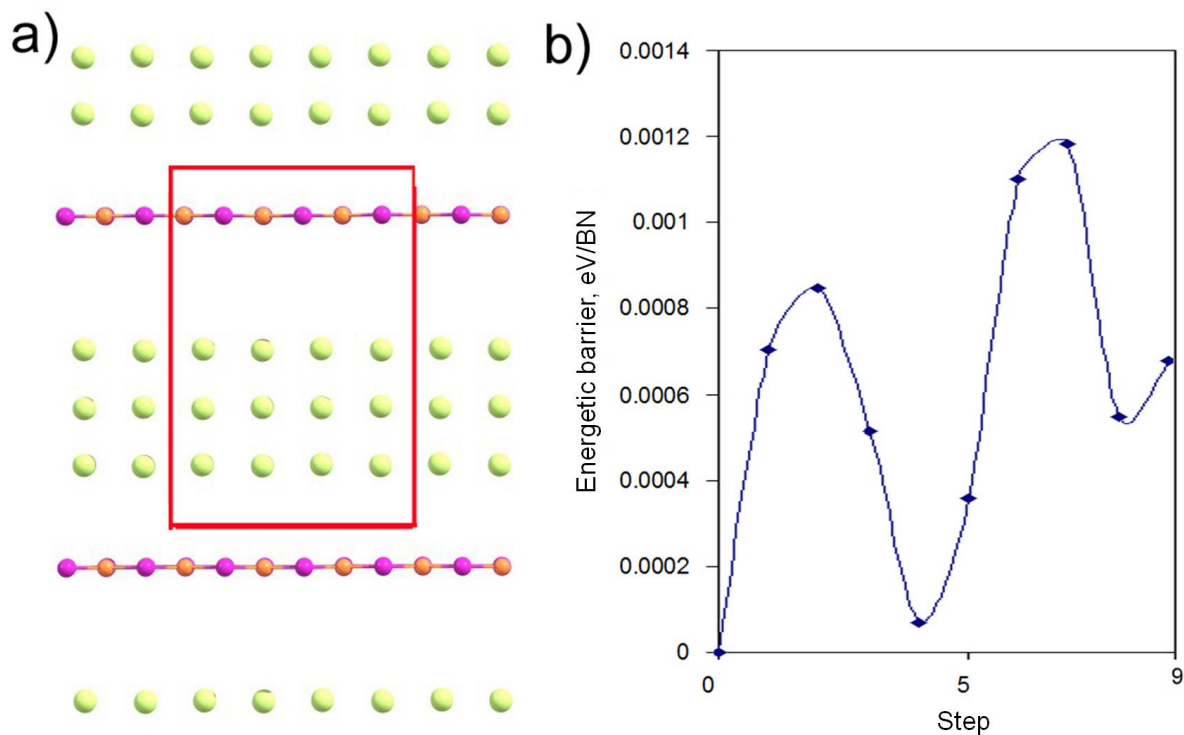
Figure 6.1 (a) Atomic structure of an Al/BNNT monolayer composite, Al, B and N atoms are drawn in light green, purple and orange colors, respectively; (b) Change in system energy under BN layer displacement along the Al atoms rows.
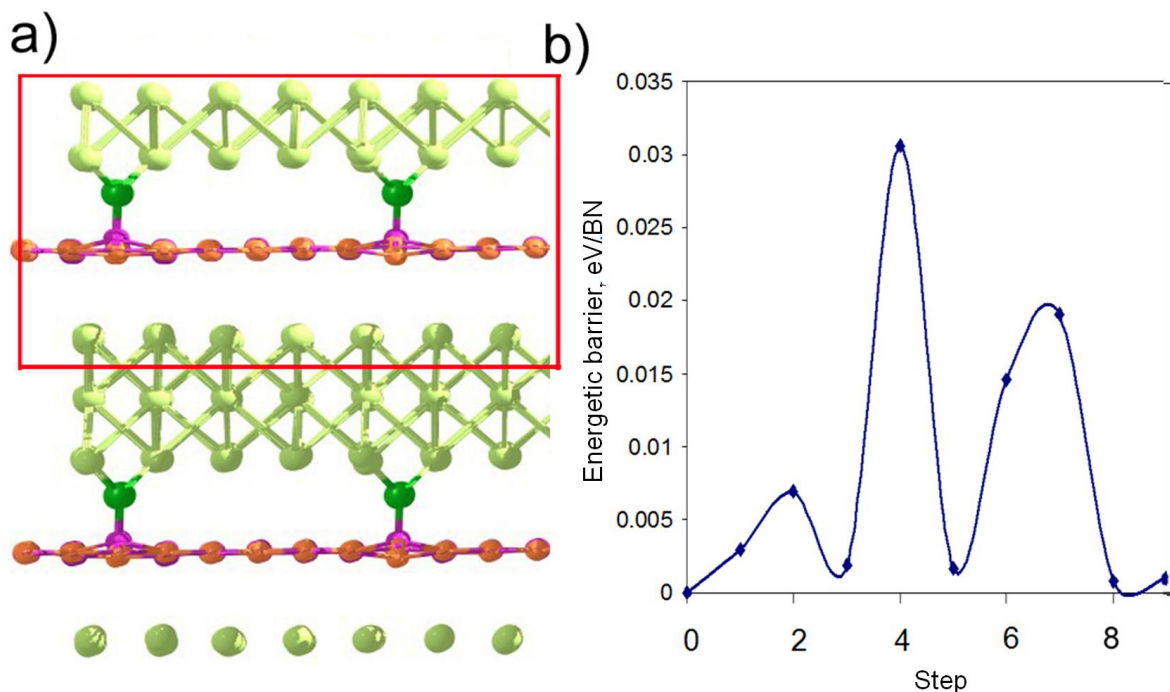

Figure 6.2 Atomic structure of an Al/BNNT monolayer composite with attached two Oxygen atoms; O, Al, B and N atoms are drawn in dark green, light green, purple and orange colors, respectively; (b) Change in system energy under BN layer displacement along the Al atoms rows.

6. Future project development

This effect was studied first taking oxygen atoms as an example. Oxygen atoms were chemically bonded to BN and Al phases, as marked in Figure 6.2 (a). Oxygen atom concentration was chosen as 6% in relation to the number of oxygen atoms to BN atoms ratio. Much stronger increase in activation barrier was obtained during displacement of such "sandwich", 0.03 eV/BN, as depicted in Figure 6.2 (b). We found that oxygen atoms chemically bond to Al atoms, breaking their bonds with a BN sheet under the regarded structural shuffle. This result predicts a very good potential of using transient surface-active layers (e.g. made of oxygen atoms) between the Al matrix and nano-BN phase for the Al/BNNT interfacial cohesion improvement.

Next, we suggest that dangling bonds at the nano-BN edges may play the key role for enhancing cohesion with the Al mother phase. We studied narrow BN nanoribbons (a width of 0.8 nm) embedded into an Al crystal (Figure 6.3(a)). The activation barrier during ribbon movement was calculated to be 0.13 eV/BN (Figure 6.3(b)). This value is the largest one among all the computed cases. Therefore, we may conclude that Al-based composites having nano-BNs with dangling and/or broken bonds at their edges do not require any transient layers and lead to much improved cohesion with the metal, just due to their own peculiar energetic.
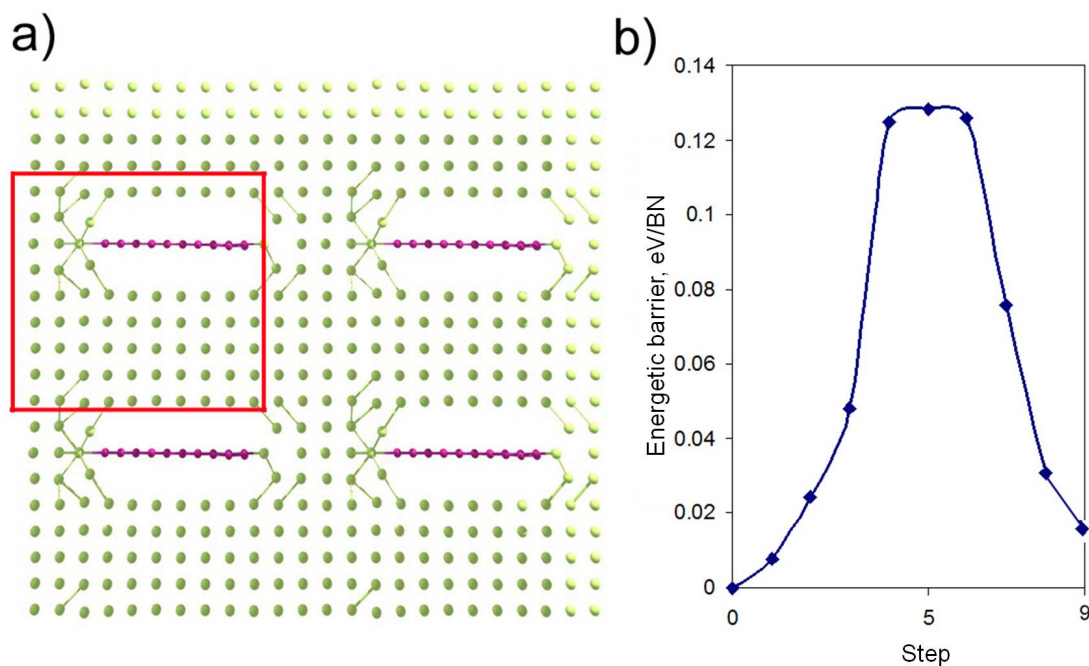

Figure 6.3 Atomic structure of an Al/BNNT nanoribbon composite, the framed area shows the system elemental cell; Al, B and N atoms are drawn in light green, purple and orange colors, respectively; (b) Change in the system energy under BN monolayer displacement along the Al lattice.

6. Future project development

Then, we theoretically compared the mechanical properties of composites with functionalized BNNT with those without functionalization. First, we calculated the elastic constant C_{11} for an Al crystal, an *h*-BN crystal and for a composite of Al with the BN nanoribbon (a ribbon width is of 0.8 nm). And we calculated that the embedment of such ribbon into the Al crystal had led to C_{11} constant increase from 50 GPa to 211.3 GPa. Also we tested how oxygen molecule functionalization on a BN monolayer may affect the mechanical properties. We found that the preferential site for oxygen atom incorporation in a BN ribbon is the B-N bond, as displayed in Figure 6.4 (a). We finally carried out the calculations of C_{11} constant of such hybrids depending on O-atom concentration on the BN surface. And a non-trivial effect was documented: a BN ribbon may be further strengthen at a low O-atom concentration (a rise of C_{11} up to 15%, for a 1.3 % O-atom content), as illustrated in Figurr 6.4 (b) for the two cases of O attachment - either one or two O-atoms located
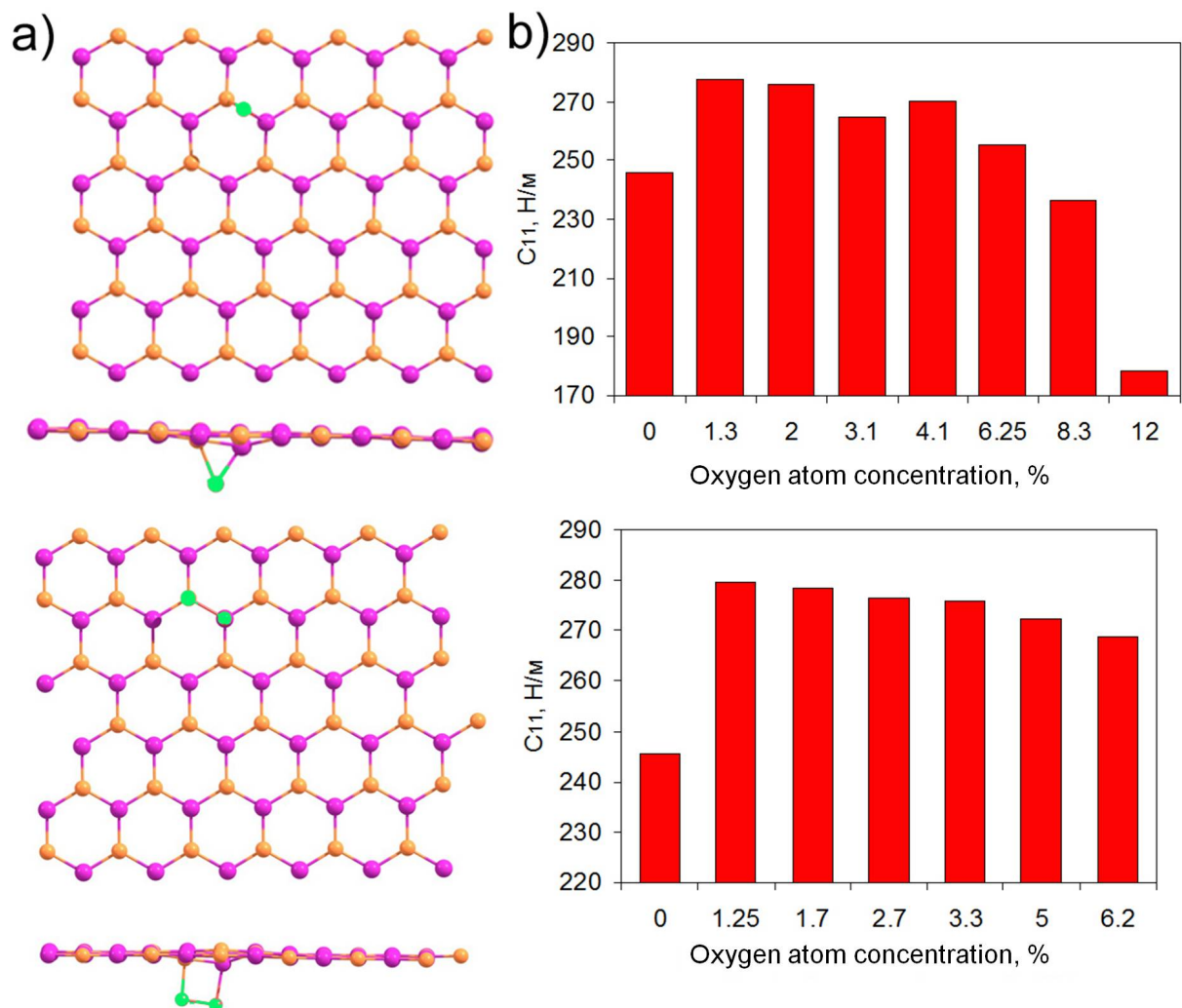

Figure 6.4 Atomic structure depicting energetically favorable Oxygen atom locations on a BN monoatomic layer for the cases of 1 O-atom (upper panel); and 2 O-atoms (lower panel); O, B and N atoms are drawn in dark green, purple and orange colors, respectively; (b) Corresponding dependences of C^{11} elastic constant as a function of Oxygen atom concentration

on a single B-N bond. More profound effect was noticed for the second case, i.e. two O-atoms placed beneath the B-N bond, as marked in the low section of Figure 6.4 (a), make the structure more effectively rigid. Thus it may be concluded that O-based functionalization not only enhanced the cohesion between nano-BN and Al phases but also additionally increases the rigidness of the reinforcing nano-BN phase itself. And we envisage that O-atom functionalization of a nano-BN reinforcing phase is a prospective route for the further Al-BNNT composite mechanical property optimization to be experimentally implemented in the nearest future.

6.2   Molecular level mixing for dispersion BNNTs

Uniform dispersion of CNTs has been the main challenge in CNTs-reinforced composites based on polymers, ceramics or metal matrices [1]. Also in our studies using BNNTs, it was one of the biggest challenges in the processing. This is due to the fact that BNNTs have tremendous surface area, which leads to formation of clusters due to Van der Waals forces. The elastic modulus, strength and thermal properties of a composite are related to the volume fraction of the reinforcement added. Hence, a homogeneous distribution of reinforcement is essential as it translates into homogeneous properties of the composite. Clustering leads to concentration of reinforcement at certain points and this could lead to worsening of overall mechanical properties. Blending by mixing is not effective in dispersing the BNNTs especially for the bulk samples (Chapter 4). I have observed that mechanical (hardness) and thermal (thermal diffusivity) properties deteriorate for SPS-made composites made with larger concentration of BNNTs. The worsening in the properties is due to the inability to obtain uniform distributions of BNNTs at large volume fractions.

Several methods have been developed to uniformly distribute CNTs in metal matrixes. Noguchi *et al.* have suggested Nano scale dispersion (NSD) process which results in uniform dispersion of CNTs in an Al powder [2]. NSD method is to disperse CNTs by functionalizing with -COOH with some acids, such as HNO_3 and/or H_2SO_4. It might be necessary to find other routes for functionalization in the case of chemically passive BNNTs. A sevenfold increase in the compressive yield strength was observed for 1.6 vol% CNT addition. Cha *et al.* have developed a novel molecular-level mixing method for dispersing CNTs [3]. Figure 6.5 shows the images of the powders obtained by various techniques and corresponding uniform distributions of CNTs. The methods suggested above have their own drawbacks. The NSD process leads to good dispersion of CNTs on the particle surface, so that the level of dispersion is dependent on the particle size used. Molecular-level-mixing methods might lead to oxide impurities because of incomplete reduction of the powders. While the quality of dispersion is important, the processes used should also be amenable to bulk production of composite powders. Quantification of the degree or quality of CNT reinforcement is important. It helps in comparing various microstructures and the effectiveness of various methods for dispersion of nanotubes in composites.

I would suggest a simple method to quantify the distribution of nanotubes in a composite. The usage of NSD methods is proposed to be very useful for BNNT dispersion within a composite microstructure.

6.3   Other methods for macrocomposites

To compact Al-BNNTs powders, it was thought that SPD techniques would be the best way in Chapter 4. These techniques are very popular owing to their ability to produce considerable grain refinement in fully dense, bulk-scale, work-pieces, thus giving a promise for the real structural applications. A great advantage of the SPD techniques is that they are based on a "top-down" approach involving grain refinement through "breakdown" of the microstructure of the bulk to the submicrometer scale. SPD processing is thus free from problems of excessive residual porosity and contamination, which are common in nanostructured materials manufactured in a "bottom-up" fashion, e.g. by consolidation of nanopowders. Furthermore, no health hazards potentially associated with handling of nanopowders are involved in SPD processing [4]. A drawback of the presently applied HPT method is that only small coin-shaped samples, typically 10-15 mm in diameter and 1 mm in thickness may be produced [4]. For the future applications, it is important to produce bigger samples so it would be needed to use other SPD techniques to obtain similar structures as those found for the HPT-made samples, but at the bigger scale. Other SPD techniques for Al-BNNTs powder compacting would be considered such as equal-channel angular pressing (ECAP), Accumulative roll-bonding (ARB), Multi-directional forging (MDF) and Twist extrusion (TE) etc. It could be possible, for example, to process the samples as large as 50×50 mm^2 in cross-section and 500 mm in length using ECAP [5] or –cm range of "sheet" type by ARB [6].
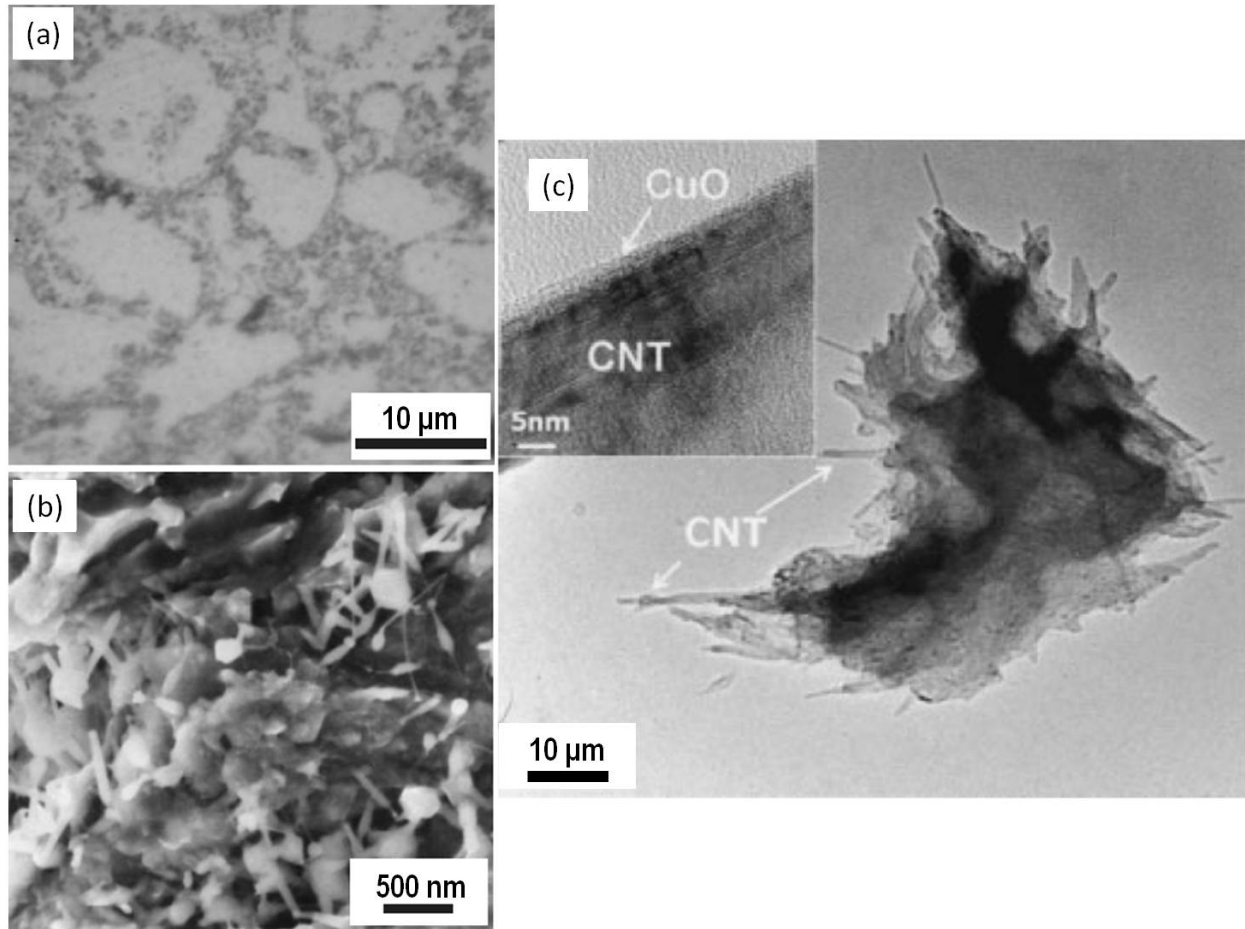
Figure 6.5 (a) (a) Optical micrograph of the cross section of a MWCNT/Al composite. (b) Scanning electron micrograph of the fracture surface of MWCNT/Al composite (from [2]). (c) TEM micrographs of CNT/CuO composite powders, showing that CNTs are implanted in the matrix with good bonding at the interface between CuO and the CNTs (inset) (from [3])

6.4 References

[1] S.R. Bakshi, D. Lahiri, A. Agarwal. *Int. Mater. Rev.* **2010**, 55, 41.

[2] T. Noguchi, A. Magario, S. Fukazawa, S. Shimizu, J. Beppu, M. Seki. *Mater. Trans.*, **2004**, 45, 602.

[3] S. I. cha, K. T. Kim, S. N. Arshad, C. B. Mo, S. H. Hong. *Adv. Mater.*, **2005**, 17, 1377.

[4] Y. Estrin, A. Vinogradov. *Acta Mater.*, **2013**, 61, 782.

[5] Frint P, Hockauf M, Halle T, Strehl G, Lampke T, Wagner MF-X. *Mater. Sci. Forum*, **2011**, 667–669, 1153.

[6] Saito Y, Utsunomiya H, Tsuji N, Sakai T. *Acta Mater.*, **1999**, 47, 579.

Chapter 7

Appendix

Appendix

Chapter 7 Appendix

In this chapter, I provide some supporting data for Chapters 3 and 4.

7.1   Al alloy-BNNTs melt-spun ribbons

Not only pure Al, but also Al-alloys had been tried as matrices for micro- and macro-composites. Al-based BNNTs melt-spun ribbons were fabricated using Al-based alloys added with copper ($Al_{85}Cu_{15}$), iron ($Al_{85}Fe_{15}$) or nickel ($Al_{85}Ni_{15}$). The sample lists are shown in Table 7.1. The basic process of making Al alloy-BNNTs composite ribbons was the same as that previously reported for Al. Before mixing with BNNTs, Al powder was mechanically mixed with another metal powder (Cu, Fe or Ni). Al alloy-BNNTs composite ribbons were prepared using a melt spinning machine (RQM-T-10, Manabe Giken, Japan) (at Prof. Louzguine's group, Tohoku University) in an argon atmosphere. Two different nozzle types for quartz tubes were used in these experiments (shown in Figure 7.1). One was a cylinder shape nozzle, diameter of 1 mm, the other had a rectangle shape, 15×0.3 mm. Al alloy-BNNTs compacts were melted by the induction currents, and melt-spun on a rotating water-cooled copper drum at a wheel rotation speed of 30-50 m s^{-1}. The fabricated melt-spun ribbons were approximately 50 μm in thickness and 4 to 5 mm in width. The length of the ribbons varied and was dependent on the stability of casting.

Table 7.1 Melt-spun sample list (prepared at Tohoku University)

Use quartz tube (A)
Use quartz tube (B)

		BNNT contents			
		0	0.5	1	1.5
Metals	Al	1 (WS:4084, P:0.03) 2 (WS:4900, P:0.02)	4 (WS:5000, P:0.04) 5 (WS:5000, P:0.03)	6 (WS:5000, P:0.03)	
	Al-Cu	3 (WS:5000, P:0.02)	7 (WS:3000, P:0.03) 18 (WS:3000, P:0.02)	8 (WS:3000, P:0.02)	9 (WS:3000, P:0.02)
	Al-Ni	16 (WS:3000, P:0.02)	10 (WS:3000, P:0.02)	11 (WS:3000, P:0.02)	12 (WS:3000, P:0.02)
	Al-Fe	17 (WS:3000, P:0.02)	13 (WS:3000, P:0.02)	14 (WS:3000, P:0.02)	15 (WS:3000, P:0.02)

WS: Wheel speed (rpm)
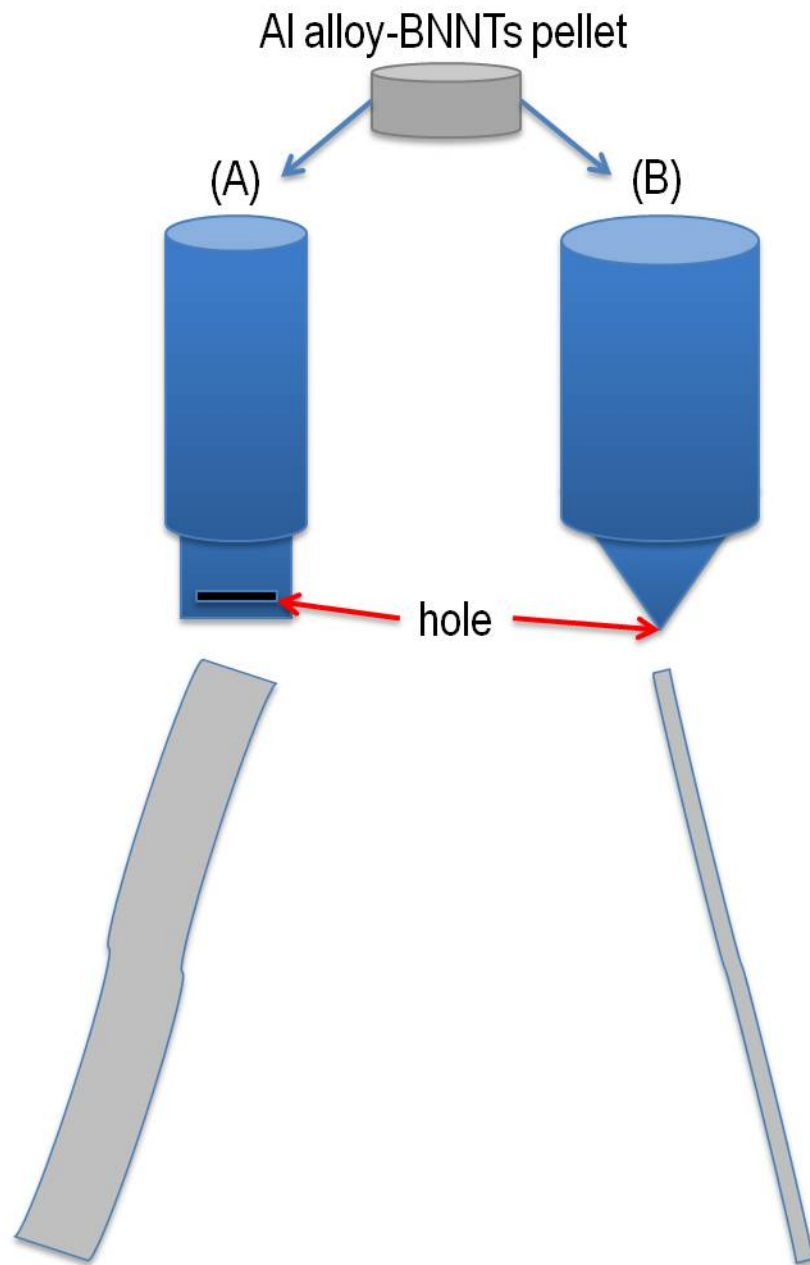P: Injection pressure (Pa)
Ar inlet pressure: 0.05 Pa

Figure 7.1 Two different nozzle shapes of quartz tubes used for melt-spinning experiments at Tohoku University.

7.1.1 Al-Cu alloy

Figure 7.2 shows XRD spectrum of an Al-Cu-BNNTs sample. Besides pure Al peaks obtained from Al-BNNTs melt-spun ribbons, $CuAl_2$ (110), (211) and (310) peaks were detected. Figure 7.3 shows SEM images of Al-Cu BNNTs samples. Some white-colored nanotubes are seen in the Al-Cu matrix (see the inset with the enlarged image). Figure 7.4 shows stress-strain engineering curves obtained for Al-Cu and Al-Cu-BNNTs melt-spun ribbons under the tensile tests. The maximum measured strength is ~ 550 MPa (Al-Cu-BNNT 3 wt%), which is more than 3.5 times larger than the maximum measured strength of Al-BNNTs.
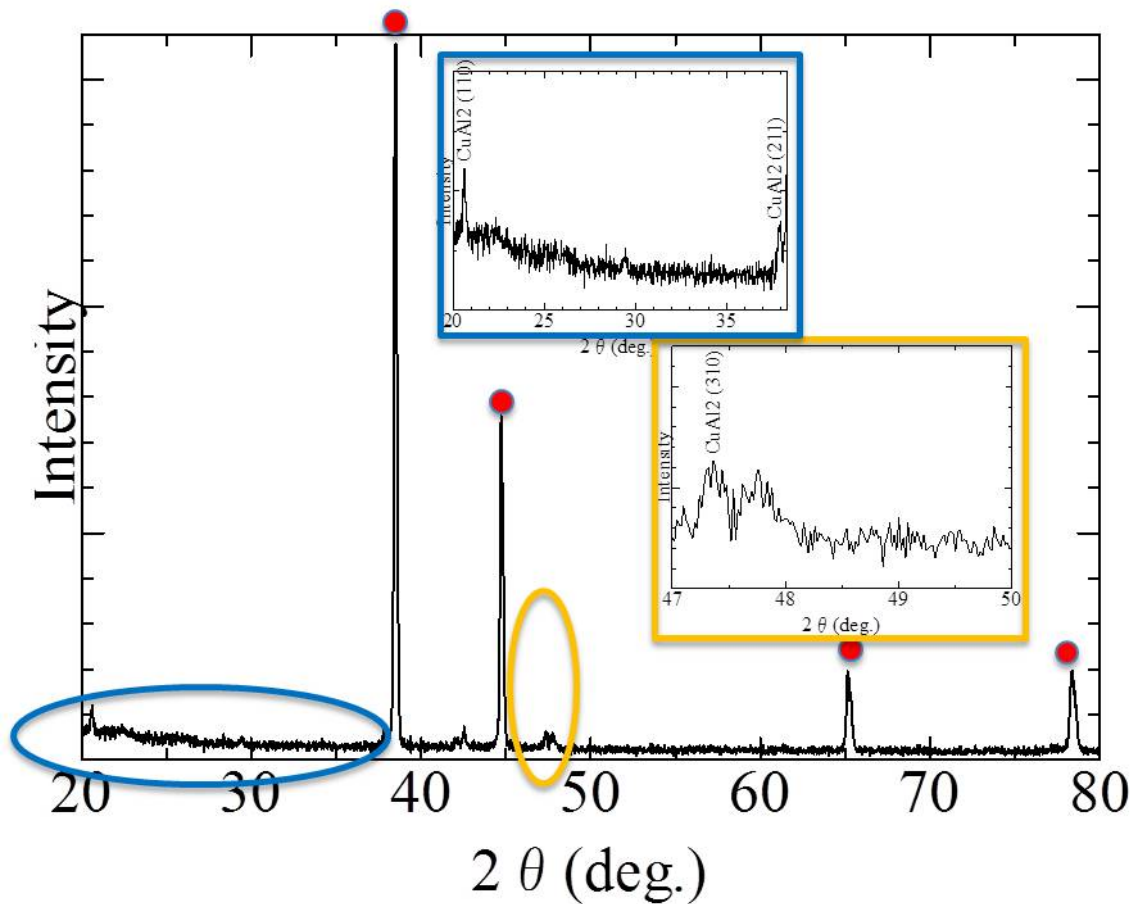
Figure 7.2 XRD spectra of Al-Cu-BNNTs melt-spun ribbon.
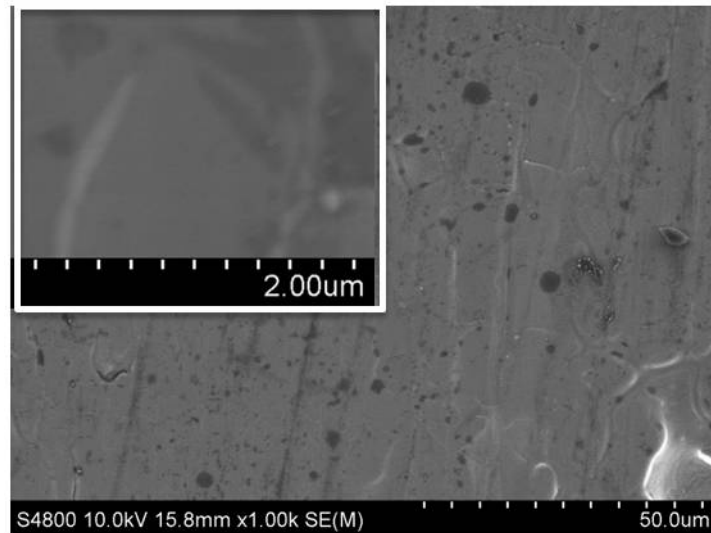
Figure 7.3 SEM images of an Al-Cu-BNNTs melt-spun ribbon. The inset is the enlarged image showing some BNNTs in the Al-Cu matrix.
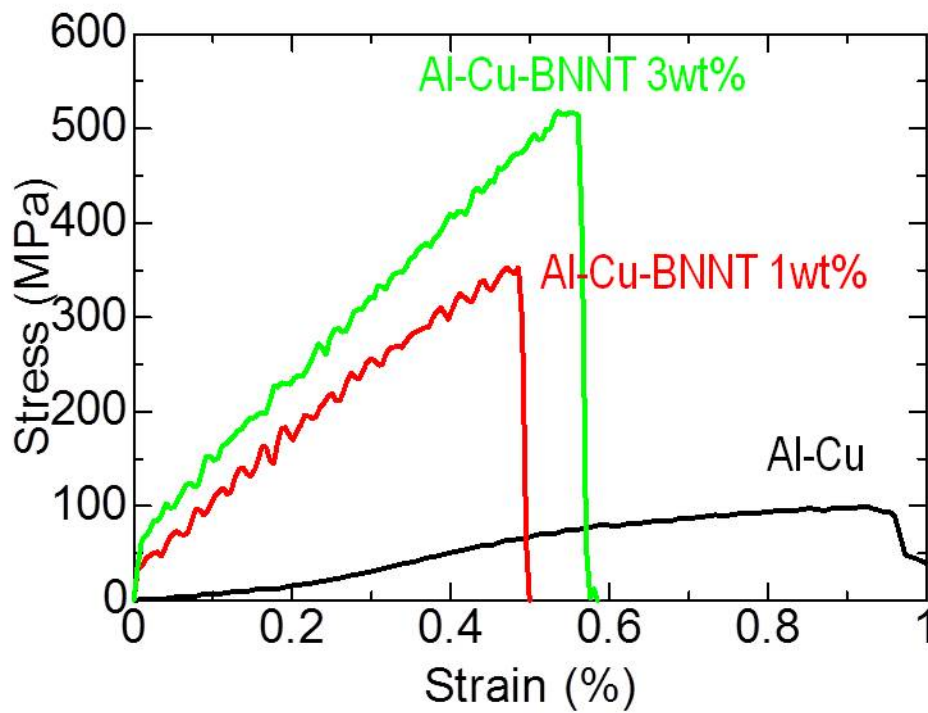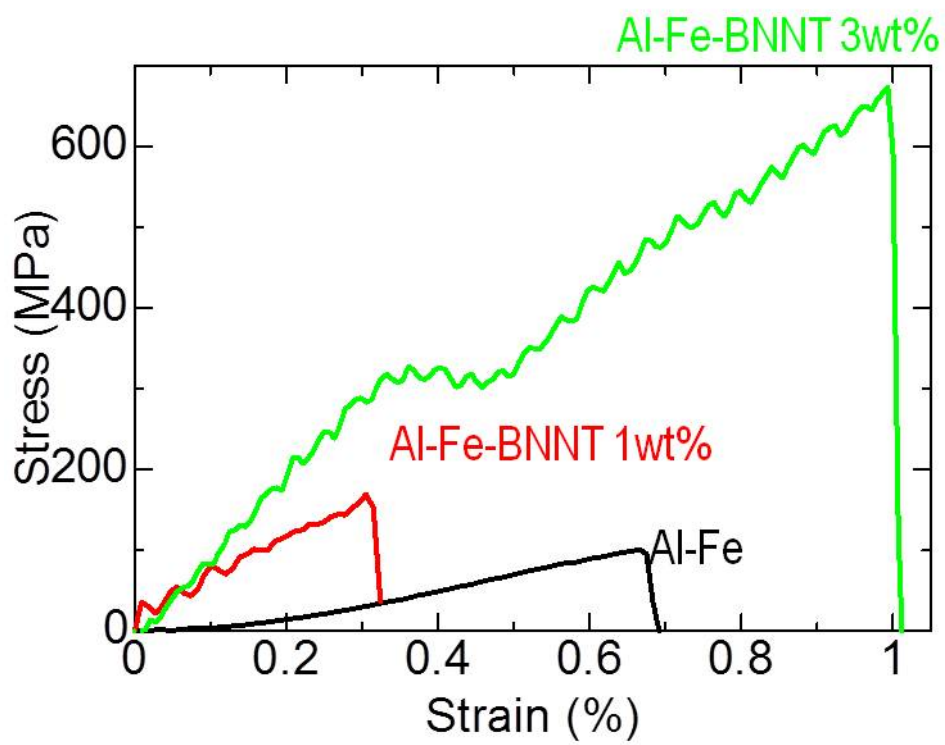

Figure 7.4 Stress-strain curves of Al-Cu and Al-Cu-BNNT melt-spun ribbons recorded under tension at room temperature.

7.1.2 Al-Fe alloy

Figure 7.5 shows XRD spectrum of an Al-Fe-BNNTs sample. Same as for the Al-Cu alloy sample, some additional peaks were detected in addition to a pure Al phase peaks, however, I was not able to determine what they were. Figure 7.6 shows SEM images of Al-Fe-BNNTs. Some nanotubes embedded into the Al-Fe matrix are also seen. Figure 7.7 shows stress-strain curves of tensile tests on Al-Fe and Al-Fe-BNNTs melt-spun ribbons. The maximum measured strength is close to 700 MPa (Al-Fe-BNNTs 3 wt%).
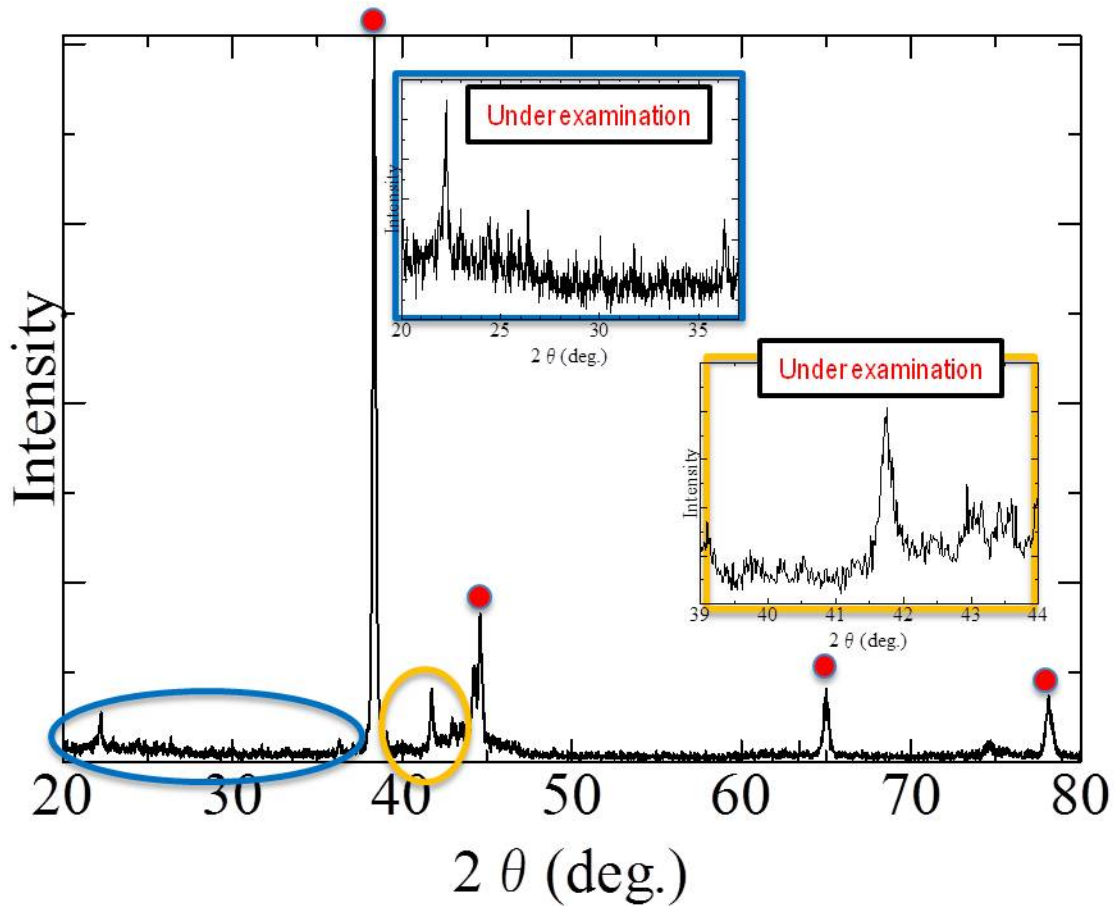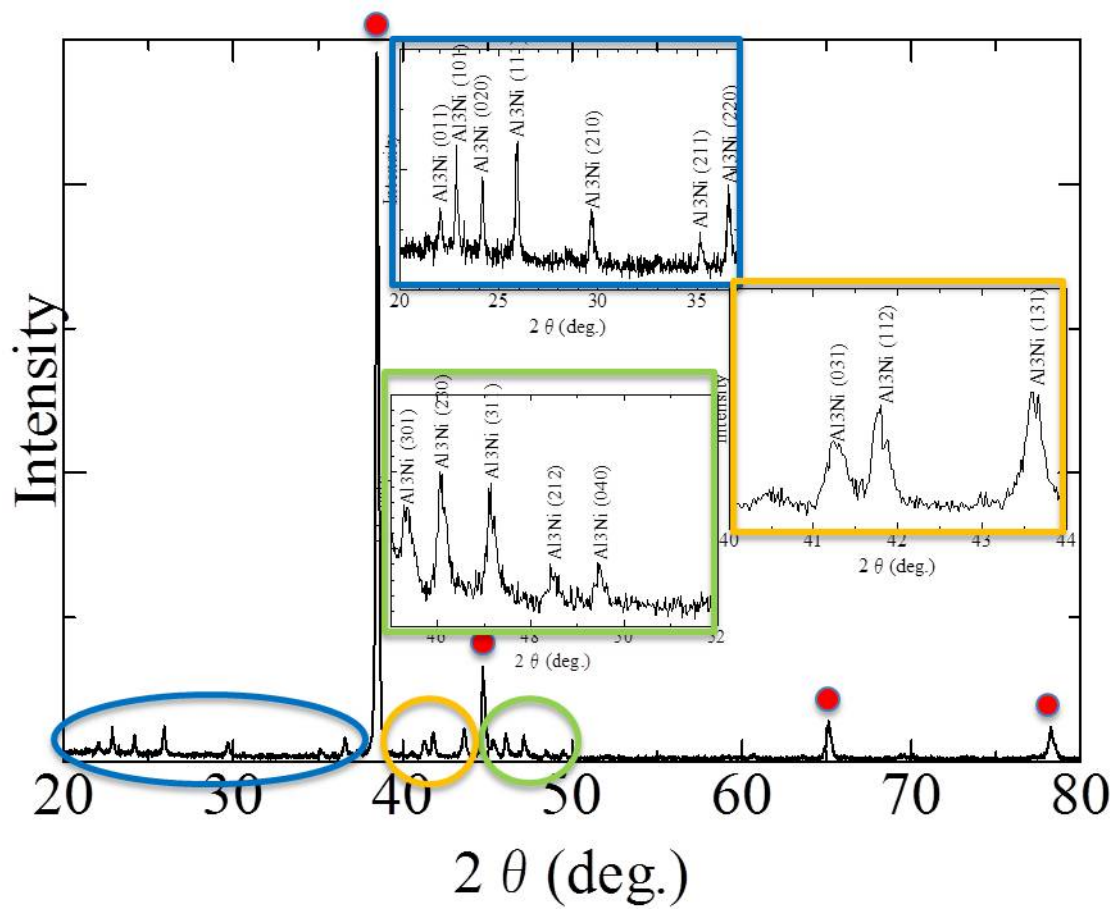

Figure 7.5 XRD spectrum of Al-Fe-BNNT melt-spun sample.
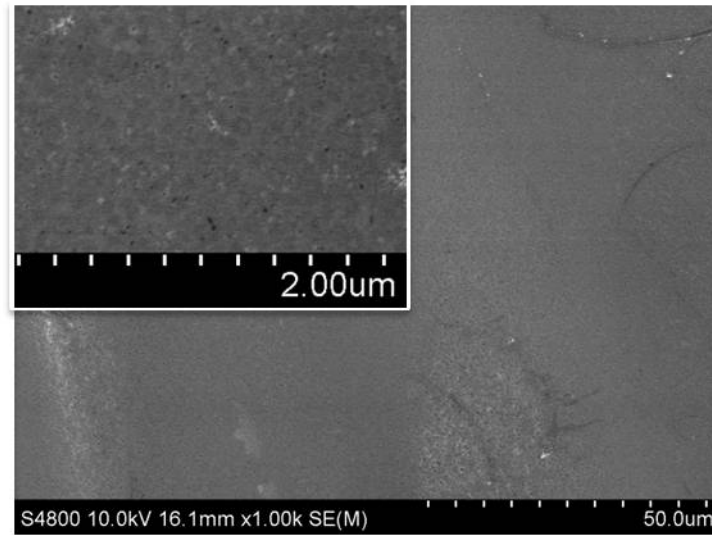
Figure 7.6 SEM images of an Al-Fe-BNNTs melt-spun ribbon.

Figure 7.7 Stress-strain curves of Al-Fe and Al-Fe-BNNT melt-spun ribbons under tension at room temperature.

7.1.3 Al-Ni alloy

Figure 7.8 shows XRD spectrum of Al-Ni-BNNTs samples. As for the cases of Al-Cu and Al-Fe alloys, Al-Ni alloy spectra (Al3Ni) were detected in addition to Al peaks. Figure 7.9 shows SEM images of an Al-Ni-BNNTs melt-spun ribbon. Here also some BNNTs are seen embedded into the Al-Ni matrix. Figure 7.10 depicts stress-strain curves recorded during the tensile tests on Al-Ni and Al-Ni-BNNTs melt-spun ribbons. Not like for Al-Cu-BNNTs and Al-Fe-BNNTs results, Al-Ni-BNNTs samples exhibited similar strength data as pure Al-Ni alloy melt-spun ribbons.

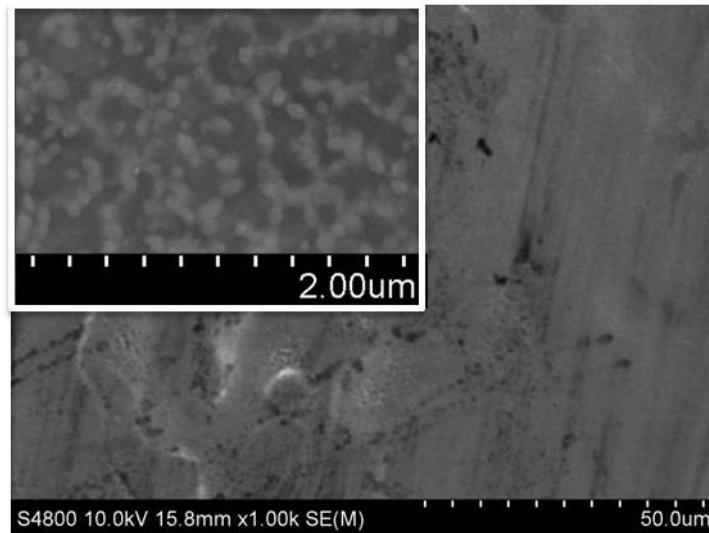**Figure 7.8** XRD spectrum of Al-Ni-BNNT melt-spun ribbon.

Figure 7.9 SEM images of an Al-Ni-BNNTs melt-spun ribbon.
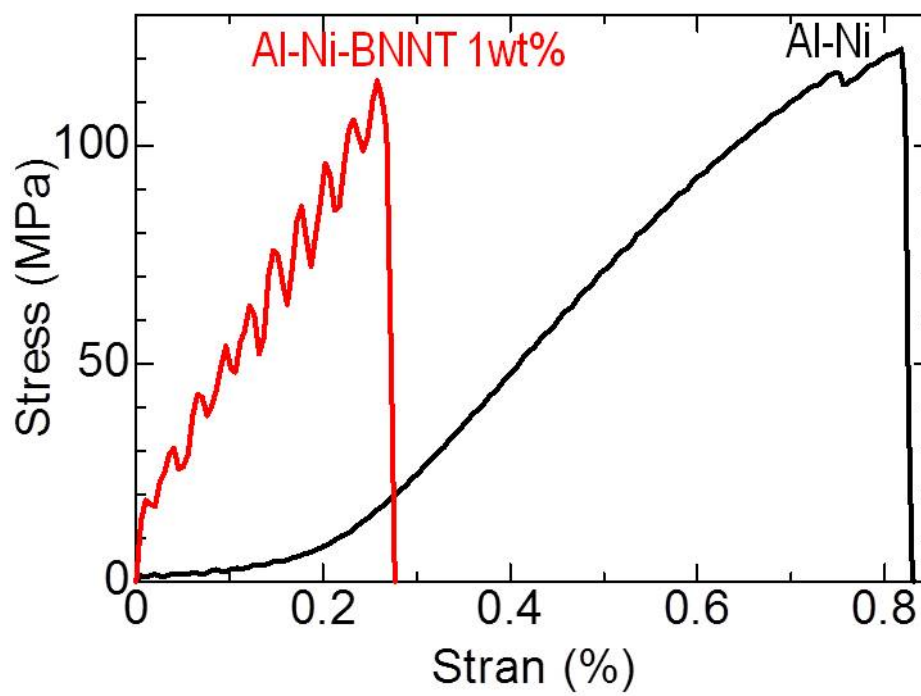

Figure 7.10 Stress-strain curves of Al-Ni and Al-Ni-BNNT melt-spun ribbons under tension at room temperature.

7.1.4 Summary

The results obtained on Al alloy-BNNTs melt-spun ribbons generally revealed a drastic increase in strength compared to Al-BNNTs melt-spun ribbons. As I mentioned in earlier Chapters, sometimes weak cohesion between Al and BNNT had been the issue of this study. Al alloyed with some metals, such as Cu and Fe, can make some transient compounds located at the nano-BN/metal interfaces and thus "glue" metal and BNNTs to increase the mechanical strength of the resultant composites. This work is still undergoing and needs more structural analysis and mechanical tests.

7.2   In-situ SEM mechanical tests at Rice University

Here I would like to show the results of tensile tests carried out at Rice University, USA, under collaboration with the group of Prof. Lou. The strength results obtained on melt-spun ribbons were very similar (comparison is shown in Figure 7.11). Also the images of fracture surfaces well resembled those discussed by me previously (shown in Figure 7.12), so it is justified that the discussed in the Thesis tensile tests carried out by a SHIMADZU AG-10 machine were pretty much reliable..
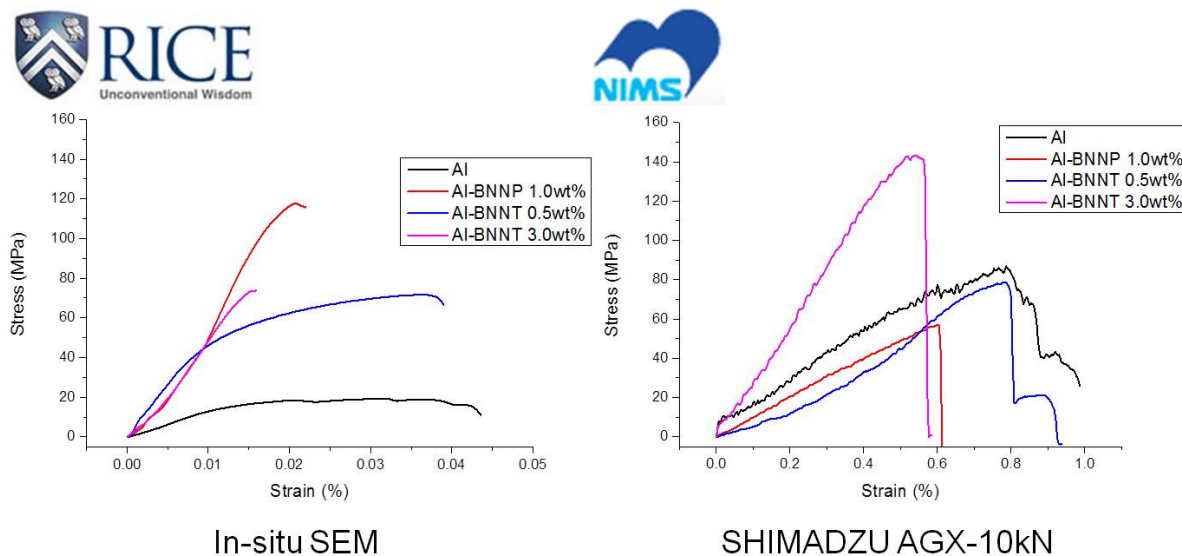

Figure 7.11 Stress-strain curves of Al and Al-BNNT melt-spun ribbons (right) compared with in-situ SEM data, left collected at Rice University)
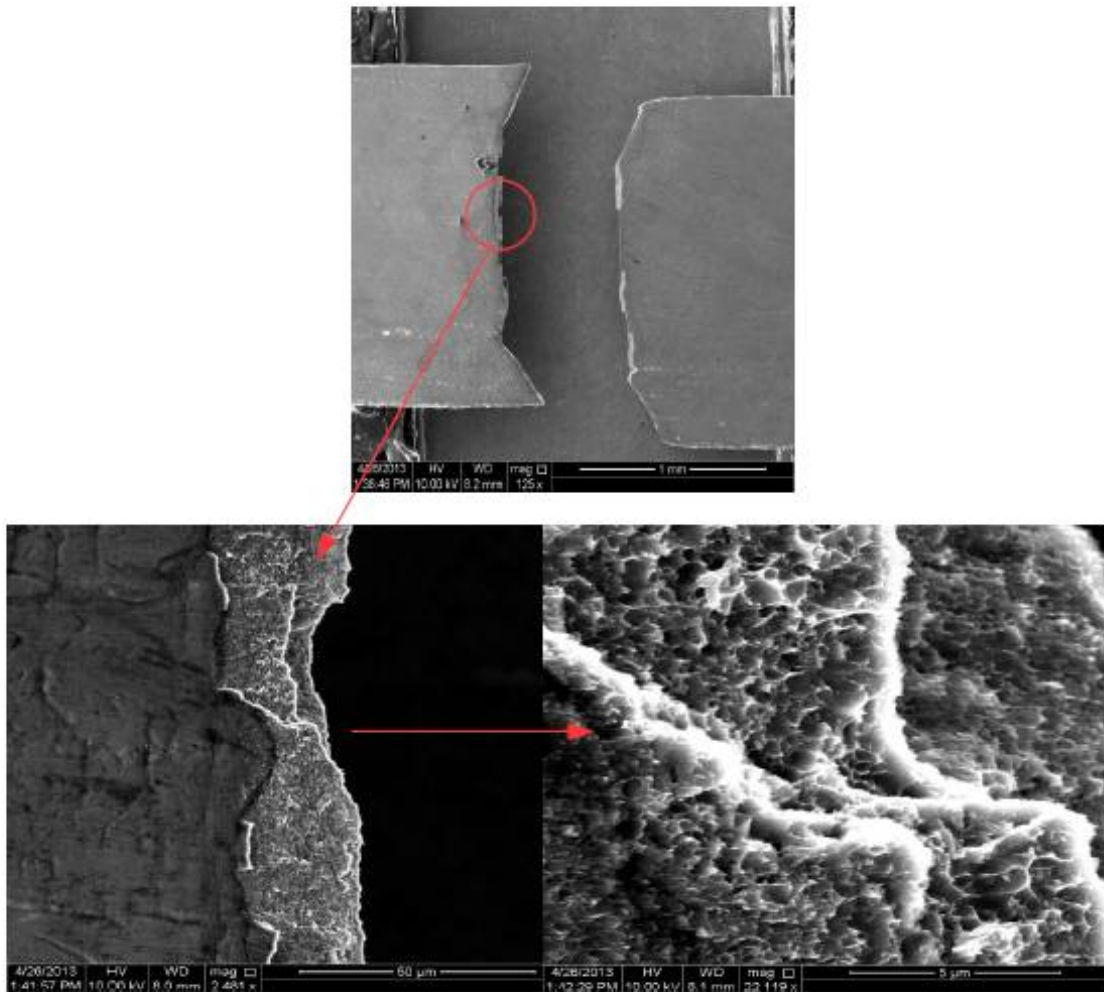
Figure 7.12 SEM images of fracture surface of melt-spun ribbon after in-situ SEM tensile tests.

Figures 7.13 to 7.16 show stress, strain, yield stress and yield strain data for pure Al, Al-Ni, Al-BNMP and Al-BNNT melt-spun samples obtained during the in-situ SEM tensile tests at Rice University.
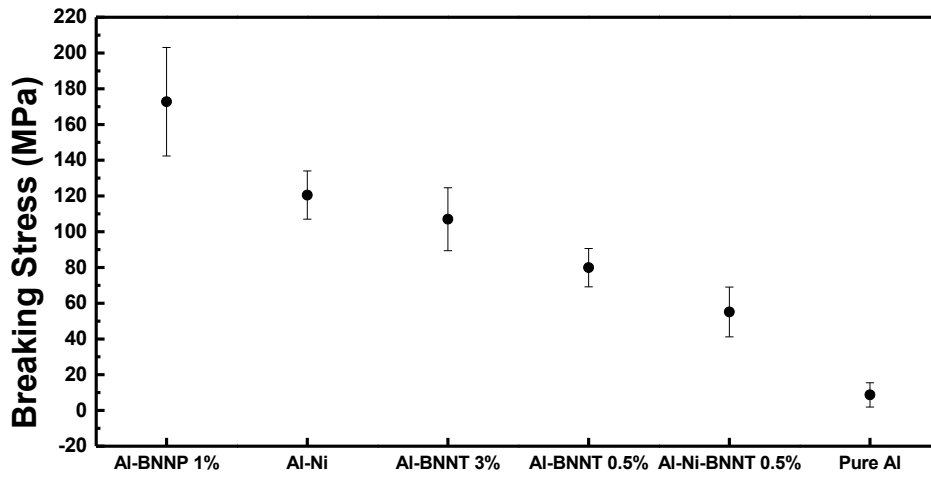
Figure 7.13 Breakage stress data of melt-spun ribbons by in-situ SEM tensile tests.
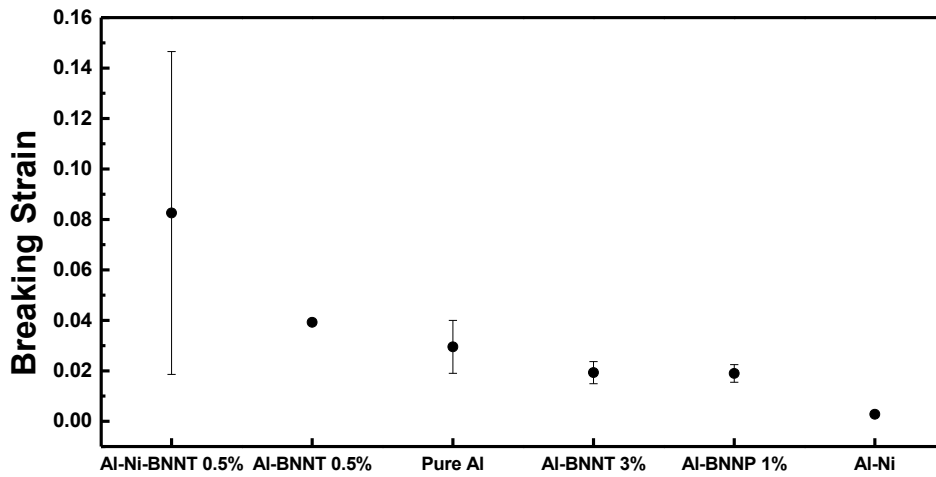

Figure 7.14 Breakage strain data of melt-spun ribbons by in-situ SEM tensile tests.
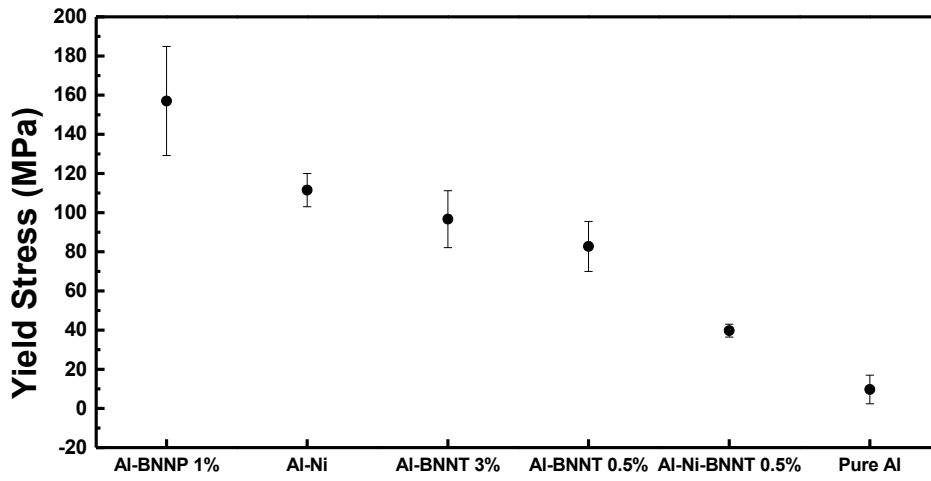
Figure 7.15 Yield stress data of melt-spun ribbons by in-situ SEM tensile tests.
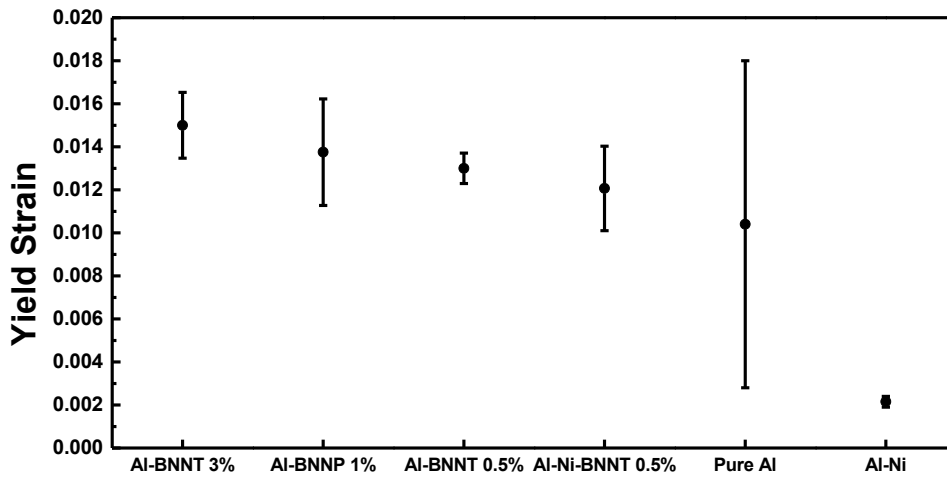

Figure 7.16 Yield strain data of melt-spun ribbons by in-situ SEM tensile tests.

7.3 Polishing and chemical etching condition on Al and Al-BNNT sample surface

Here I show the polishing conditions of melt-spun ribbons, SPS and HPT samples. Aluminum is very soft so it is difficult to polish and etch it to see the grain boundaries. It depends on the sample conditions, and it may take different time.

0. Mount the sample

Use plastic clip for thin samples like ribbons or tablets before putting in. Better using plastic resin but it is non-conductive so if one wants to use the sample for SEM, use Polyfast^{TM}.

1. Polish with a sand paper

#320 for about 1 min when one can see the surface

~ #1200 until every sample gets clean surface. * Every one minute change the paper

2. Polishing steps

Table 7.2 Basic polishing recipe for Al

	Paff	Paste	Suspension	Weight/ sample	Speed	Holder rotation	Time
2-1	Trident	Diamond 9 μm	MetaDi	5 lb	150 rpm	Same way	5 min
2-2	Vertex	Diamond 9 μm	MetaDi	5 lb	150 rpm	Same way	4 min
2-3	Chemomet	MasterMet (SiO_2)	Water	5 lb	150 rpm	Same way	3 min

2-1 and 2: Add Diamond paste or MetaDi every minute each time.

e.g. Diamond - > MetaDi -> Diamond -> MetaDi -> Diamond (5min)

2-3: Add MasterMet every 30 seconds and add water for last 20 seconds.

3. Chemical etching

Although there are some solutions for Al etching by acids, I chose Keller's reagent.

Keller's Reagent: 1.0 % HF + 1.5 % HCl + 2.5 % HNO_3 + H_2O

Time: depends on the sample. Check every 5-10 seconds with an optical microscope.

4. Check surface by microscope

For bulk samples, it may be possible to see the grain boundaries using a digital microscope e.g.Figure 7.17. However, it was difficult to obtain nice surface images for melt-spun ribbons as the samples were very thin so there were some problems when mounting the samples (it was difficult to make "flat" surface). So I tried

using Scanning Image Microscopy (SIM) images without polishing and etching process. The surfaces were scanned by an ion (such as Ga) beam and secondary electrons created the surface images. This technique is better for obtaining metal (such as Al or Cu) surface information compared with using SEM. I used this system under Focused Ion Beam (FIB) to obtain a continuous surface image. Figure 7.18 shows the SIM images of melt-spun surface.
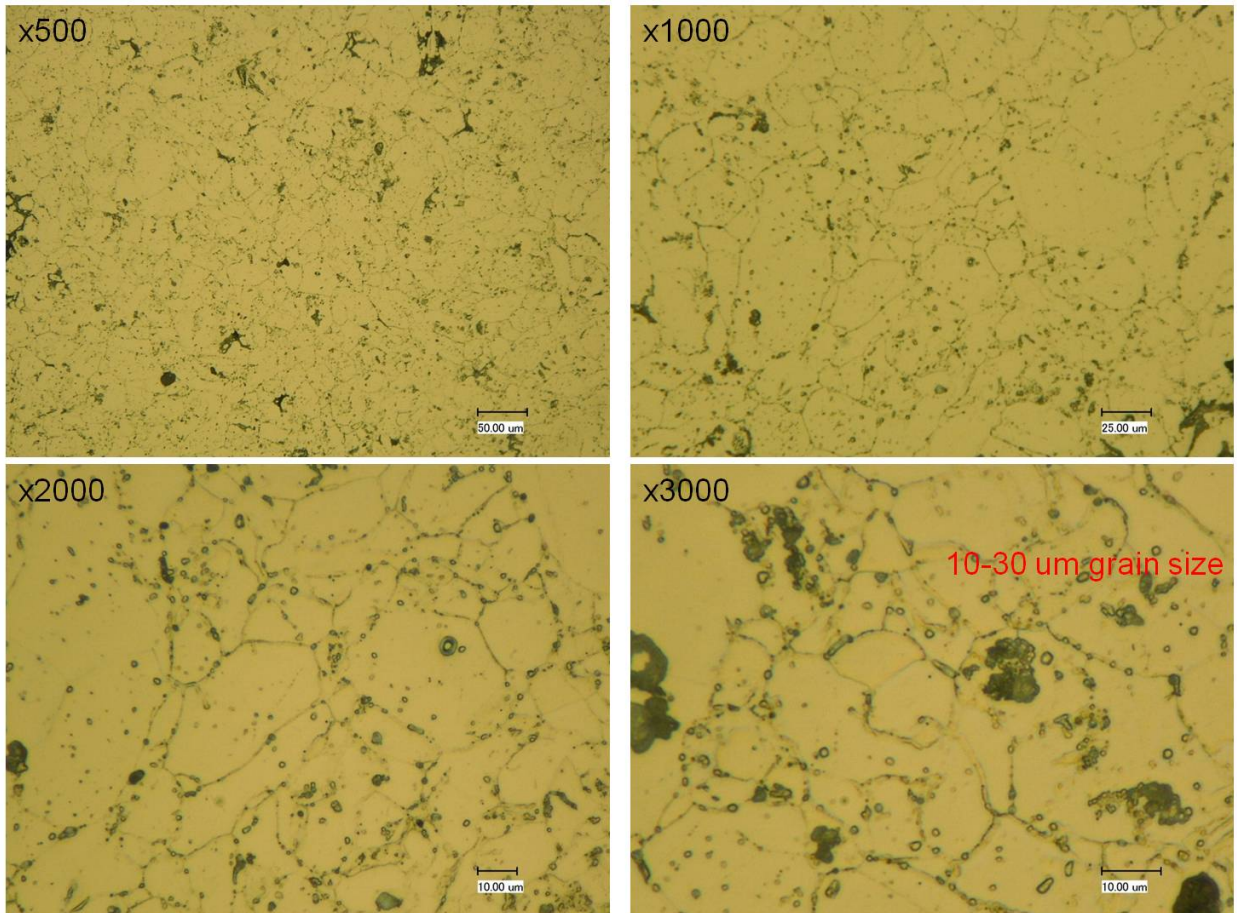

Figure 7.17 Digital microscopy images of SPS sample surface after polishing and etching using the recipe given in this Chapter.
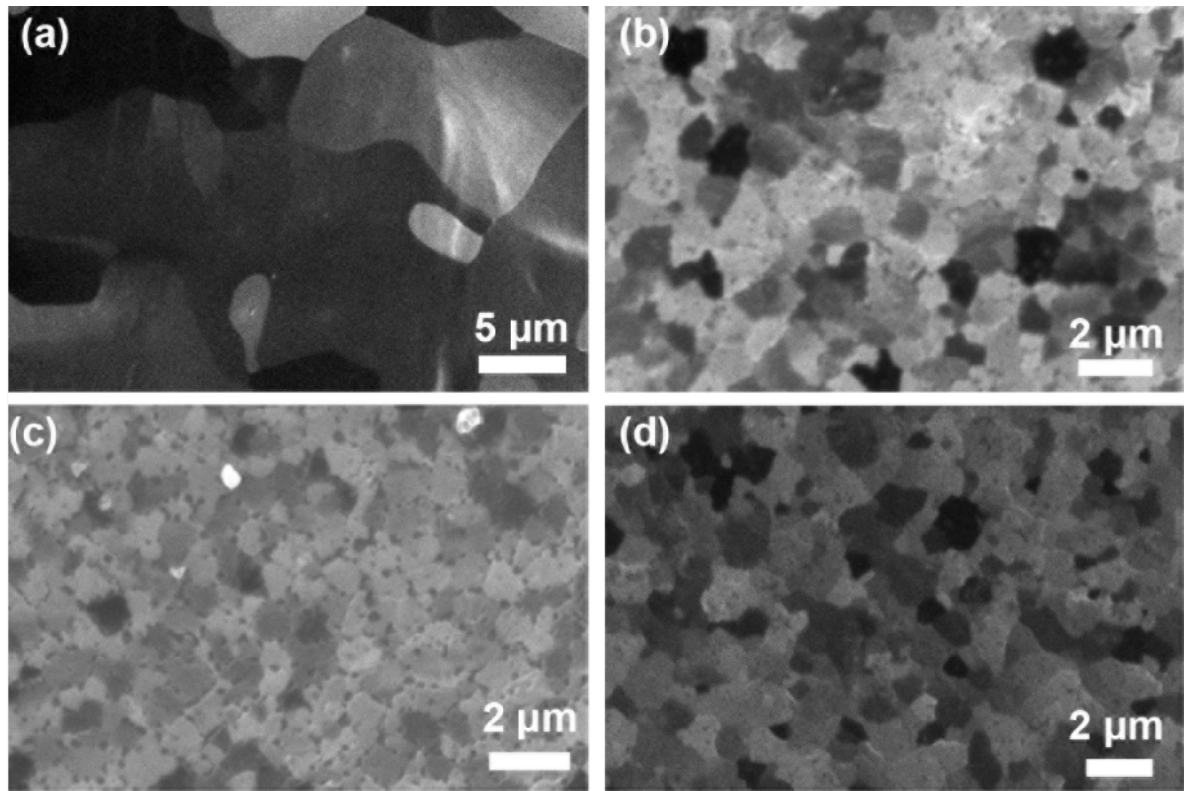
Figure 7.18 SIM images of Al-BNNT melt-spun ribbons under FIB system.

List of Publications

From April 2011 to December 2013

Academic publications

1. **M. Yamaguchi**, J. Bernhardt, K. Faerstein, D. Shtansky, Y. Bando, I. S. Golovin, H. R. Sinning, D. Golberg. *"Fabrication and characteristics of melt-spun Al ribbons reinforced with nano/micro-BN phases"* Acta Mater., **2013**, 61, 7604.

2. **M. Yamaguchi**, A. Pakdel, C.Y. Zhi, Y. Bando, D.M. Tang, K. Faerstein, D. Shtansky, D. Golberg. *"Utilization of multiwalled boron nitride nanotubes for the reinforcement of lightweight aluminum ribbons"* Nano. Res. Lett., **2012**, 8, 3.

3. **M. Yamaguchi**, D.M. Tang, C.Y. Zhi, Y. Bando, D. Shtansky, D. Golberg. *"Synthesis, structural analysis and in situ transmission electron microscopy mechanical tests on individual aluminum matrix/boron nitride nanotube nanohybrids"* Acta Mater., **2012**, 60, 6213.

4. Y-T. R. Lau, **M. Yamaguchi**, X. Li, Y. Bando, D. Golberg, F. M. Winnik. *"A Facile and Mild Strategy Towards Biopolymer-Coated Boron Nitride Nanotubes via a Glycine-Assisted Interfacial Process"* J. Phys. Chem. C., **2013**, 117, 19568.

5. X. Li, C.Y. Zhi, N. Hanagata, **M. Yamaguchi**, Y. Bando, D. Golberg. *"Boron nitride nanotubes functionalized with mesoporous silica for intracellular delivery of chemotherapy drugs"* Chem. Commun., **2013**, 49, 7337.

6. E. A. Obraztsova, D. Shtansky, A. N. Sheveyko, **M. Yamaguchi**, A. M. Kovalskii, J. Y. Mevellec, S. Lefrant, D. Golberg. *"Structural Changes of BN Nanotubes Irradiated by Al Ions"* J. Nanoelectron. Optoelectron., **2013**, 8, 87.

7. D. Golberg, D.M. Tang, X. Wei, **M. Yamaguchi**, N. Kawamoto, M. Mitome, C.Y. Zhi, Y. Bando, P. J. Costa, C. Ren. *"In situ TEM measurements of nanotube and nanosheet properties"* Microsc. Microanal., **2012**, 18, 1542.

8. E. A. Obraztsova, D. Shtansky, A. N. Sheveyko, **M. Yamaguchi**, A. M. Kovalskii, D. Golberg. *"Metal ion implantation of multiwalled boron nitride nanotubes"* Scripta Mater., **2012**, 67, 507.

Presentations

1. **M. Yamaguchi,** F.Q. Meng, N. Kawamoto, S. Ii, B. Pauw, K. Faerstein, D. Shtansky, K. Tsuchiya,

<u>*List of Publications*</u>

D. Golberg. *"Aluminum / Boron Nitride Nanotube Composites by High Pressure Torsion"*
MRS Fall Meeting & Exhibit, Dec 1-5, 2013, Boston, USA
Session title: Poster Session

2. **<u>M. Yamaguchi</u>**, A. Pakdel, C.Y. Zhi, Y. Bando, D.M. Tang, K. Faerstein, D. Shtansky, D. Golberg.
"Aluminum/Boron Nitride Nanotube Composite"
Fourteenth International Conference on the Science and Application of Nanotubes, Jun 24-28, 2013,
Espoo, Finland
Session title: Poster Session

3. **<u>M. Yamaguchi</u>**, A. Pakdel, C.Y. Zhi, Y. Bando, D.M. Tang, K. Faerstein, D. Shtansky, D. Golberg.
*"Synthesis, structural analysis and mechanical properties of aluminum matrix/boron nitride
nanotube hybrids"*
OSAKA University MANA/NIMS Joint Symposium, Mar 18, 2013, Tsukuba, Japan
Session title: Poster Session

4. **<u>M. Yamaguchi</u>**, A. Pakdel, C.Y. Zhi, Y. Bando, D.M. Tang, K. Faerstein, D. Shtansky, D. Golberg.
*"Utilization of multiwalled boron nitride nanotubes for the reinforcement of lightweight aluminum
and aluminum alloy ribbons"*
MANA International Symposium, Feb 27- Mar 1, 2013, Tsukuba, Japan
Session title: Poster Session

5. **<u>M. Yamaguchi</u>**, D.M. Tang, C.Y. Zhi, Y. Bando, D. Shtansky, D. Golberg. *"Synthesis, structural
analysis and mechanical properties of aluminum matrix/boron nitride nanotube hybrid composites"*
Thirteenth International Conference on the Science and Application of Nanotubes, Jun 24-29, 2012,
Brisbane, Australia
Session title: Poster Session

6. **<u>M. Yamaguchi</u>**, D.M. Tang, C.Y. Zhi, Y. Bando, D. Shtansky, D. Golberg. *"Synthesis of Boron
Nitride Nanotubes and Their Potentials for Light Metal Composite Reinforcement"*
MANA International Symposium, Feb 29- Mar 2, 2012, Tsukuba, Japan
Session title: Poster session

From previous work (At Aoyama Gakuin University)

Academic publications

1. K. Takahashi, N. Oka, **M. Yamaguchi**, Y. Seino, K. Hattori, S. Nakamura, Y. Sato, Y. Shigesato. *"Oxidation Resistance of Ti–Si–N and Ti–Al–Si–N Films Deposited by Reactive Sputtering Using Alloy Targets" Jpn. J. Appl. Phys.*, **2011**, 50, 075802.

2. A. Miyamura, **M. Yamaguchi**, K. Hattori, Y. Sato, S. Nakamura, Y. Shigesato. *"Ti-Al-Si-N Films for Super-Hard Coatings Deposited by Reactive Co-Sputtering using Ti, Al and Si Targets" J. Vac. Sci. Technol. A.*, **2007**, 25, 1103.

Academic publications

1. **M. Yamaguchi**, A. Miyamura, K. Hattori, T. Aoki, Y. Sato, Y. Shigesato. *"Comparative study on super-hardcoating materials between Ti_xW_yN and $Ti_xAl_ySi_zN$ deposited by reactive co-sputtering"*
   American Vacuum Society 53th International Symposium and Exhibition, Nov 12-17, 2006, San Francisco, CA
   Session title: Poster Session

2. **M. Yamaguchi**, K. Hattori, Y. Seino, A. Miyamura, Y. Sato, Y. Shigesato. *"Preparation of $Ti_xAl_ySi_zN$ super hard films deposited by 3-cathodes co-magnetron sputtering (2)"*
   The Japan Society of Applied Physics 67th Autumn Meeting, Aug 29-Sep1, Ritsumeikan Universiy, Shiga, Japan
   Session title: Poster Session

3. **M. Yamaguchi**, K. Hattori, A. Miyamura, Y. Sato, Y. Shigesato. *"Preparation of $Ti_xAl_ySi_zN$ super hard films deposited by 3-cathodes co-magnetron sputtering"*
   The Japan Society of Applied Physics 66th Autumn Meeting, Sep10, Tokushima Universiy, Tokushima, Japan
   Session title: Oral Session